Title
MEASUREMENTS OP THE MUON-CAPTURE RATE IN He3 AND He4

Author
Easterling, Robert John.

Publication Date
1964-04-09

University of California

Ernest O. Lawrence Radiation Laboratory

MEASUREMENTS OF THE MUON-CAPTURE RATE IN He^3 AND He^4

Berkeley, California

DISCLAIMER

UCRL-11004

UNIVERSITY OF CALIFORNIA
Lawrence Radiation Laboratory
Berkeley, California

AEC Contract No. W-7405-eng-48

MEASUREMENTS OF THE MUON-CAPTURE RATE IN He^3 AND He^4

Robert John Esterling

(Ph. D. Thesis)

April 9, 1964

Printed in USA. Price $2.75. Available from the
Office of Technical Services
U. S. Department of Commerce
Washington 25, D.C.

UNIVERSITY OF CALIFORNIA

Lawrence Radiation Laboratory
Berkeley, California

AEC Contract No. W-7405-eng-48

November 12, 1964

ERRATA

TO: All recipients of UCRL-11004

FROM: Technical Information Division

SUBJECT: UCRL-11004, "Measurements of the Muon-Capture Rate in He^3 and He^4," Robert John Esterling (Ph. D. Thesis), April 9, 1964.

Please make the following corrections on subject report.

Page 14 Equation 20, denominator of first term should read

$$(Gm_p{}^2 [V_\beta{}^2(0) + 3 A_\beta{}^2(0)]$$

Page 25 Equation 43, denominator of last term should be

$$G^2 (V_\beta{}^2 + 3 A_\beta{}^2)$$

Page 128 fourth paragraph, 7th line, Bollard should be Bollaert

Page 159 Reference 6, page given as 466 should be 431
Reference 12, Walsh should be Welsh

Page 161 Reference 28, Petrukhim should be Petrukhin
Muhkin should be Mukhin

MEASUREMENTS OF THE MUON-CAPTURE RATE IN He^3 AND He^4

Contents

MEASUREMENTS OF THE MUON-CAPTURE RATE IN He^3 AND He^4

Robert John Esterling

Lawrence Radiation Laboratory
University of California
Berkeley, California

April 9, 1964

ABSTRACT

A measurement was made of the total muon-capture rates in He^3 and He^4 and the partial capture rate into the channel

$$\mu^- + He^3 \rightarrow H^3 + \nu.$$

Negative muons were brought to rest in a high-pressure helium gas target. The capture processes all yield a charged particle whose energy was measured by observation of scintillation in the helium gas. Captures into the H^3 channel were recognized by the unique energy (1.9 MeV) of the triton recoil. The total capture rates obtained were:

$$\Lambda(He^3) = 2170 \pm \begin{matrix} 170 \\ 430 \end{matrix} \text{ sec}^{-1}$$

$$\Lambda(He^4) = 375 \pm \begin{matrix} 30 \\ 300 \end{matrix} \text{ sec}^{-1}.$$

The large lower limits are due to uncertainties from capture events in the walls surrounding the gas. The partial capture rate to the triton ground state was measured as

$$\Lambda(He^3 \rightarrow H^3) = 1505 \pm 46 \text{ sec}^{-1}.$$

The results are in good agreement with theoretical predictions that are based on the universal Fermi interaction.

I. INTRODUCTION

A. Universal Fermi Interaction

Although the muon was first observed about 1937, it was not until about 1947 that it was recognized that the muon was not the Yukawa particle responsible for nuclear forces. The classic experiment of Conversi, Pancini, and Piccioni[1] provided the first evidence of the competition between muon decay and muon capture and showed that the muon had characteristics that were inconsistent with those of a strongly interacting particle. Soon afterwards, measurement of the muon lifetime led several physicists to observe that beta decay, muon decay, and muon capture could all be characterized by a common interaction with small and approximately equal coupling constants.[2] They suggested that there is one "universal Fermi interaction" (UFI) that describes the coupling of all the weakly interacting particles. Such an interaction can be summarized in the well-known Puppi triangle.

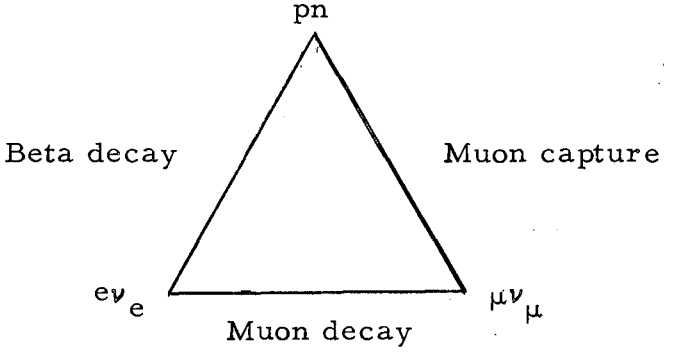

The concept of a UFI was placed on a quantitive foundation by comparison of the vector-coupling constant obtained from O^{14} beta decay with that obtained from the muon-decay rate. These two coupling constants differ by $2 \pm 0.2\%$,[3] but electromagnetic corrections to the beta-decay coupling constant are uncertain and could account for this small difference.[4] Several excellent reviews summarize the present knowledge of beta and muon decay.[5] These interactions seem to be well understood at the present time.

The present experiment investigates the least understood of the strangeness-conserving weak interactions: muon capture. In particular, this experiment measures the muon-capture rates in He^3 and He^4. Comparison with theoretical predictions then tests the hypothesis of UFI in muon capture.

B. Muon Capture

When a positive muon is brought to rest in matter it decays with the same mean life as in free space ($\tau = 2.200 \pm 0.002$ μsec).[6] When a negative muon comes to rest in matter, it goes into Bohr orbits with $n,l \approx 15$, from which it cascades down by x-ray and Auger processes to the 1s atomic state in $\approx 10^{-10}$ sec.[7] When the muon reaches the ground state it either decays according to

$$\mu^- \rightarrow e^- + \nu_\mu + \bar{\nu}_e \qquad (1)$$

or it interacts with the nucleus, with the transformation of a proton into a neutron and the emission of a neutrino, according to the basic reaction,

$$\mu^- + p \rightarrow n + \nu_\mu. \qquad (2)$$

We call this nuclear interaction "muon capture." The capture and decay times are of the order of 1 μsec and thus are much longer than the time required for the muon to slow down and to reach the 1s Bohr orbit.

The atomic system consisting of the muon and the nucleus is initially formed in a statistical mixture of $I \pm \frac{1}{2}$ spin states, in which I is the spin of the nucleus. These two angular-momentum states are called hyperfine states, because they are analogous to hyperfine states in a normal atom. Since the muon-capture rate is spin dependent, a knowledge of the hyperfine state is vital to an interpretation of experimental results.

Muon capture is analogous to K-electron capture. However, because the muon mass is ≈ 200 times as large as the electron mass, the muonic atom has smaller orbits than a normal atom and more energy is available in muon capture. Thus it follows that there is a

greater overlap between the muon and the nuclear wave function and a larger volume of phase space available in muon capture. This makes muon-capture rates much faster than K-electron capture rates so that muon capture competes with free-muon decay. Both the negative-muon-decay rate and the capture rate depend on the atomic number of the nucleus. The decay rate of a muon bound in a 1s Bohr orbit depends on the atomic number (Z), approximately according to the function[8] $1 - \frac{1}{2}(Z/137)^2$, so that for very light elements the decay rate is the same as in free space. For elements with small Z, the capture rate increases like Z^4; a factor Z^3 is due to the increased muon-nuclear wave function overlap ($a_o \approx 1/Z$) whereas the other factor of Z arises from the Z protons in each nucleus. In low-Z materials decay predominates, whereas in high-Z materials the capture process predominates. The capture rate is equal to the decay rate at Z = 12 (magnesium).

Denoting the muon-decay rate by Λ_D and the capture rate by Λ_C, we have for the total rate of the muon's disappearance by either process

$$\Lambda_T = \Lambda_D + \Lambda_C,$$

so that the fraction of all stopped muons surviving to time t is $\exp(-\Lambda_T t)$. In the lighter elements, the total disappearance rate is about equal to the decay rate, so that muon-capture events must be identified by their reaction products. The usual procedure of determining capture rates in the heavier elements is by measuring the total disappearance rate, Λ_T.

When the muon is captured in heavy elements, the neutrino takes away most of the muon's rest energy so that only about 20 MeV remains in the resultant nucleus as excitation energy. Occasionally the neutron produced in the capture interaction carries off most of this excitation energy, but usually the nucleus de-excites by emission of lower energy neutrons and γ rays, and only infrequently by proton emission.

Wolfenstein[9] summarized much of the information available on muon capture up to 1960, and Sard and Crouch summarized some of the earlier work.[10] Telegdi has recently given the experimental evidence for a Fermi interaction in muon capture.[11]

C. Advantages and Disadvantages of Muon Capture in Hydrogen

Much data are available on muon-capture rates in complex nuclei,[12] but the data are difficult to interpret because of the complex problem involving many strongly interacting nucleons and many final states. Ideally, therefore, one would like to study the muon-capture rate in hydrogen[13] where there are no nuclear-structure effects. There are, however, five main reasons why an experiment in He^3, the next simplest nucleus not an isotope of hydrogen, is easier to perform and to interpret. These are:

1. The muon-capture rate in hydrogen is especially sensitive to whether the μ-p atom is in a triplet or a singlet hyperfine state.

2. The μ-p atom is neutral and rapidly diffuses through the hydrogen undergoing collisions with other protons. In these collisions the muon is often exchanged from proton to proton. These exchange collisions rapidly change the original statistical population of 1/4 singlet and 3/4 triplet atoms to 100% singlet μ-p atoms (the ground state of the μ-p system). Furthermore, in liquid hydrogen in about 0.5 μsec the singlet μ-p atom becomes part of a $(p\text{-}\mu\text{-}p)^+$ molecular ion, if the muon has not decayed first. In such an ion the muon can be captured by either proton, and this again changes the probability of capture from a relative singlet or triplet μ-p state. Thus the fraction of captured muons, with spin aligned with or opposite to the capturing proton, varies depending upon whether the p-μ-p ion is in a para or an ortho state. Although calculations show that the molecular ion is almost invariably formed in the ortho state,[14] a mixture of the para and ortho states could change the capture rate considerably. All such variations in the relative-spin states affect the capture rate. In addition, the uncertainty of the molecular wave function in the p-μ-p system causes additional theoretical difficulties

in hydrogen. In helium there are no exchange collisions and the hyperfine states at capture have just their original statistical population.

3. The muon is more tightly bound to all other nuclei (including the deuteron) than it is to hydrogen. Thus any collision with an impurity nucleus has a high probability of transferring the muon from the proton to the impurity nucleus. This exchange is irreversible and, since muon-capture rates are much larger in impurities than in hydrogen, ultrapure hydrogen is required. Again this problem is not present in helium because electrical repulsion keeps the μ-He atom away from other nuclei.

4. To detect muon capture in the lighter elements one must detect the reaction product, which is a neutron in the case of hydrogen and a charged triton in the case of helium. The charged particle can be detected with virtually 100% efficiency whereas it is difficult to determine the neutron-detection efficiency.

5. Finally, the rate for observing the μ-He^3 reaction is more than 100 times that of the μ-p reaction if one includes neutron-detection efficiencies.

The conclusion is that the muon-capture rate in helium can be measured more accurately than the rate in hydrogen. On the other hand, for hydrogen there is no uncertainty in the nuclear structure. This one big disadvantage with capture in helium almost outweighs its favorable features. Nevertheless the hope is that the He^3 nucleus is sufficiently simple to permit an unambiguous theoretical prediction of a capture rate on the basis of a UFI.

D. Muon Capture in He^3 and He^4

When a negative muon is captured by a He^3 nucleus, three principal reactions occur:

$$\mu^- + He^3 \rightarrow H^3 + \nu_\mu \tag{3}$$

$$\mu^- + He^3 \rightarrow H^2 + n + \nu_\mu \tag{4}$$

$$\mu^- + He^3 \rightarrow H^1 + n + n + \nu_\mu . \tag{5}$$

Since there are no known excited states of the triton (H^3) nucleus, Reaction (3) presumably goes directly to the ground state of the triton. This bears a close resemblance to the basic muon-capture Reaction (2). The isodoublet (He^3, H^3) with spin 1/2, called the "trion," is analogous to the proton-neutron doublet. Furthermore, the calculation of the capture rate can be somewhat simplified by use of the ft-value for H^3 to calculate the matrix element for the beta-decay process:

$$H^3 \rightarrow He^3 + e^- + \bar{\nu}_e \,. \qquad (6)$$

This reaction is analogous to the inverse of Reaction (3), and by formation of the ratio of the matrix elements for (3) and (6), some nuclear-structure effects can be approximately cancelled out. Measurement of the $He^3 \rightarrow H^3$ capture rate, Λ_C, therefore appears to be a good way to verify the universality of the Fermi interaction.

Since Reaction (3) has a two-body final state, energy and momentum conservation show that the triton will recoil with a unique (1.90 MeV) energy (see Appendix A). The present experiment is designed primarily to measure the partial capture rate to the triton ground state by observation of this monoenergetic recoil.

Reactions (4) and (5) represent muon captures that result in an unbound triton and are referred to as the breakup reactions in this paper. These breakup reactions involve three- and four-body final states, with the momentum of the charged particle ranging from 0 to about 350 MeV/c. The breakup capture rate, Λ_B, is also measured in this experiment, although with much less accuracy than is Λ_C. The theoretical analysis of the breakup reactions is not so clear-cut as that of Reaction (3); however Yano has recently completed a detailed theoretical analysis of Reaction (4).[15] It is interesting to compare the probability of capture from the same nucleus into various channels. By comparing with experiment the calculations made with a certain set of coupling coefficients, one can test the coefficients and the nuclear wave function better when several channels are involved than when there is only one final state.

To determine Λ_C, we measured the ratio of stopped muons giving a triton recoil (T) to the total number of stopped muons (Sμ).

We have then

$$\Lambda_C = \frac{T}{S\mu} \Lambda_T , \tag{7}$$

where $\Lambda_T = \Lambda_D + \Lambda_C + \Lambda_B$ is the total-muon-disappearance rate, and $\Lambda_D = 4.545 \times 10^5$ sec^{-1} is the muon-decay rate.[6] Similarly the breakup capture rate is

$$\Lambda_B = \frac{E}{S\mu} \Lambda_T , \tag{8}$$

where E is the number of observed breakup events. Only about 1 muon in 300 is captured to the triton ground state, and about 1 in 600 is captured to the breakup states. The remainder decay. One of the experimental problems is to distinguish the decay electron from the relatively rare capture events.

Most of the experimental tests were performed with He^4 before He^3 was put in the target. Consequently a measurement of the muon-capture rate in He^4 was made concomitant with the He^3 measurement. The principal reaction in He^4,

$$\mu^- + He^4 \rightarrow H^3 + n + \nu, \tag{9}$$

is very similar to the breakup Reaction (4), and the experimental analysis is very similar to the analysis of the breakup reactions.

Two previous measurements of the capture rate in He^3 and two in He^4 have been made. Using a He^3-filled diffusion cloud chamber, Falomkin et al. obtained $\Lambda_C = 1410 \pm 140$ sec^{-1} and $\Lambda_B = 730 \pm 180$ sec^{-1}.[16] Using a helium-plus-xenon scintillator, Edelstein et al. first found $\Lambda_C = 1480 \pm 280$ sec^{-1};[17] later they repeated the measurement with an improved apparatus and found $\Lambda_C = 1450 \pm 75$ sec^{-1}.[18] Our experiment is an attempt to make a more precise measurement of Λ_C by the use of helium scintillation. A preliminary account of the $He^3 \rightarrow H^3$ capture-rate measurement was reported previously;[19] the experiment is described and analyzed in greater detail in this article. The slight shift in the value of Λ_C

reflects a more careful analysis of the corrections.

Measurements with He^4 performed in liquid helium bubble chambers indicate a total capture rate close to 400 sec^{-1}.[20,21]

II. THEORETICAL BACKGROUND

Before going on to describe the details of the experiment it seems appropriate to discuss some theoretical questions involved in the prediction of the muon capture rates. The main emphasis is on the calculation of the $He^3 \rightarrow H^3$ capture rate, since the main purpose of the experiment described here is to measure that rate.

A. The Interaction Hamiltonian

In the framework of Fermi's theory of beta decay, the particular interaction responsible for muon decay is of the V-A form. This V-A form is justified by experiment and by the theory of Feynman and Gell-Mann.[22] The interaction Hamiltonian responsible for μ decay is then:

$$\mathcal{H} = \frac{G}{\sqrt{2}} [\bar{u}(e)\,(1-\gamma_5)\,\gamma_\lambda\, u(\nu_e)][\bar{u}(\nu_\mu)\,(1-\gamma_5)\gamma_\lambda\, u(\mu)] + \text{H. C.} \quad (10)$$

Here H. C. means the Hermitian conjugate, G is the weak-interaction coupling constant, the u's are Dirac spinors, and the γ's are the Dirac matrices. The coupling constant evaluated from decay rate of the positive muon is[23]

$$G = 1.0263 \pm 0.0004 \times 10^{-5}/m_p^2 \approx 1.43 \times 10^{-49}\ \text{erg-cm}^3,$$

where m_p is the proton mass.

The basic postulate of the UFI viewpoint is that the same Hamiltonian and the same coupling constant G describe the weak interaction between any four fermions. One has just to replace μ, e, ν_μ, and ν_e by the relevant particles. The hypothesis of universality dictates that the coupling constant is still G and that the interaction is still V-A. Unfortunately, except for muon decay, strong interactions come into play in every weak interaction, and virtual pion effects must be expected to alter the effective interaction. In the particular case of nuclear β decay, the interaction is known to be modified to an effective Hamiltonian

$$\mathcal{H} = \frac{G}{\sqrt{2}} [\bar{u}(e)\,(1-\gamma_5)\,\gamma_\lambda\, u(\nu_e)]\,[\bar{u}(p)\,(V_\beta + A_\beta\,\gamma_5)\,\gamma_\lambda\, u(n)] + \text{H. C.}, \quad (11)$$

where V_β and A_β are the vector and axial-vector coupling coefficients that take strong interactions into account. If one calculates G from the muon-decay rate and tries to determine V_β and A_β, for instance from O^{14} and neutron-beta decay, one finds $V_\beta \approx 1$ and $A_\beta \approx -1.2$. The coupling coefficient V_β is so near to 1.0 that Feynman and Gell-Mann,[22] and independently Gershtein and Zel'dovich,[24] looked for a theory in which V_β should be exactly 1.0, even in the presence of strong interactions. Thus they formulated a theory of conserved vector currents in weak interactions that is closely analogous to the conserved electromagnetic current.

This β-decay interaction [Eq. (11)] is sufficient to describe the situation in the limit of zero-momentum transfer. In muon capture, however, the momentum transfer is of the order of the muon mass and this further modifies the Hamiltonian. The Hamiltonian that is effective in muon capture was first presented by Goldberger and Treiman[25] but later modified by Weinberg[26] to the form:

$$\mathcal{H} = \frac{G}{\sqrt{2}} \left[\bar{u}(n) \left(V\gamma_\lambda + A\gamma_5\gamma_\lambda + M\sigma_{\lambda a} \frac{q_a}{m_p} + T\sigma_{\lambda a}\gamma_5 \frac{q_a}{m_p} + S \frac{q_\lambda}{m_p} + P\gamma_5 \frac{q_\lambda}{m_p} \right) u(p) \right] \left[\bar{u}(\nu_\mu)(1-\gamma_5)\gamma_\lambda u(\mu) \right] + \text{H. C.} \qquad (12)$$

This is the most general interaction Hamiltonian that (a) is Lorentz invariant, (b) has no derivatives in the leptonic fields, (c) reduces to Eq. (10) in the absence of strong interactions, and (d) reduces to Eq. (11) in the presence of strong interactions at zero-momentum transfer. In this Hamiltonian, $q_a = p_a - n_a = \nu_a - \mu_a$ is the four-momentum transfer, $\sigma_{\alpha\beta} = \frac{1}{2}(\gamma_\alpha\gamma_\beta - \gamma_\beta\gamma_\alpha)$, and V, A, M, T, S, and P are the coupling coefficients of the vector, the axial-vector, the weak magnetism, the tensor, the induced scalar, and the induced pseudoscalar terms, respectively. These coupling coefficients are dimensionless functions of q^2 and can all be chosen real if the interaction is time-reversal-invariant. Each coefficient is discussed in Sec. II. B.

B. Coupling Coefficients

In this section, I evaluate the coupling coefficients of Eq. (12) so far as is possible with present theories. The trion is treated as a single Dirac particle as opposed to a composite of nucleons, and the nucleon spinors of Eq. (12) are replaced by trion spinors. This analysis is similar to that given in references 23 and 27, in which all nuclear-structure effects are absorbed into the coupling coefficients.

1. Vector and "Weak Magnetism" Coefficients

The vector V and weak-magnetism M coefficients in the Hamiltonian (12) are the only coefficients that can be determined with some degree of confidence. This is because the conserved-vector-current (CVC) theory[22] seems to be valid in nuclear and pion-beta decay,[28] and thus should also apply in muon capture. The coefficients V and M can then be related directly to the electric and magnetic-isovector-form factors measured in electron scattering.

The electromagnetic current can be written[29]

$$
\begin{aligned}
j_\mu^{e.m.} &= \frac{1}{2}\, e\,\overline{\psi}_N \left[(F_1^S + F_1^V \tau_3)\,\gamma_\mu + (F_2^S + F_2^V \tau_3)\,\sigma_{\mu\nu} q_\nu \right] \psi_N \\
&= \frac{1}{2}\, e\,\overline{He} \left[(F_1^S + F_1^V)\,\gamma_\mu + (F_2^S + F_2^V)\,\sigma_{\mu\nu} q_\nu \right] He \qquad (13) \\
&+ \frac{1}{2}\, e\,\overline{H} \left[(F_1^S - F_1^V)\,\gamma_\mu + (F_2^S - F_2^V)\,\sigma_{\mu\nu} q_\nu \right] H \\
&= \overline{He}\,(2eF_1^{He}\gamma_\mu + K_{He}\mu_N F_2^{He}\sigma_{\mu\nu} q_\nu)\,He + \overline{H}\,(eF_1^H \gamma_\mu + K_H \mu_N F_2^H\, \sigma_{\mu\nu} q_\nu) H
\end{aligned}
$$

where

$$
\psi_N = \begin{pmatrix} He \\ H \end{pmatrix}, \qquad \tau_3 = \begin{pmatrix} 1 & 0 \\ 0 & -1 \end{pmatrix},
$$

He and H refer to the He^3 and H^3 wavefunctions, K is the anomalous magnetic moment measured in units of μ_N, the nuclear magneton, and the F's are the electromagnetic form factors and are functions of q^2, the four-momentum transfer. The subscripts 1 and 2 on the F's refer to the Dirac and Pauli form factors and the superscripts

S and V refer to the isoscalar and isovector components of F_1 and F_2. The factors F_i^{He} and F_i^{H} are actually measured in an experiment and F_i^{V} can be related to them by identifying terms in Eq. (13). Thus

$$F_1^V = 2F_1^{He} - F_1^H$$

$$F_2^V = \frac{\mu_N}{e} (K_{He} F_2^{He} - K_H F_2^H) \tag{14}$$

where F^{He} and F^H are normalized to unity at zero momentum transfer.

Now according to CVC theory the weak vector current is just related to $j_\mu^{e.m.}$ by replacement of e by $G/\sqrt{2}$ and τ_3 by τ_+ in the first part of Eq. (13) and by the circumstance that $F^S(\text{weak}) = 0$. Thus

$$j_\mu^{weak} = \frac{G}{2\sqrt{2}} \bar{\psi}_N [(F_1^S + F_1^V \tau_+) \gamma_\mu + (F_2^S + F_2^V \tau_+) \sigma_{\mu\nu} q_\nu] \psi_N$$

$$= \frac{G}{\sqrt{2}} \bar{H} [F_1^V \gamma_\mu + F_2^V \sigma_{\mu\nu} q_\nu] \text{ He.} \tag{15}$$

By comparing terms in this equation and in the Hamiltonian (12), one obtains with the aid of Eq. (14)

$$V(q^2) = F_1^V(q^2) = 2 F_1^{He}(q^2) - F_1^H(q^2)$$

$$\frac{M(q^2)}{m_p} = F_2^V(q^2) = \frac{\mu_N}{e} [K_{He} F_2^{He}(q^2) - K_H F_2^H(q^2)]. \tag{16}$$

Collard et al.[32] give the rms charge and magnetic-moment radii for He^3 and H^3. These results are listed in Table I along with other properties of the trions. All of the radii were obtained by means of a Gaussian model, except that of the charge radius of He^3 for which a hollow-exponential model was used. One can find the form factor at a given momentum transfer q by using the formula[33]

Table I. Some properties of He^3 and H^3.

	He^3	H^3
1. Mass[a] (MeV)	2808.23±0.03	2808.76±0.03
2. Magnetic moment[b] (nuclear magnetons)	-2.1274	+2.9788
3. Anomalous magnetic moment		
(nuclear magnetons)	-2.7956	+2.6448
(trion magnetons)	-8.3676	+7.9177
4. Charge radius[c] (fermis)	1.97±0.10	1.68±0.16
Magnetic moment radius (fermis)	1.69±0.10	1.63±0.16
5. $F_{ch} \approx F_1 (q^2 = 0.2735F^{-2})$	0.840±0.041	0.879±0.065
F_{mag}	0.878±0.041	0.886±0.065
F_2	0.869±0.041	0.887±0.065

a. See Ref. 30

b. See Ref. 31

c. See Ref. 32

$F(qa) = \exp(-(qa)^2/6)$ for the Gaussian model and
$F(qa) = [1-(qa)^2/60]/[1+(qa)^2/20]^3$ for the hollow exponential model, where a is the rms radius. Since q = 103.2 MeV/c = 0.5231 F^{-1} is the momentum transfer in (μ-He^3) capture, one can obtain the values of F_{ch} and F_{mag} given in Table I. These are related to F_1 and F_2 by the formulas[32]

$$F_{ch} = F_1 - \frac{q^2 K}{4m_t^2} F_2$$
$$F_{mag} = (F_1 + K F_2)/(1 + K) \qquad (17)$$

where m_t is the trion mass and K is the anomalous magnetic moment. Values of F_1 and F_2 obtained from these formulas are also given in Table I. Substitution of these values of F_1 and F_2 into Eq. (16) gives

$$V(q^2 = 0.2735\ F^{-2}) = 0.80 \pm 0.10$$
(trion) (18)
$$M(q^2 = 0.2735\ F^{-2}) = -2.39 \pm 0.10.$$

Note that $V(0) = V_\beta = 1.0$ and $M(0) = \frac{1}{2}(K_{He} - K_H) = -2.72$ and that $V(q^2)/V(0) = 0.80$, $M(q^2)/M(0) = 0.88$.

The above discussion also applies to the coupling coefficients for a single nucleon if one makes the replacements: $p \leftrightarrow He$, and $n \leftrightarrow H$. F_1 and F_2 then have the form[34]

$$V(q^2) = F_1^V(q^2) = -0.20 + \frac{1.20}{1 + 0.10q^2} = 0.97 \qquad \text{(nucleon)} \quad (19)$$

$$M(q^2)/m_p = F_2^V(q^2) = \frac{K_p - K_n}{2\,m_p} F_1^V(q^2) = 1.797/m_p$$

where $K_p = 1.793$ and $K_n = -1.913$ are the anomalous magnetic moments in units of the nuclear magneton.

Note that the sign of $M(q^2)$ for the nucleon is opposite that for the trion. One way to understand this opposite sign is by considering He^3 and H^3 as a closed-shell nucleus, He^4, minus a neutron or a proton. The missing particle (hole) gives He^3 and H^3 the properties of an antineutron and antiproton respectively. Since the magnetic moments of the antinucleons are opposite in sign from those of the nucleons, the weak magnetism coefficient must also have opposite sign.

2. Axial-Vector Coefficient

The axial-vector coefficient at zero-momentum transfer A(0) can be found from the beta-decay rate of tritium. The ft value of H^3 was measured[35] to be 1132 ± 40 sec and can be calculated from the formula[5]

$$ft = \frac{2\pi^3 \ln 2}{(Gm_p^2)^2 (V_\beta^2(0) + 3A_\beta^2(0)} \left(\frac{m_p}{m_e}\right)^4 \frac{\hbar}{m_e c^2} \qquad (20)$$

where f is the usual dimensionless integral over the electron-energy spectrum

$$f(Z, E_{max}) = \int_1^{E_{max}} F(Z, E)\,(E_{max} - E)^2\, E \sqrt{E^2 - 1}\; dE, \qquad (21)$$

where $F(Z, E)$ is the Fermi function that takes into account the Coulomb repulsion of the electron from the nucleus, and E is measured in units of the electron mass, m_e. By the hypothesis of the CVC theory, $V_\beta(0) = 1.0$ and one may solve for $|A_\beta(0)| = 1.194 \pm 0.037$. By the principles of UFI, $A_\beta(0)$ in beta decay is the same coefficient as that in muon capture and therefore for the trion, we have

$$|A(0)| = 1.194 \pm 0.037. \qquad \text{(trion)} \quad (22)$$

Similar analysis for the nucleon gives

$$|A(0)| = 1.20 \pm 0.04\ . \qquad \text{(nucleon)} \quad (23)$$

The experiments on muon capture in hydrogen have established that for the nucleon the sign of A is opposite to that of V,[13] that is that we have a V-A theory. For the trion, A must have the sign opposite to that of the axial-vector coefficient of the nucleon, again because of the correspondence $He^3 \leftrightarrow He^4 + \bar{n}$ and $H^3 \leftrightarrow He^4 + \bar{p}$. This is most easily seen by manipulating the nuclear part of the axial-vector matrix element as follows:

$$\bar{u}(\bar{p})\gamma_5\gamma_\lambda u(\bar{n}) = u(\bar{n})\, CC^{-1}(\gamma_4^*\gamma_5^*\gamma_\lambda^*)^\dagger CC^{-1}\, u^*(\bar{p})$$

$$= u^*(n)\gamma_2\gamma_\lambda^*\gamma_5\gamma_4\gamma_2\, u(p) = -\bar{u}(n)\gamma_5\gamma_\lambda\, u(p) \qquad (24)$$

where I have used the usual representation of the γ matrices

$$\vec{\gamma} = \begin{pmatrix} 0 & +i\vec{\sigma} \\ -i\vec{\sigma} & 0 \end{pmatrix} \qquad \gamma_4 = \begin{pmatrix} +1 & 0 \\ 0 & -1 \end{pmatrix} \qquad \gamma_5 = \begin{pmatrix} 0 & 1 \\ 1 & 0 \end{pmatrix} \qquad (25)$$

where $\vec{\sigma}$ is the Pauli spin matrix and 1 is the 2×2 unit matrix. In this representation the charge conjugation operator $C = C^{-1} = \gamma_2$. In Eq. (24) the He^3/H^3 states have been replaced by the $\bar{n}/\bar{p}$ states (the closed-shell He^4 nucleus can be considered a spectator since it appears on both sides of the reaction). Thus the axial-vector term reverses sign on going from the reaction $\mu^- He^3 \to H^3\nu$ to the reaction

$\mu^- p \rightarrow n\nu$. Therefore since $A(0) = -1.20\ V(0)$ for the nucleon, $A(0) = +1.194\ V(0)$ for the trion.

There is no proven theory or experimental information for the dependence of A on q^2 in the case of the trion. One can hypothesize that, since the axial-vector term and the weak-magnetism term in the Hamiltonian reduce to the same form in the nonrelativistic limit, $A(q^2)/A(0) = M(q^2)/M(0)$. An alternative choice is that this ratio is equal to $V(q^2)/V(0)$. Strictly speaking, however, nothing is known of the momentum dependence of A, but A is expected to be within $\approx 10\%$ of +1.0.

In the case of the nucleon, a dispersion-theoretical argument indicates that[36]

$$\frac{A(q^2)}{A(0)} \approx 1 - \frac{q^2}{4\pi m_p^2} = 0.999. \qquad (26)$$

However, the momentum dependence of A for the trion is expected to be much greater than this because of nuclear-structure effects.

3. Induced-Pseudoscalar Coefficient

Even less is known about the value of the induced pseudoscalar coefficient, $P(q^2)$, than is known about $A(q^2)$. Dispersion-theoretical arguments,[25] which use the one-pion-exchange model, give for the nucleon

$$\frac{m_\mu}{m_p} P(q^2) = \frac{2m_\mu m_p A(0)}{q^2 + m_\pi^2} = 6.6\ A(0) = -7.9. \qquad \text{(nucleon)} \quad (27)$$

In the case of the trion, the proton mass must be replaced by the trion mass and one obtains

$$\frac{m_\mu P(q^2)}{m_p} = \frac{2m_\mu m_3}{q^2 + m_\pi^2} A(0) = 19.7\ A(0) = +23.5. \qquad \text{(trion)} \quad (28)$$

An additional correction for many-body effects is probably also necessary for $P(q^2)$ of the trion, but since the dispersion argument is so uncertain this additional factor of 0.8 to 0.9 has been neglected.

Measurements of the angular distribution of neutrons from muon capture in calcium[37] and measurements of muon capture[38] in O^{16} populating discrete levels of N^{16} yield values of P/A (nucleon) between 5 and 30, depending on the experiment and its interpretation. Most measurements are consistent with a P/A ratio close to 10.

4. Induced Scalar and Tensor Coefficients

Absolutely nothing is known about the values or the signs of the S and T coefficients. These are the "second class" terms which, as Weinberg pointed out,[26] could also be present in the Hamiltonian. The symmetry of the S and T terms under G, defined as the product of charge conjugation and a 180° rotation about the y axis in isotopic-spin space, is opposite to that of the V and A terms. Most authors assume that the weak currents have a definite G-conjugation parity (that of the V and A terms) and that therefore S = T = 0. If S and T are not zero, Weinberg guesses that they are of the same magnitude as V. If this is the case, these second-class terms could radically affect the capture rate in both hydrogen and helium.

C. Hyperfine Effect

A simple theory that has V = -A coupling and no other coupling in Eq. (12) has the peculiar feature that no capture takes place in a muonic atom in the hyperfine-triplet states. This is because in the nonrelativistic limit the vector operator γ_λ reduces to unity, whereas the axial-vector operator $\gamma_5\gamma_\lambda$ reduces to $\vec{\sigma}$, the spin matrix. Thus the matrix element becomes proportional to $V + A\ \vec{\sigma}_\mu \cdot \vec{\sigma}_p$. The term $\vec{\sigma}_\mu \cdot \vec{\sigma}_p$ can be evaluated from the relation

$$(\vec{S}_\mu + \vec{S}_p)^2 = S_\mu^2 + S_p^2 + 2\vec{S}_\mu \cdot \vec{S}_p = \frac{3}{4} + \frac{3}{4} + \vec{\sigma}_\mu \cdot \vec{\sigma}_p/2 \qquad (29)$$

where the spin $\vec{S} = \vec{\sigma}/2$ and $S^2 = S(S+1)$. The capture rate, which is proportional to the square of the matrix element, becomes in the singlet and triplet cases

$$\Lambda_s \approx |V - 3A|^2 \quad \text{and} \quad \Lambda_t \approx |V + A|^2. \qquad (30)$$

Thus if the coefficient V = -A (as in muon capture in hydrogen), $\Lambda_t = 0$. In the case of capture in He^3, $V \approx +A$ (see Sec. II. B), and in the simple theory there is no dependence on the hyperfine state.

In actual practice $|V|$ is not exactly equal to $|A|$ and there are other terms in Hamiltonian [Eq. (12)]. These factors modify the singlet and the triplet rate as given by the simple theory but the same tendencies persist. For example, in hydrogen the singlet and triplet rates are 713 sec^{-1} and 16.9 sec^{-1}, respectively,[39] whereas in He^3 they are 1806 sec^{-1} and 1312 sec^{-1}, as calculated in Sec. II. D. Thus it is important to know the relative fraction of singlet and triplet states at time of capture.

The energy splitting of hyperfine states is given by the formula[40]

$$\Delta E = \frac{8}{3} \mu_o M \left(\frac{Z_{eff}}{a_o}\right)^3 \left(\frac{2I+1}{I}\right), \qquad (31)$$

where μ_o is the muonic Bohr magneton, M is the actual magnetic moment of the nucleus, a_o is the Bohr radius, I is the nuclear spin, and Z_{eff} is the effective charge in muon capture (see Ref. 12a). For positive M, the hyperfine level with $F = I - 1/2$ is lower in energy. In He^3, for which $Z_{eff} \approx Z$ and $M = -2.1274\ \mu_N$, the hyperfine splitting is ≈ 1.4 eV and the triplet level has the lower energy. The question that remains is whether transitions take place between hyperfine levels during the lifetime of the muon.

Winston and Telegdi have investigated hyperfine transitions in muonic atoms both theoretically and experimentally.[41] They find that transitions take place by internal conversion (electron ejection) at rates comparable to the muon's lifetime in the lighter elements. In particular in F^{19} the calculated transition rate of 5.8×10^6 sec^{-1} is in excellent agreement with the observed rate close to 6.0×10^6 sec^{-1}. However, in He^3 there is not enough energy available in the hyperfine transition to eject the single K electron that surrounds the μ-He^3 atomic system. Thus, if internal conversion is the major cause of hyperfine transitions (as Winston's work seems to show), there should be no transitions between the hyperfine levels in He^3 during the muon's

lifetime and the hyperfine states should have just their original statistical population. It should be emphasized again that this is not the case in hydrogen, for which exchange collisions provide the mechanism for hyperfine transitions.

It would be interesting to induce transitions between the hyperfine levels in He^3, to obtain a nonstatistical distribution between the singlet and triplet states. For, if η is the fraction of muonic atoms in the hyperfine singlet state, then the capture rate is given by

$$\Lambda_C = \eta \Lambda_s + (1-\eta) \Lambda_t. \tag{32}$$

The rates Λ_s and Λ_t are essentially independent and, in principle, measurement of Λ_C at two values of η allows a determination of both Λ_s and Λ_t. In practice, inducing hyperfine transitions is not easy and the determination of η is difficult.

D. $He^3 \rightarrow H^3$ Capture Rate - Method I

This method of calculating Λ_C, the capture rate of Reaction (3), was recently proposed by Fujii and Yamaguchi[23] and independently by Drechsler and Stech.[27] In this calculation the free trion is assumed to satisfy the Dirac equation and the nucleon spinors of Eq. 12 are replaced by trion spinors. All the nuclear-structure effects are absorbed into the coupling coefficients analogously to the way nuclear structure is absorbed into the electromagnetic-form factors in electron-nucleon scattering. Thus the calculation is completely relativistic and is as accurate as the single-proton calculation. The difficulties that remain are to fix the coupling coefficients for the trion and to interpret the trion results in terms of single proton capture.

The capture rate can be obtained directly from the calculation of Adams for proton capture.[39] One has merely to interpret his results in terms of the trion. The results for the singlet and triplet capture rates follow:

$$\Lambda_o = \frac{(Gm_p^2)^2}{2\pi^2}\left(\frac{Za\,m'_\mu}{m_p}\right)^3\left(\frac{k^2}{E+k}\right)\frac{m_p\,(0.98)}{\hbar} = 115.4\ \text{sec}^{-1} \quad (33)$$

$$\begin{aligned}\Lambda_s = \Lambda_o \Big| &(5E+3k-4m)^{1/2}\,V - (5E+3k+4m)^{1/2}A \\ &+\left[\frac{5}{2}k^2E + \frac{3}{2}k^2m - 3kw\,(E-m) + \frac{9}{2}w^2\,(E-m) - 2k^3 + 6k^2w\right]^{1/2} M \\ &+\left[\frac{5}{2}k^2E - \frac{3}{2}k^2m - 3kw\,(E+m) + \frac{9}{2}w^2\,(E+m) - 2k^3 + 6k^2w\right]^{1/2} T \\ &+ (w-k)\left(\frac{E+m}{2}\right)^{1/2} S - (w-k)\left(\frac{E-m}{2}\right)^{1/2} P\Big|^2 . \end{aligned} \quad (34)$$

$$\begin{aligned}\frac{\Lambda_t}{\Lambda_o} = {} & (E+k/3)\,|V+A|^2 - 1/6\left[4k^2E + 6k^2w + 4wkE + 3k^3 - kw^2\right] M\,T \\ & + 1/6\left[3w^2(E-m) + 7k^2E + k^2m + 4wk^2 + 4k^3 - 2kw\,(E-m)\right] M^2 \\ & + 1/6\left[3w^2\,(E+m) + 7k^2E + k^2m + 4wk^2 + 4k^3 - 2kw\,(E+m)\right] T^2 \\ & + 1/2\,(w-k)^2\left[(E+m)\,S^2 + (E-m)\,P^2 + (2/3)k\,S\,P\right] \\ & + 1/3\left[3E\,(w-k) - mk - 3mw + k\,(w-k)\right]\,(V+A)\,M \\ & + 1/3\left[3E\,(w-k) + mk + 3mw + k\,(w-k)\right]\,(V+A)\,T \\ & + 1/3\,(w-k)\left[3\,(E+m) + k\right]\,(V+A)\,S \\ & + 1/3\,(w-k)\left[3\,(E-m) + k\right]\,(V+A)\,P \\ & - 1/3\,(w-k)\left[3k^2 + 2k\,(E+m) - kw\right] M\,S \\ & + 1/3\,(w-k)\left[2k^2 + 3w(E+m) - k\,(E+m)\right] T\,S \\ & + 1/3\,(w-k)\left[2k^2 + 3w\,(E-m) - k\,(E-m)\right] M\,P \\ & - 1/3\,(w-k)\left[3k^2 + 2k\,(E-m) - kw\right] T\,P\ . \end{aligned} \quad (35)$$

Here k, E, and m are the triton's momentum, total energy, and rest mass, and $w = E - m(He^3)$ is the fourth component of the four-momentum transfer. These variables are all in units of the proton mass. The 0.98 in Λ_o is the correction factor for the muon-wave function due to the finite size of the trion, m'_μ is the reduced mass of the muon, α is the fine-structure constant, and $Z = 2$ is the charge of the He^3 nucleus.

If the following coupling coefficients

V = 0.80	M = -2.39	S = 0	
A = 1.00	P = 208.7	T = 0	(36)

discussed Sec. II. B are used to calculate the capture rates, one obtains $\Lambda_s = 1806\ \text{sec}^{-1}$ and $\Lambda_t = 1312\ \text{sec}^{-1}$, which combine to give $\Lambda_C = 1/4\,\Lambda_s + 3/4\,\Lambda_t = 1435\ \text{sec}^{-1}$ for a statistical population. If each coupling coefficient is varied one at a time from the values given in Eq. (36), the effect on the capture rate is shown in Fig. 1. Note that Λ_C is not especially sensitive to V but is over three times more sensitive to A. Also note that Λ_s is especially sensitive to small changes in P. Thus if a measurement of the $He^3 \rightarrow H^3$ capture rate from the hyperfine singlet state were possible, P could be determined rather accurately.

The present uncertainties in A and P, as well as those in S and T, make an accurate verification of the UFI hypothesis difficult. These difficulties arise because of the presence of strongly interacting nucleons and because of the large-momentum transfer involved in muon capture. There are so many parameters that practically any capture rate near $1500\ \text{sec}^{-1}$ can be calculated with an appropriate choice of the coupling coefficients. Only if both S and T are zero is there hope of verifying UFI to any accuracy less than 10%. These questions are discussed further in Section V.

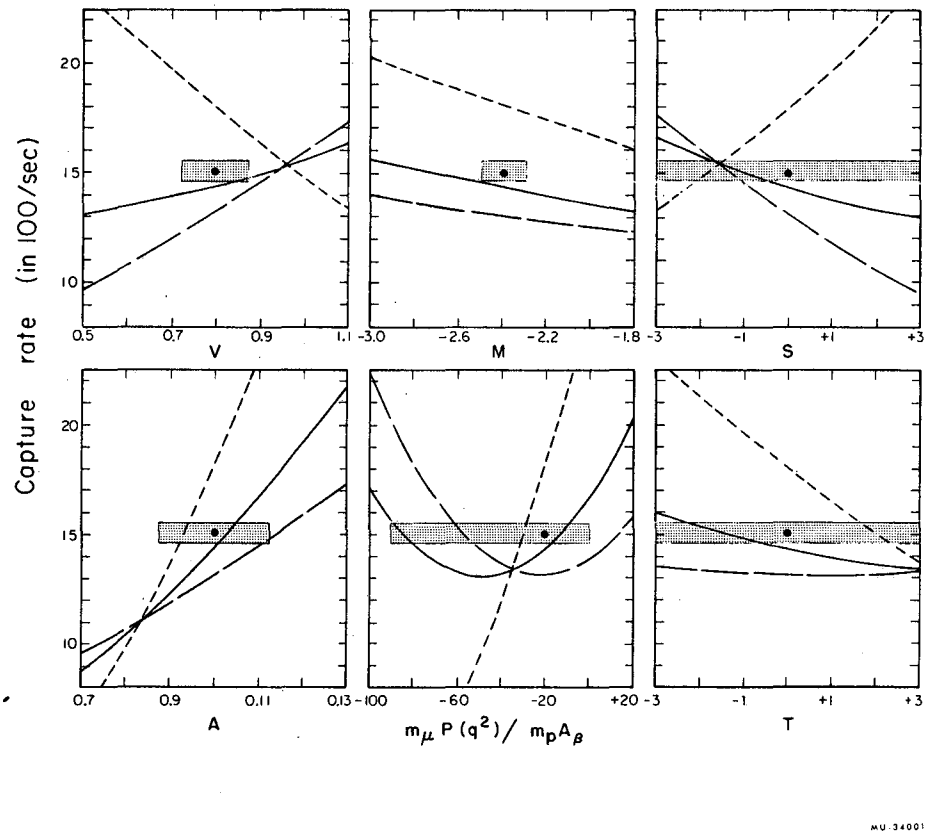

Fig. 1. Effect on the $He^3 \rightarrow H^3$ capture rate as each coupling coefficient is varied from the values given in Eq. (36). The hyperfine-singlet capture rate, Λ_s (· · ·) is given by Eq. (34); the triplet rate, Λ_t (– – –) is given by Eq. (35); total rate (——), $\Lambda_C = 1/4\,\Lambda_s + 3/4\,\Lambda_t$. The dot in each graph represents the intersection of the measured capture rate and the coupling coefficients of Eq. (36) with uncertainty indicated by the shaded area.

E. $He^3 \rightarrow H^3$ Capture Rate - Method II

This section outlines the method of calculating the $He^3 \rightarrow H^3$ capture rate that is given by Fujii and Primakoff.[36] The essential feature of this method is that the ratio of the nuclear matrix element for muon capture and for tritium-beta decay is used to eliminate some of the uncertainty due to nuclear structure. The calculation is nonrelativistic, treats the trion as an aggregate of three nucleons, and does not include the S and T terms of the Hamiltonian [Eq. (12)].

The first step in this method is to calculate the capture rate, Λ_C, in terms of the nuclear matrix element expressed as a sum over the three nucleons in He^3. By using a nonrelativistic expansion of the Hamiltonian, expressing M in terms of V via Eq. (19), summing over all spin orientations of the neutrino and the triton, integrating over all directions of emission of the neutrino, and averaging over the muon-He^3 hyperfine states, one can obtain the capture rate in the following form:

$$\Lambda_C = \frac{(2\pi)\,(4\pi)p_\nu^{\,2}}{(2\pi)^3}\left(1 - \frac{p_\nu}{m_\mu + m_{He}}\right)\frac{(Z\alpha m'_\mu)^3}{2\pi}\,\frac{\left|M^{\mu}_{nucl}(He^3 \rightarrow H^3)\right|^2}{(2\,I_{He}+1)}, \tag{37}$$

where $p_\nu = 103.2$ MeV/c is neutrino's momentum, $\hbar = c = 1$, and $I_{He} = 1/2$ is the spin of the He^3 nucleus. The nuclear-matrix element, with several approximations (such as neglect of terms proportional to p_ν/m_p) becomes

$$\left|M^{\mu}_{nucl}(He^3 \rightarrow H^3)\right|^2 = \int \frac{d\hat{p}_\nu}{4\pi} \sum_{\substack{\text{spins of} \\ He^3,\ H^3}} \left[G_V^2 \left| \left\langle H^3 \left| \sum_{j=1}^{3} \tau_j^- \exp(-i\vec{p}_\nu \cdot \vec{r}_j)\phi(r_j) \right| He^3 \right\rangle \right|^2 \right.$$

$$\left. + \Gamma_A^2 \left| \left\langle H^3 \right| \sum_{j=1}^{3} \tau_i^- \exp(-i\vec{p}_\nu \cdot \vec{r}_j)\phi(r_j)\,\sigma_j \left| He^3 \right\rangle \right|^2 \right], \tag{38}$$

where

$$
\begin{aligned}
G_V/G &\equiv V(1 + p_\nu/2m_p), \\
\Gamma_A^{\,2} &\equiv G_A^{\,2} + 1/3(G_P^{\,2} - 2G_P G_A), \\
G_A/G &\equiv A - V(1 + K_p - K_n)\, p_\nu/2m_p, \\
G_P/G &\equiv \left(\frac{m_\mu}{m_p} P - A - V(1 + K_p - K_n)\right) p_\nu/2m_p,
\end{aligned}
\tag{39}
$$

$\phi(r_i)$ is the muon-spatial-wave function taken at the position of the ith nucleon, τ_i^- is the isotopic-spin operator that transforms the ith proton state into the ith neutron state, $\vec{r}_i$ is the space coordinate of the ith nucleon, and σ_i is the spin operator for the ith nucleon. Note that in the matrix element (38) the H^3 and He^3 nuclei are considered not as a single Dirac particle, but as an aggregate of three nucleons. Thus the coupling coefficients in Eq. (39) must be taken to be the same as an isolated nucleon, in contrast with the trion coefficients discussed in Sec. II. B.

The second step in this calculation is finding the triton-beta-decay-transition rate, in which the roles of the He^3 and H^3 nuclei are interchanged. This calculation yields the beta-decay rate

$$
\lambda_\beta = \frac{(4\pi)^2}{(2\pi)^6} \frac{2\pi f m_e^{\,5}}{2I_H + 1} \left| M^\beta_{\text{nucl}}(H^3 \rightarrow He^3) \right|^2 \tag{40}
$$

with

$$
\left| M^\beta_{\text{nucl}}(H^3 \rightarrow He^3) \right|^2 =
$$

$$
\sum_{\substack{\text{spins of} \\ He^3;\, H^3}} \left[(GV_\beta)^2 \left| \left\langle He^3 \right| \sum_{i=1}^{3} \tau_i^{\,+} \left| H^3 \right\rangle \right|^2 + (GA_\beta)^2 \left| \left\langle He^3 \right| \sum_{i=1}^{3} \tau_i^{\,+} \sigma_i \left| H^3 \right\rangle \right|^2 \right]
\tag{41}
$$

where V_β and A_β are the usual vector and axial-vector coupling constants of beta decay [see Eq. (11)] and f is given by Eq. (21).

The third step of the calculation is to form the ratio of the transition rates in muon capture and beta decay. Since $I_{He} = I_H$ one obtains

$$\frac{\Lambda_C}{\lambda_\beta} = \pi p_\nu^2 \left(1 - \frac{p_\nu}{m_\mu + m_{He}}\right) \frac{(Z\alpha m_\mu)^3}{f m_e^5} \frac{|M^\mu_{nucl}(He^3 \to H^3)|^2}{|M^\beta_{nucl}(H^3 \to He^3)|^2}, \qquad (42)$$

$$= 3.05 \times 10^6 \times R,$$

where R is the ratio of the nuclear-matrix elements. The problem now is to evaluate R. The ratio R is close to unity and relatively independent of the nuclear model. Nonetheless, most of the uncertainties in this calculation arise because of the uncertainty in R. Fujii and Primakoff obtain the following formula

$$R \approx \left(1 + \frac{x}{15}\right)^{-5} \left[1 - \frac{2\alpha Z m'_\mu}{p_\nu}\left(\frac{3x}{4}\right)^{1/2}\left(\frac{1-5x/18}{1-x/6}\right)\right]\left[\frac{G_V^2 + 3\Gamma_A^2}{G(V_\beta^2 + 3A_p^2)}\right] \qquad (43)$$

where

$$x = p_\nu^2 \langle r^2 \rangle,$$
$$\langle r^2 \rangle = \int r^2 \rho(r)\, d^3r \qquad (44)$$

is the mean-square radius, and $\rho(r)$ is some density distribution of protons in the He^3 nucleus. The interpretation of $\langle r^2 \rangle$ (or alternatively of ρ) is ambiguous in this calculation, but on the basis of a variational-trial-wave function, Fujii and Primakoff obtain $(\langle r^2 \rangle)^{1/2} = 1.78F$. In electron-scattering experiments, Collard et al.[32] obtained 1.97F for the charge radius of He^3 and 1.69F for the magnetic-moment radius. These radii are considerably different but they average to 1.83F, so a value of the rms radius close to 1.83F might be appropriate. This ambiguity in the nuclear radius is related to the uncertainty of $A(q^2)$ for the trion that was discussed in Sec. II. D.

If one uses $\langle r^2 \rangle = (1.83F)^2$, the values of G_V and Γ_A given by the coupling coefficients of the nucleon,

$$V = 0.97 \qquad \frac{m_\mu P}{m_p} = -7.9 \qquad V_\beta = 1.0$$
$$A = -1.2 \qquad A_\beta = -1.2 \tag{45}$$

one obtains $R \approx 0.808$. This value, together with $ft = 1132 \pm 40$ sec and by means of Eq. (42), yields

$$\Lambda_C = 3.05 \times 10^6 \ln(2) R/ft = 1518 \text{ sec}^{-1}. \tag{46}$$

Several authors have calculated the $He^3 \rightarrow H^3$ capture rate, but they differ in the choice of a wave function used to evaluate R, in the choice of the coupling coefficients, or in the value of the nuclear radius.[36, 42-46] Figure 2 shows the dependence of Λ_C on the nuclear radius and on the various coupling coefficients.

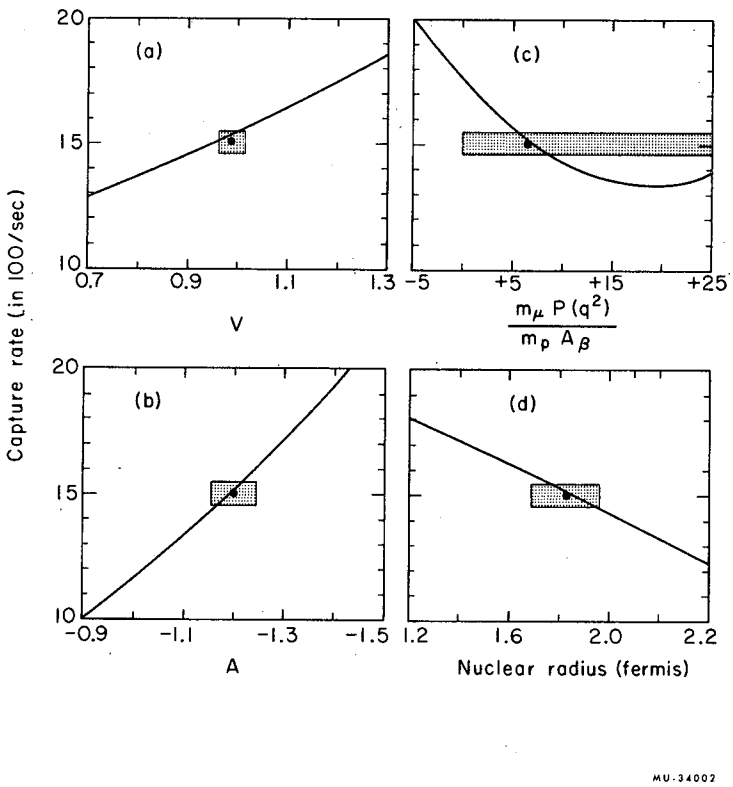

Fig. 2. Dependence of Λ_C, as given by Eqs. (43) and (46), on (a) the vector-coupling coefficient, (b) the axial-vector-coupling coefficient, (c) the induced pseudoscalar coefficient, and (d) the nuclear radius. Each parameter is varied one at a time from the central values given in Eq. (45). The dot in each graph represents the intersection of the measured capture rate and the central value of the parameter with uncertainty indicated by the shaded area.

III. DESCRIPTION OF THE EXPERIMENT

The main purpose of the experiment is to measure $\Lambda_C = \Lambda_T \, T/S\mu$. To show how this is done, I first outline the experimental method used in determining the number of stopped muons, $S\mu$, and the number of triton recoils, T. Then I present a more detailed discussion of the beam, the target, the electronics, and the data.

A. General Technique

Figure 3 is a rough schematic diagram of the system. A beam of negatively charged particles, extracted from the cyclotron, were momentum analyzed and focused on the helium target. The muon component of the beam was identified by a time-of-flight coincidence ($B\mu$) and by range. The helium gas served three purposes: (a) as a target for the muon-capture process, (b) as a scintillation detector for muons that came to rest in the gas, and (c) as an energy spectrometer for measuring the energy of delayed events. A cup-shaped plastic scintillation counter (5) enclosed the gas, leaving only the beam-entrance direction free, and signaled muons that passed through the gas without stopping. Thus a stopped muon ($S\mu$) was identified electronically by a prompt coincidence of $B\mu$ and the He counter (4) with an anticoincidence signal (veto) from the cup counter (5), i.e., $S\mu = B\mu \, \text{He} \, \bar{5}$. Delayed pulses from the He counter, occurring in the interval 0.2 to 6.4 μsec after $S\mu$, triggered the coincidence circuit TR and were then sorted on the basis of pulse height and timing. Counters 3 and 5, which surround the gas, were used to detect $\mu \rightarrow e$ decays, and any TR event that was associated with a pulse in counters 3 or 5 was vetoed. True triton recoils have a range of only 1.7 mm (at 28.9 atm) in the gas and were not vetoed. Thus, a TR event is of the type TR = $S\mu$ (delayed He $\bar{3}$ $\bar{5}$). Such events opened a gate and allowed the He pulse height to be measured on a pulse-height analyzer (PHA). The resulting energy spectrum and the number of counts $S\mu$ form the basic data.

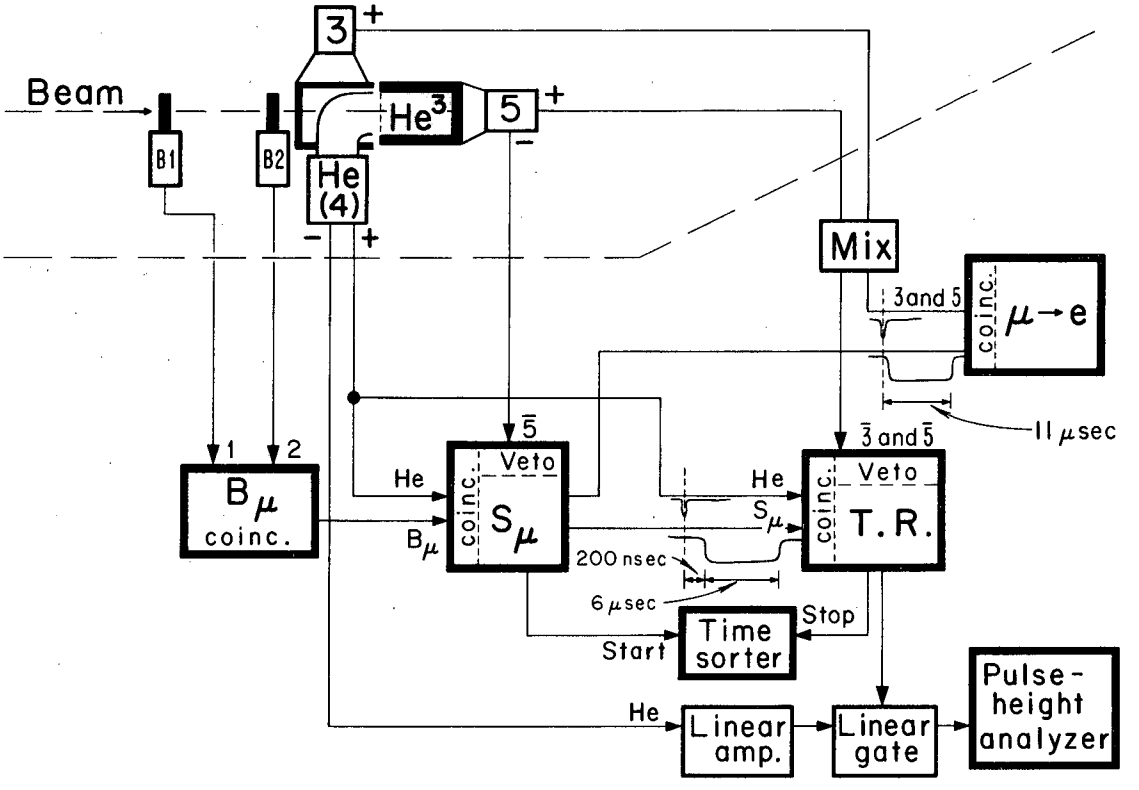

Fig. 3. Rough diagram of the apparatus showing a simplified schematic of the electronics logic.

B. The Target

Figure 4 shows the apparatus. Helium gas at liquid nitrogen temperature (80°K) was held in a cylindrical stainless steel vessel with Lucite end windows. The maximum gas pressure was 28.9 atmospheres, which gave a gas thickness of 240 mg/cm^2 (carbon equivalent) in the beam direction. (All pressures in this paper are absolute.) Appendix B describes the procedure used in handling the gas. The gas had to be pure for three reasons: (a) to improve helium scintillation, (b) to keep the tritium β-decay background low, and (c) to insure that muons were captured on helium and not on impurities. The suppliers specified that the He^3 was pure to within 200 ppm (parts per million), with oxygen and nitrogen as the main contaminants. The tritium content was specified as 1 part in 10^{11}. With all the gas in the target, this amount of tritium results in about 5×10^4 β decays per second. Luckily the β energy is only 18 keV and the β's were not detected by our apparatus.

After using the He^3 in the experiment, we measured its composition on a mass spectrometer. This measurement could not distinguish He^3 and H^3, but showed about 100 ppm of He^4, with no observable traces of any other contaminants. This He^4 probably got in the gas during the switchover from the He^4 target to the He^3. Standard reactor-grade helium was used as the He^4 target and no tests were made of its composition. Both the He^3 and the He^4 were passed through a powdered-carbon purifier maintained at liquid nitrogen temperature for additional purification before use. One can conclude that the gas as a target was pure to 100 ppm.

Light from the gas scintillator was channeled out of the front Lucite window through a hollow aluminized brass elbow into a photomultiplier (RCA 7046). The portion of the elbow in the muon beam was cut away and replaced with a thin window of electroplated silver. An attempt was made to take additional scintillation light out through the edge of the Lucite window; however, tests showed that not enough light came out this way to make the effort worthwhile.

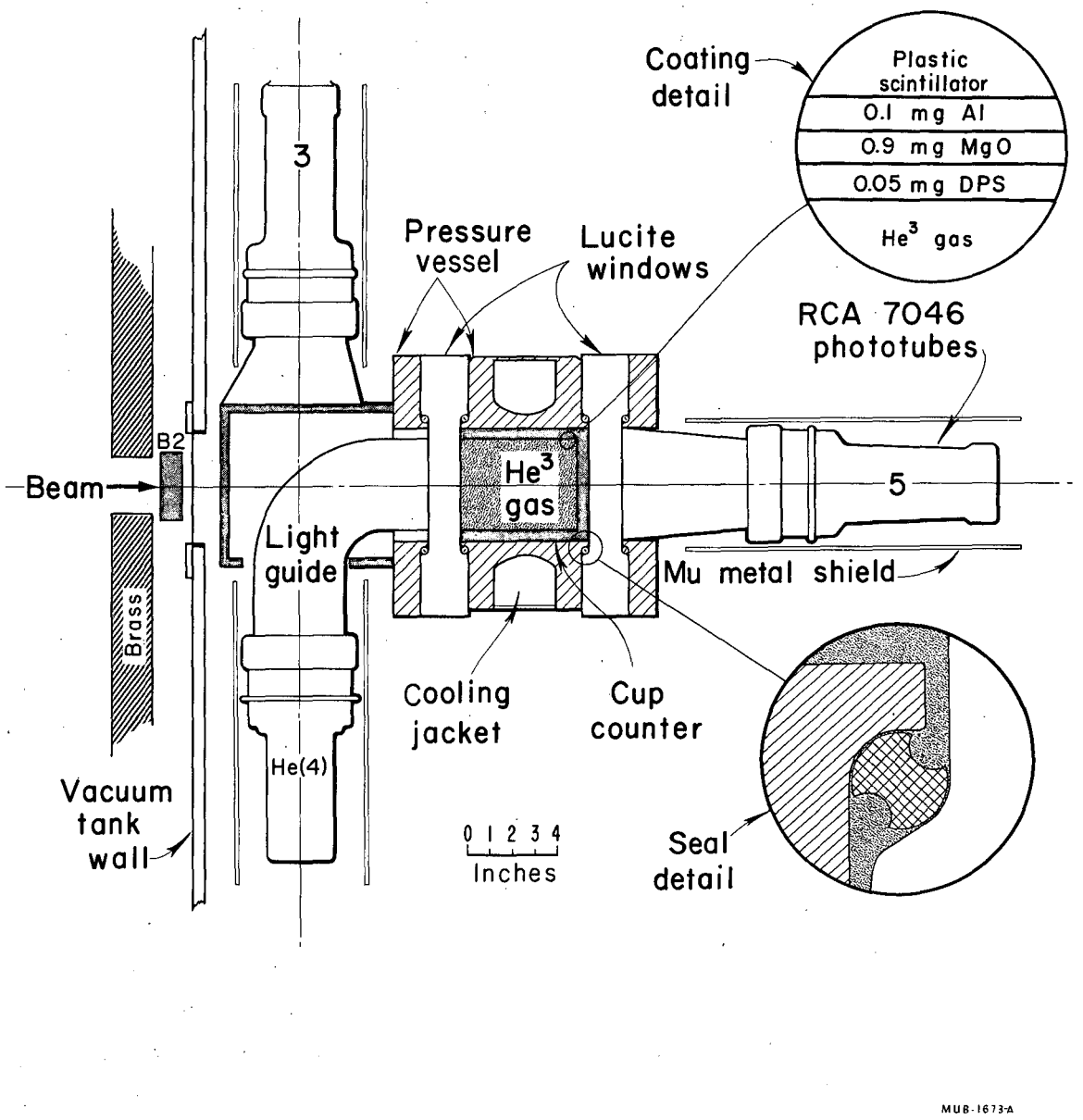

Fig. 4. Top view of the target with details of the pressure seal and the cup-counter coating.

In order to check the uniformity of response inside the gas volume, an Am^{241} α source on the end of a curved steel wire was inserted into the helium gas through a gas-lock system. It was also used for frequent energy calibrations of the gas scintillator.

The gas was surrounded by a cup-shaped plastic scintillation counter (5) 1/2-inch thick. This counter had an inner diameter of 4 inches and an inner length of 5 inches; it vetoed muons that passed through the gas without stopping and detected delayed events (mostly muon-decay electrons) in which the charged particle had enough energy to be counted in 5. The inner wall of the cup was coated with an opaque layer of aluminum (0.3 μ thick), which prevented the scintillation light from the gas and the scintillation light from the cup from mixing. Light from the plastic scintillator passed through the rear Lucite window and into a photomultiplier (RCA 7046).

The plastic scintillation counter 3 served to detect decay electrons that missed counter 5 in coming out the front Lucite window. Counter 3 was 1/4-inch thick and covered as much of the front hole in the cup counter as was possible. The entire apparatus was enclosed in a large vacuum tank of soft iron. Additional target details are given in Appendix B.

C. Helium Scintillation

Since a determination of the capture rate depends on how well we can distinguish the 1.9-MeV triton recoils from background events, an important part of the experiment was to make the helium scintillation process as efficient as possible. Because the mechanism of scintillation is complicated, most information about gas scintillation is empirical. By coating the walls of the gas container with a "wave shifter" backed by a reflecting material, previous investigators obtained the most light output for a given amount of deposited energy.[47] A waveshifter is a phosphor that absorbs the ultraviolet light of the primary scintillation and radiates it in a spectral region more nearly matching the spectral sensitivity of the photocathode. Using the previous investigations as a guide, we performed several tests in an effort to increase the light collected by the phototube.

1. Wall-Coating Tests

Three different wall coatings were tried: (a) sodium salicylate on aluminum, (b) p-p' diphenylstilbene(DPS) on aluminum, and (c) DPS on MgO backed by aluminum. The third coating was finally adopted. Besides requiring a high reflectivity for the wall coating, one must have a very thin coating to reduce the number of muons stopping in the wall material. Results of the coating tests are discussed below.

The sodium salicylate, dissolved in a methyl alcohol solution, was sprayed onto the aluminum surface to an average thickness of ≈ 1 mg/cm^2. Under optimum conditions this coating gave a resolution (FWHM, full width, half maximum) of 27% of the pulse height for the 5.4-MeV Am^{241} alpha source. This variation in pulse height is due to the random nature of photon collection and indicates that the photomultiplier collected only a small number of photoelectrons for each α-particle pulse. There was also a 30% variation in pulse height as the α source moved over the volume of the helium gas. In the actual experiment light comes from triton recoils all over the gas volume, and therefore this variation adds to the resolution coming from photoelectron statistics. In the test with about 100 μg/cm^2 of DPS coated directly on the aluminum surface, the pulse-height varied as the solid angle of the phototube, showing that only light heading toward the phototube reached it. That is, there was very little reflection of light from the DPS and aluminum surface. This agrees with the view that a large fraction of the light generated in the DPS undergoes total internal reflection. In an attempt to get the internally reflected light out, several samples were made with the Al and DPS coatings on a rough (sandblasted) surface. This increased the light output substantially; however there was still much less light from this combination than with the DPS deposited on a white surface, such as paper.

The final configuration tested consisted of a layer of DPS ≈ 50 μg/cm^2 thick backed by a layer of MgO ≈ 1 mg/cm^2 thick deposited over the aluminum coat covering the cup counter. The

front Lucite window had a transparent coating of about 30 $\mu g/cm^2$ of DPS in all the tests as well as in the final experimental arrangement. The DPS and aluminum coatings were in all cases obtained by vacuum evaporation. The MgO was smoked onto the cup counter by burning a magnesium ribbon in air. This white, diffusely reflecting substance has a high reflectivity for both visible and ultraviolet light and, because of its granular surface, it did not allow much light to be internally reflected in the DPS coating. With the MgO and DPS combination, the α source had a 16% resolution under the best conditions, and the pulse height varied only 5% over the volume of the gas. Since it did not appear that we could do much better than this, the MgO and DPS combination was chosen for the experiment.

2. Gas-Purity Effects

Many researchers have found that the purer the gas, the more scintillation-light output.[48] Our results again confirm this fact. At room temperature we found that the pulse height decreases to about half in 2 hours. This presumably is due to contamination of the gas by the waveshifter coating. When the gas container was cooled to dry-ice temperature (195 °K) this effect disappeared, the pulse height remained stable in time, and in fact, a contaminated gas recovered its original properties. Additional cooling (to liquid nitrogen temperatures) did not further increase the pulse height.

By passing reactor-grade helium through powdered charcoal maintained at liquid nitrogen temperature, we doubled the scintillation-pulse height. Passing the helium through a liquid nitrogen trap improved the light output only slightly, thus showing that the absorbing properties of charcoal were essential in the purification. All indications were that a further purification of the gas could lead to an additional increase in the pulse height.

3. Pressure Effects

Early in the scintillation tests we noticed that the pulse height increased with increasing pressure. This effect occurred with both the DPS and sodium salicylate waveshifters and to our knowledge

has not been previously reported.[49] Figure 5 shows the pulse-height variation with pressure of the α source 5.4-MeV peak. The range of the α was entirely within the gas for all points above 2 atm. Gas impurities changed the shape of this curve by causing lower saturation levels. Rubbia and Toller report there is no variation in pulse height for helium pressures between 20 and 100 atm.[50] Figure 5 seems to confirm this. The small decrease in pulse height above 30 atm is probably due to absorption of the scintillation light by the source holder, since at these pressures the range of the α particle is of the same order of magnitude as the source dimensions.

The increase in pulse height up to pressures of 20 atm is probably associated with electron-ion-recombination times in helium. If the helium-scintillation pulses are observed on an oscilloscope, one notices a variation with pressure in the timing of the scintillation light. At low pressures (1 to 2 atm), some pulses associated with the α particle occur as much as 20 μsec after the initial pulse. As one increases the gas pressure, these late pulses occur sooner, and by the time the pressure has reached 20 atm, one can no longer observe any slow component of the light. At all pressures it appears that if one could integrate all the output light over time, there would be no variation with pressure. In our electronics system the pulse-height analyzer measures only helium scintillation light that occurs in the first 100 nsec after the start of scintillation. Thus the variation of the pulse height with pressure is due to a variation in the timing of the output light.

Qualitatively one would expect that, as the gas pressure increases, the electron and ion densities associated with the ionization of an α particle would also increase proportionally to the pressure (the α range is inversely proportional to the pressure). This would make it easier at the higher pressures for the electrons and ions to recombine and to produce the scintillation light. This suggestion relating the timing of the helium scintillation to electron-ion recombination is supported by the following quantitative calculation.

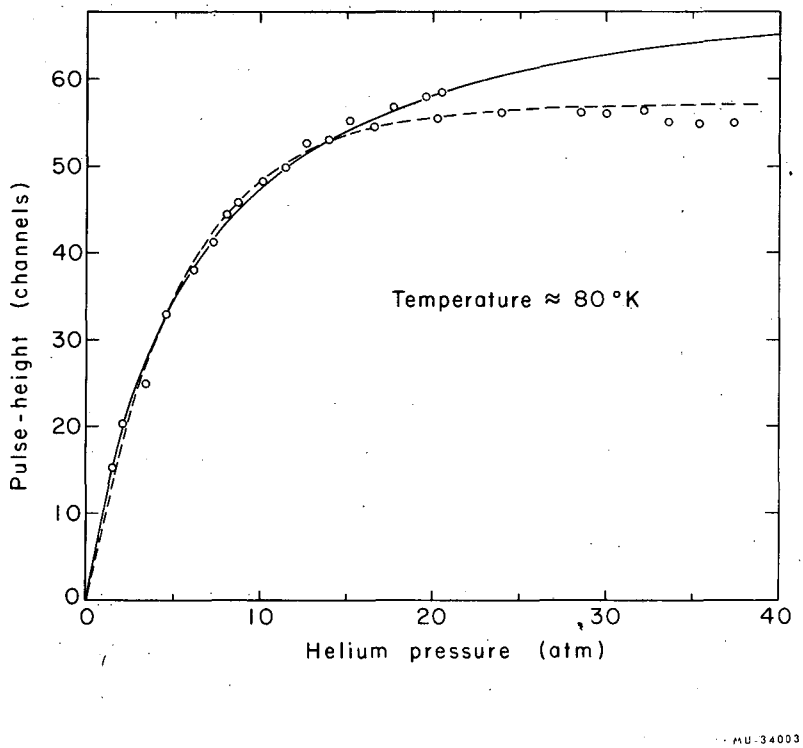

Fig. 5. Variation of a 5.4-MeV α-scintillation pulse height vs helium gas pressure. Both He^3 and He^4 followed the same curve, whose shape is independent of the wave shifter used. The solid curve is a least-squares fit of the data points below 20 atm to a function of the form $kP/(1+KP)$, with $K = 0.17$; the dashed curve is the function $1 - \exp(-KP)$, with $K = 0.19$. P is the gas pressure.

If n_- and n_+ are the electron and ion densities, then the rate of recombination is[51]

$$\frac{\partial n_+}{\partial t} = \frac{\partial n_-}{\partial t} = -\zeta n_+ n_- , \tag{47}$$

where ζ is the recombination constant and equals 1.7×10^{-8} cc/ion-sec in helium at $\approx 1/30$ atm.[52] The recombination constant should be independent of pressure but no measurements of ζ have been made in our pressure range. The first differential equation gives

$$n \equiv n_+ = n_- + c, \tag{48}$$

where $c = 0$ if the gas is electrically neutral. Substituting n in Eq. (47) and solving the differential equation

$$\frac{\partial n}{\partial t} = -\zeta n^2 \tag{49}$$

for n, one obtains

$$\frac{1}{n} = \frac{1}{n_o} + \zeta t \qquad \text{or} \qquad n = \frac{n_o}{1 + n_o \zeta t} \tag{50}$$

where n_o is the initial-ion density. The density of recombinations occurring between $t = 0$ and t_1 is just the difference between the initial-ion density n_o and the density at time t_1, i.e.,

$$n_o - n = n_o - \frac{n_o}{1 + n_o \zeta t_1} = \frac{n_o \zeta t_1}{1 + n_o \zeta t_1} . \tag{51}$$

The light output is proportional to the number of recombinations N occurring between $t = 0$ and $t_1 \approx 100$ nsec, and one must multiply Eq. (51) by the volume of the ionization V to get a number rather than a density. Thus one can write

$$N = (n_o V) \left(\frac{KP}{1 + KP} \right) \tag{52}$$

where $K = n_o \zeta t_1 / P$ is approximately independent of the pressure P. Since V is roughly inversely proportional to P and n_o is proportional to P, the product $n_o V$ should be independent of the pressure. Thus

the light output can be written

$$L = \frac{kP}{1 + KP} \tag{53}$$

where k is a proportionality constant independent of the pressure. The solid line in Fig. 5 is a curve of this shape with K = 0.17/atm and it fits the data points below 20 atm reasonably well. Above 20 atm the discrepancy between the data and Eq. (53) could be real but more likely is due to a nonadiabatic change in the gas pressure near 20 atm. Pumping the gas into the target (see Appendix B) required a rapid and uncontrolled increase in the pressure from 20 atm to the maximum pressure near 37 atm. All points in this region were obtained while decreasing the gas pressure. The rapid increase in pressure during pumping could have caused a decrease in the pulse height and could explain the deviation of the data points from the solid curve.

In any event, one can use the value of K to calculate n_o to see if it checks with the expected alpha-ionization density. At a pressure of 7 atm, the alpha range is 1 cm and

$$n_o = \frac{KP}{\zeta t_1} = 7 \times 10^{14} \text{ ions/cm}^3. \tag{54}$$

If one uses the ratio of 30 eV per ion pair produced by the α, one obtains for the expected α-ionization density

$$n_+ = n_o = \frac{1}{V} \frac{5.4 \text{ MeV}}{30 \text{ eV}} ; \tag{55}$$

V will be a cylinder of length 1 cm and radius R. The value of R is not easy to calculate but it is probably close to a mean-free path in the gas, which is 1000 Å at 7-atm pressure. Using this value for R, one obtains $n_+ \approx 10^{15}$ atoms/cm^3, which checks well with Eq. (54). Because the approximations are very rough and because the value of ζ, the recombination coefficient, was extrapolated from 1/30 atm to $\approx$ 30 atm, one must consider the above calculation to be good only to a factor of $\approx$ 100. However, the excellent agreement between the two values of the ion density supports a recombination-time explanation for the pulse-height variation of Fig. 5.

4. Scintillator Performance

Figure 6 shows the performance of the helium-gas scintillator in measuring three energies under experimental conditions. The light output was found to be linear with energy loss (see Fig. 7) and to vary only 5% over the volume of the counter. The final energy resolution of 38% for the 1.9-MeV triton recoil corresponds to an average of 30 effective photoelectrons.

D. Muon Beam

A diagram of the beam configuration is shown in Fig. 8. Mesons are produced by inserting a beryllium target 2-in. thick into the 720-MeV internal proton beam of the Lawrence Radiation Laboratory's 184-inch synchrocyclotron. Muons come mainly from pions that decay close to the target. The particles are deflected out of the cyclotron by its own magnetic field, and pass through a thin aluminum window of the vacuum tank into the 8-in. aperture of a two-section (doublet) quadrupole magnet (Q1). This quadrupole brings the beam to a focus just outside an 8-foot long iron collimator known as the meson wheel. A previous study showed that the highest intensity of negative particles could be obtained at a meson-wheel angle of 18° and a beam momentum of about 200 MeV/c.[53] Consequently these parameters were chosen, and they in turn determine the approximate radial and azimuthal position of the beryllium target.

The thickness of the material traversed just before entering the helium target was about 9 gm/cm^2, requiring a momentum incident on the target of at least 100 MeV/c. Since the helium gas was at most 240 mg/cm^2 thick, one important beam requirement was a small-incident-momentum spread. This requirement led to the large, 70°-bending angle of the beam and to the placement of a degrader at the first focus just after the meson wheel and before the bending magnet. Polyethylene (CH_2) was chosen as the degrader in order to minimize multiple scattering. Finally a second 12-in. aperture quadrupole (Q2) brought the beam to a second focus at the target. Two time-of-flight counters (B1 and B2) with their associated electronics analyzed

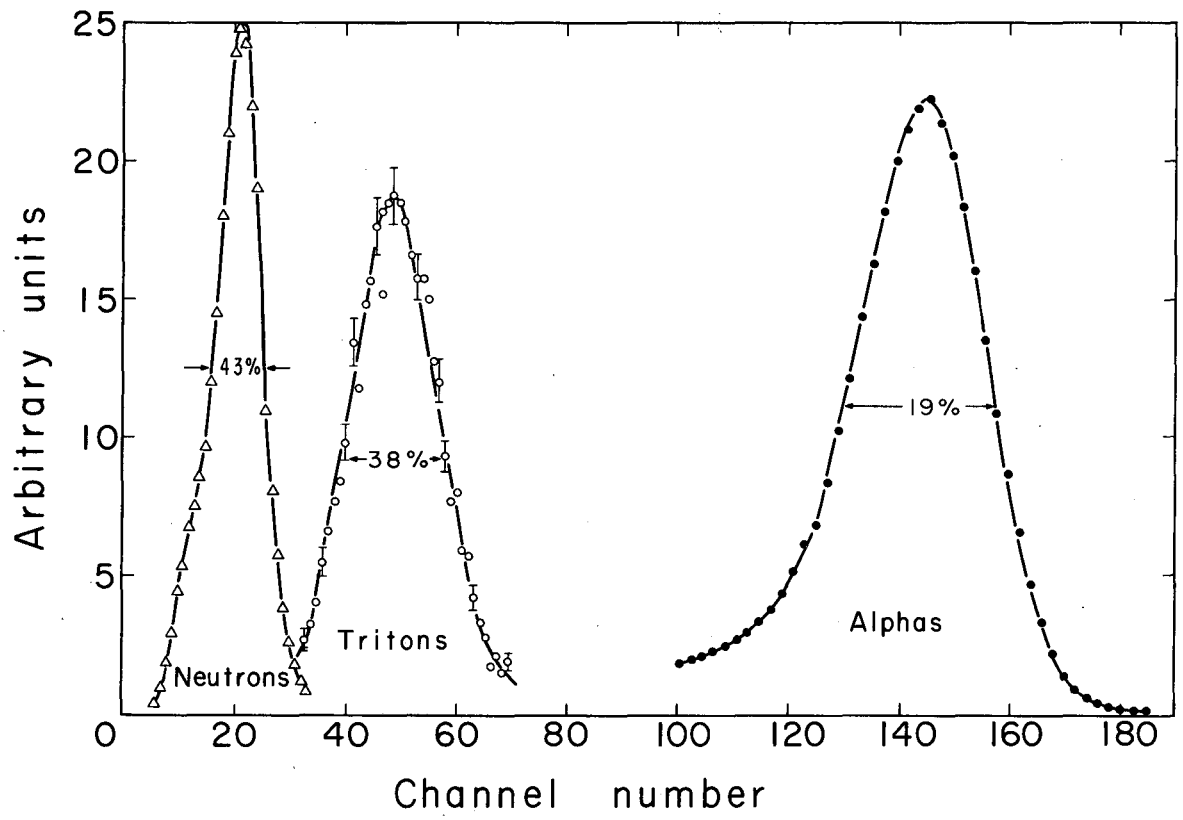

Fig. 6. Calibration energy peaks showing the resolution of the helium scintillator. The neutron peak was obtained from the capture of thermal neutrons in He^3 (i.e., $n + He^3 \rightarrow H^3 + p$), in which 0.77 MeV is released; the triton peak is from the final data on muon capture in He^3 (i.e., 1.9-MeV triton recoils); and the alpha peak is from an Am^{241} alpha source (5.4 MeV).

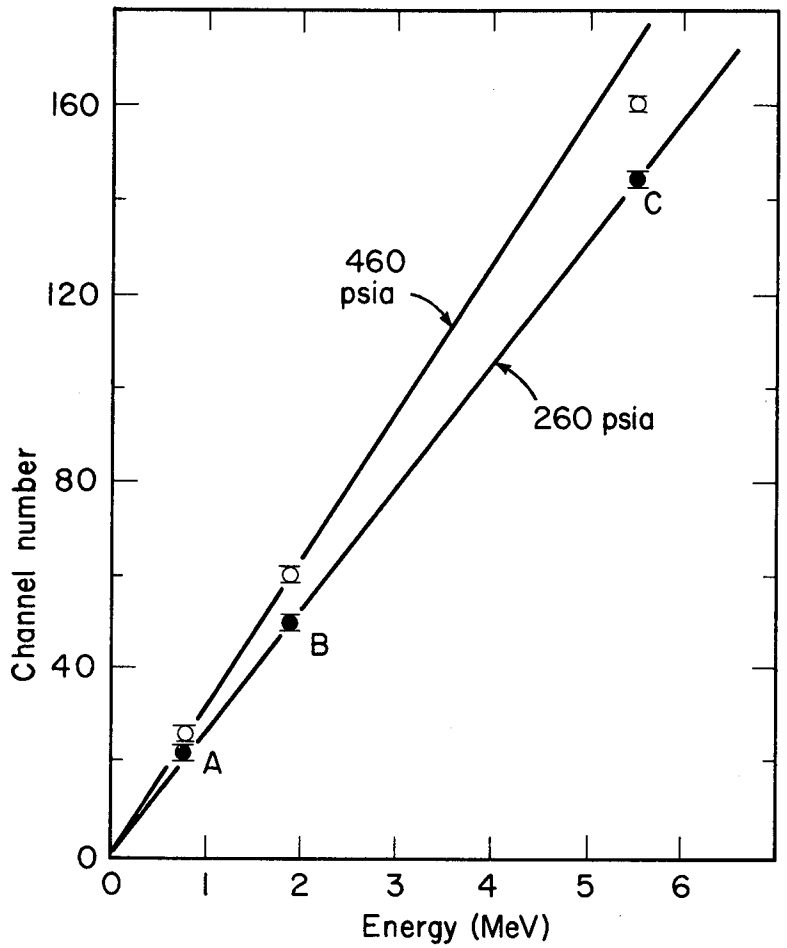

Fig. 7. Energy calibration of the pulse-height analyzer at two gas pressures: A, neutron captures; B, triton recoils; C, Am^{241} alpha particles.

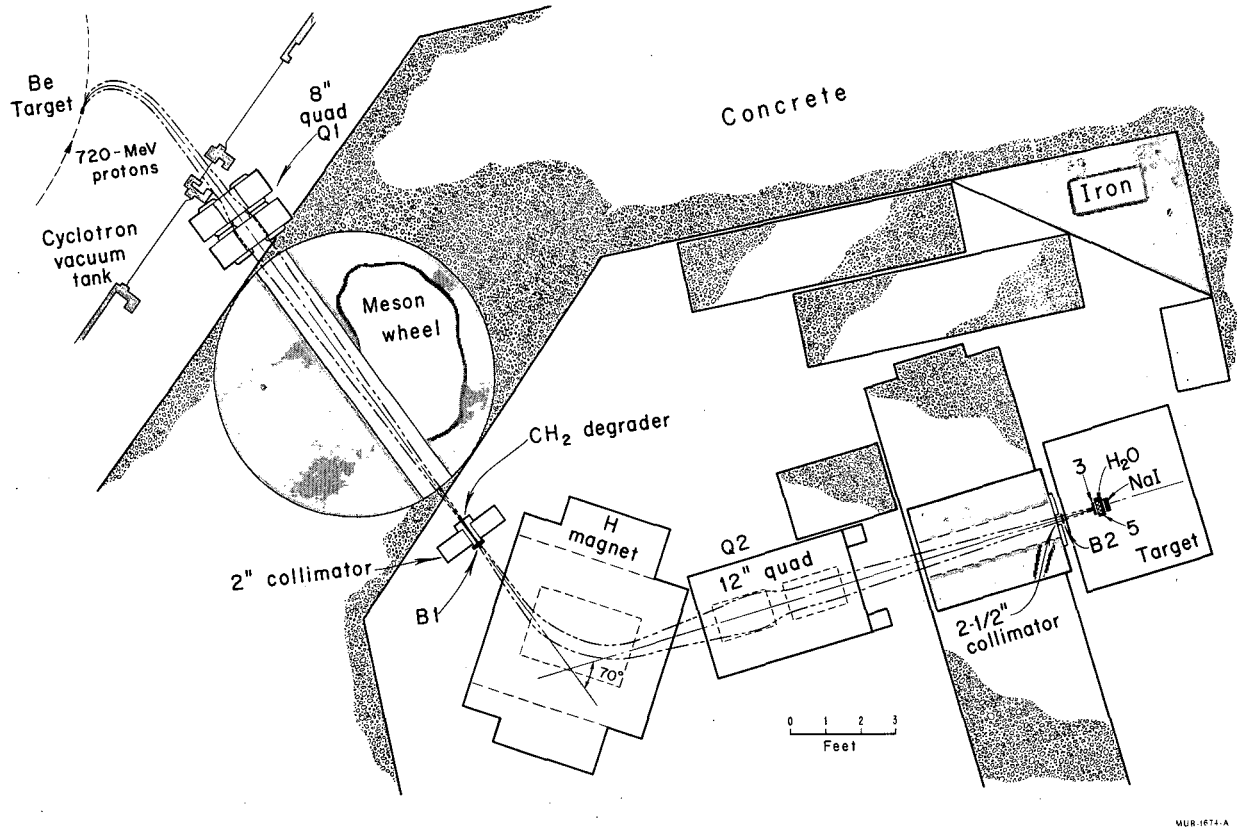

Fig. 8. Scale drawing of the beam-transport system.

the beam into pions, muons, and electrons (see Sec. III. F. 2). Helium bags were used in the beam channel wherever practical in order to reduce multiple Coulomb scattering of the beam in air.

We experimentally optimized the muon beam by making a series of variations in the magnet currents, the thickness of the absorber at the first focus, and the radial and azimuthal position of the Be target. The quadrupole currents initially selected in this investigation were calculated with the computer program OPTIK,[54] which is a very general program that will trace beam rays through various elements of the beam-transport system, including bending magnets, quadrupoles, and collimators. The value of the bending-magnet current for a given momentum was determined by means of the wire-orbit technique[55] with the magnet in place and with the cyclotron field on. Wire orbiting was also used to check the calculated quadrupole currents. Given an arbitrary magnetic-field pattern and the initial position and momentum of a particle, the program[56] ORBITS will trace the orbit of the particle. It was useful in tracing beam rays from the Be target through the magnetic field of the cyclotron to Q1, and determined that the effective object position of the Be target in the horizontal plane was 123 inches from the center of Q1. Knowing this and the desired position of the foci, OPTIK calculated the quadrupole field gradients and demonstrated the effect of various collimator sizes. The first element of Q2 focused the rays in the horizontal plane and thus gave almost unit magnification in the horizontal plane while reducing the object to about one-half size in the vertical plane. Consequently the collimator at the first focus (the object of Q2) was made twice as high as it was wide. This collimator was 6 inches long, made of copper, and had an aperture 4 inches high and 2 inches wide containing the CH_2 degrader. The second collimator, placed just before the helium target, consisted of a brass plate 2-in. thick containing a hole 2.5 in. in diameter.

Two criteria were used in experimentally optimizing the beam: (a) muon intensity, and (b) the ratio of μ to $\pi + e$. Because the

pion and electron sources are essentially the size of the target, whereas the muon, being produced in pion decay, has a more diffuse source, a slight detuning of the beam optics greatly increases the muon ratio in the beam. From a ratio of 0.07 one can pass by detuning to a ratio of 2. In addition, by replacing some of the CH_2 degrader at the first focus by a quarter inch of lead (which causes the electrons to lose additional energy by bremsstrahlung), one can obtain over 90% muons in the beam. However, no lead radiator was used in this experiment since it also reduced the muon intensity somewhat; furthermore beam electrons did not appreciably hurt the experiment since these electrons are all vetoed by counter 5.

The beam study showed that the best compromise between muon intensity and μ to $\pi + e$ ratio is obtained with 9.6 inches of polyethylene (plus the 1-inch-thick counter B1) at the first focus, a target radius of 81 inches, and an azimuth of 252° from the north. This study was carried out at a fixed-bending-magnet current of 175.5 A, corresponding to central-ray momentum of 109 MeV/c. The optimum currents for Q1 were determined to be 32.6 A in the first (horizontally divergent) element and 38.1 A in the second (corresponding to field gradients of 90 G/in. and 104 G/in. respectively). Switching on Q1 increases the beam intensity by a factor of two. About 110 A (corresponding to 250 G/in.) in each element were the optimum currents for Q2. Under these conditions we obtained in the useful stretched part of the beam an average maximum of 650 muons per sec (57% of the beam particles were muons).

Figure 9 shows the momentum spread of the beam through the second collimator to be 4.4%. The momentum spread of the beam before the degrader at the first collimator was 6%, whereas after the degrader $\Delta p/p = 26\%$. A range curve determined that the addition of half an inch of polyethylene just after counter B2 led to the maximum number of muons stopping in the gas for a fixed incident momentum of 109 MeV/c. Pions of this momentum stop just before the front Lucite window of the target, whereas electrons have

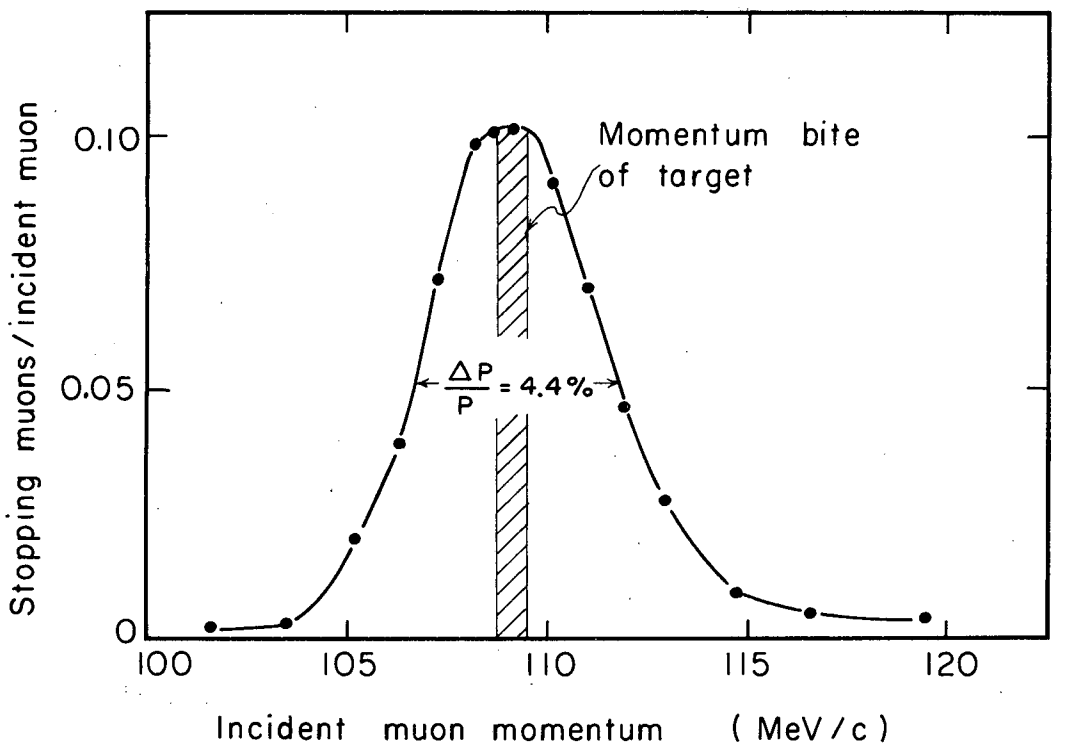

Fig. 9. Variation of the ratio Sμ/Bμ with the bending-magnet current. Shaded area shows the calculated momentum bite of the relatively thin helium target. (Sμ = muon stopping in the helium; Bμ = incident-beam muon).

about five times the range of the muons. Thus in addition to the time-of-flight requirement, muons are also selected from the beam by the range requirement. An average of ≈ 50 muons/sec stopped in the helium gas (at 28.9 atm), which leads to an events rate of ≈ 10 triton recoils per minute. Positive muons were obtained by the reversal of all the magnetic fields and the use of the particles emitted in a backward direction from the cyclotron target. Typical μ^+ intensities were ≈ one-quarter of the negative-muon intensities.

At all times throughout the experiment, the auxiliary dee of the cyclotron was used to improve the beam duty cycle. In this mode almost half of the beam intensity comes in a "beam spike" about 300 μsec wide at the end of each accelerating cycle (64 cps), but the remaining beam intensity is "stretched" almost uniformly in time over the next 10 msec. The spike in beam is not useful since the extremely high counting rate at this time jams the counters; therefore the scalers and pulse-height analyzers were electronically gated off during this part of the beam cycle. Pulses from the dynode of counter B1 were integrated and displayed on an oscilloscope as a beam monitor. Figure 17(a) shows a typical beam display with the gating signal superimposed. The duty factor is typically 55% of the total time and, of course, excludes the time when the scalers are gated off during the spike. The beam also has an rf structure (18 Mc) that is ignored in measuring the duty factor.

E. Distribution of Stopping Muons

Knowledge of the spatial distribution of muons stopping in the target is needed to properly calculate the following quantities:

a. The fraction of the muon beam stopped in the target,

b. The fraction of the muon beam stopped in the dead layer of the cup counter (see Sec. IV. A),

c. The fraction of muons stopping in the gas but close enough to the wall so that the triton recoil collides with the wall (see Sec. IV. K),

d. The fraction of muon-decay electrons that escape counters 3 and 5 (see Sec. III. F. 6),

e. The energy distribution of the charged particle in the breakup reactions, Eqs. (4) and (5) (see Sec. IV. F).

The stopping-muon distribution is mainly determined by the size of the collimator just before the target and by the occurrence of multiple scattering as the muon slows down in the material before the gas. The stopping distribution was both calculated and experimentally measured. The experimental verification of the multiple-scattering calculation justified the use of the calculated distribution for the above purposes.

1. Multiple-Scattering Calculation

Figure 4 shows the material that the muon passes through before it is stopped in the gas. This material was split up into slices, such that the product of the muon momentum and the velocity ($p\beta c$) is fairly constant in any one slice. Next, the mean-square scattering angle[57]

$$\theta_i = \frac{21.2 \text{ MeV}}{p\beta c} \sqrt{\frac{X_i}{X_o}} \tag{56}$$

was computed for each slice. (X_o is the radiation length of the material and X_i the thickness of the slice.) Assuming that each of these angles is small, the net rms scattering angle is found by adding the square of each partial θ_i

$$\theta_{net}^2 = \sum_i \theta_i^2 . \tag{57}$$

If d_i is the distance of each slice from the point where the muon stops, then the rms displacement from the mean position at the stopping point is given by

$$r_o^2 = \sum_i (d_i \theta_i)^2 . \tag{58}$$

As a result of the multiple scattering, the beam has a probability per unit area

$$P(s, r_o) = \frac{1}{\pi r_o^2} \exp(-s^2/r_o^2) \tag{59}$$

to be found at a distance s from its position without scattering (point B in Fig. 10). This probability distribution is that of a two-dimensional random-walk problem. Following an article by Sternheimer,[58] this probability must then be integrated over the area of the beam. If we assume that the beam distribution is uniform over the area of the collimator, and since we have cylindrical symmetry, the probability per unit area per input beam particle of finding a beam particle at a distance r from the axis of symmetry is

$$Q(r, r_o) = \int_0^{2\pi}\int_0^{R} P(s, r_o)\rho\, d\rho\, d\theta \,. \tag{60}$$

See Fig. 10 for the notation used. Using the law of cosines and performing the integration over θ, we have

$$Q(r, r_o) = \frac{1}{\pi r_o^2}\int_0^{R}\int_0^{2\pi} \exp\left[-\left(\frac{r^2+\rho^2-2r\rho\cos\theta}{r_o^2}\right)\right]\rho\, d\rho\, d\theta$$

$$= \frac{2}{r_o^2}\exp(-r^2/r_o^2)\int_0^{R} I_o(2r\rho/r_o^2)\exp\left[-\left(\frac{\rho^2}{r_o^2}\right)\right]\rho d\rho \,, \tag{61}$$

where I_o is the Bessel function with imaginary arguments. The computer program MUSCAT[59] was developed to integrate the above formula numerically for different radial positions and different r_o (corresponding to the z coordinate).

The calculation outlined above gave a rms scattering angle of $\theta_{net} = 22^\circ$ and a rms displacement varying almost linearly from $r_o = 1.2$ inches at the front of the cup counter to 2.05 inches at the back. The largest contribution to the multiple scattering (about 80%) comes from counters B2 and 3 and from the absorber just behind B2. Reduction of the thickness of this material and its distance from the target could almost halve the number of particles stopping near the wall. The dotted lines of Fig. 11 show the variation of

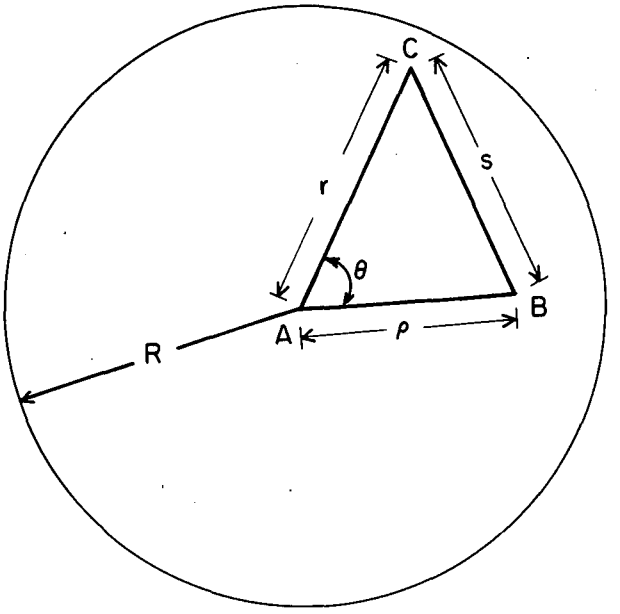

MU-34004

Fig. 10. Notation used in multiple-scattering calculation. A is axis of symmetry of collimator of radius R, B is the place where a beam particle would have hit if there were no multiple scattering, and C is the place where a beam particle might actually hit.

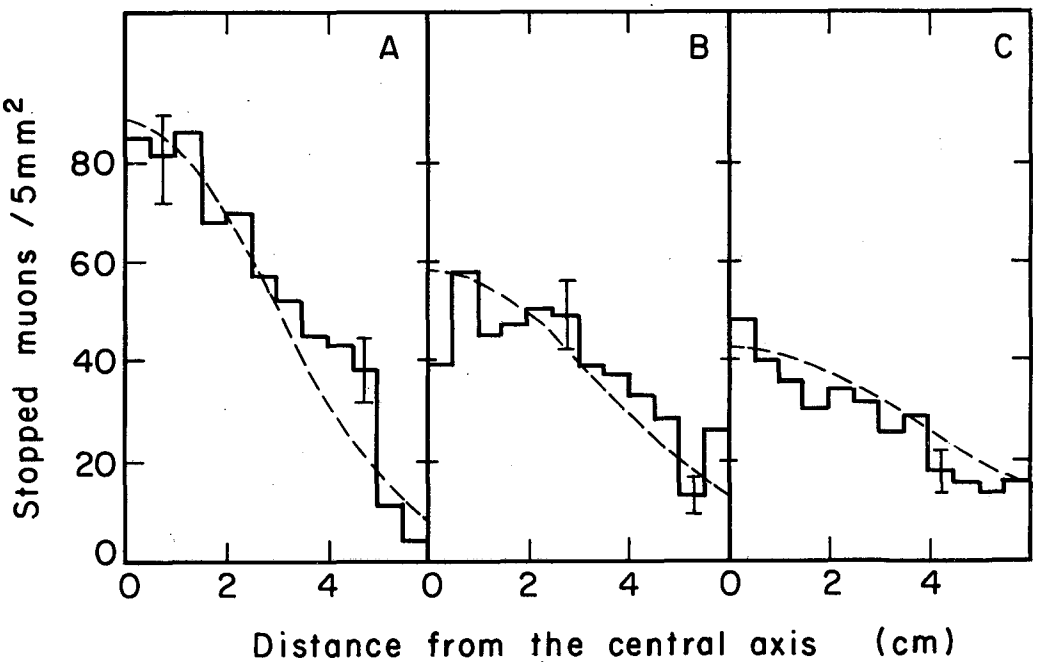

MU-33863

Fig. 11. The histograms show the radial variation of muons stopping in a nuclear emulsion. Emulsion A was exposed directly behind the front Lucite window in the target, emulsion B 2-3/4 inches behind the front window, and emulsion C 5 inches behind the window. Each emulsion was exposed to 2×10^6 beam muons. The dashed lines are the muon-stopping distributions, at the same three positions, obtained from the multiple-scattering calculation and are normalized to the same total area as the histograms. Note that fewer muons stop near the rear of the cup counter than stop near the front.

$Q(r, r_o)$, the probability per unit area of muon stops, with radial positions at three different places in the cup counter. Because of the spreading of the beam, about 50% more muons stop in the front of the gas than in the back.

2. Emulsion Exposure

The above calculation is approximate, for not only does it neglect plural and single scattering at large angles, but it also neglects the angular divergence of the beam. These and other similar effects should be small but they make the calculation uncertain. Thus, in order to verify the multiple-scattering calculation, three K-5 nuclear emulsions were exposed inside the target after removal of the rear Lucite window and the cup counter. Only a limited area of these emulsions was scanned for stopping muons because of the time involved. Within the limited scanning statistics, however, it appeared that the beam was cylindrically symmetric and that the stopping distribution checked well with the multiple-scattering calculation (see Fig. 11). As the scanning efficiency may have been as low as 70%, no absolute computation was made of the expected muon stops in the emulsion. The computed curves in Fig. 11 were normalized to the areas of the emulsion histograms in A, B, and C. That is, one normalizing factor was used for all three curves; this allows a comparison between A, B, and C.

F. Electronics

Figure 12 is a block diagram of the electronic circuit used in the experiment. I first give some general details of the electronics and then go on to describe each element of the figure.

1. General Details

All the circuits used in the experiment were transistorized except those of Hewlett-Packard amplifiers, the high-voltage power supplies, and the scaler-gating control. This led to a very reliable system with no electronic failures due to fatigue during the experiment. The entire logic was built up from modules and was contained in the double rack shown in Fig. 13. The voltage divider used in the

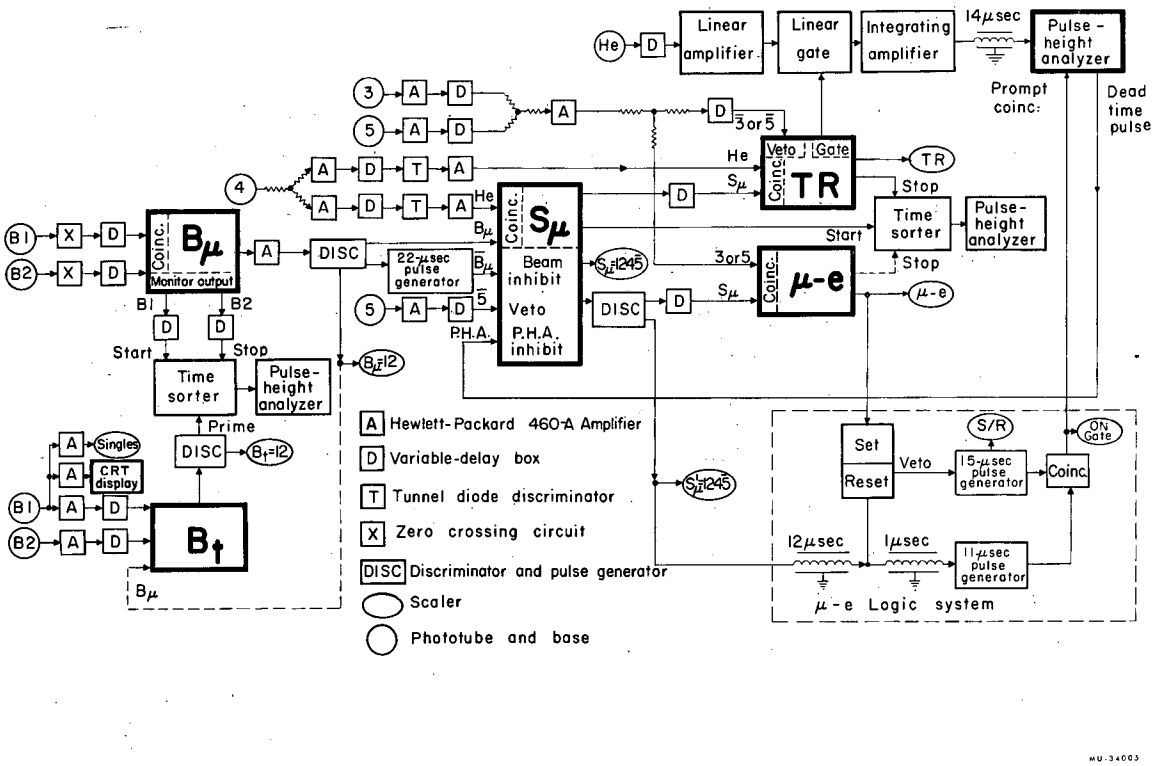

Fig. 12. Block diagram of the electronics circuitry.

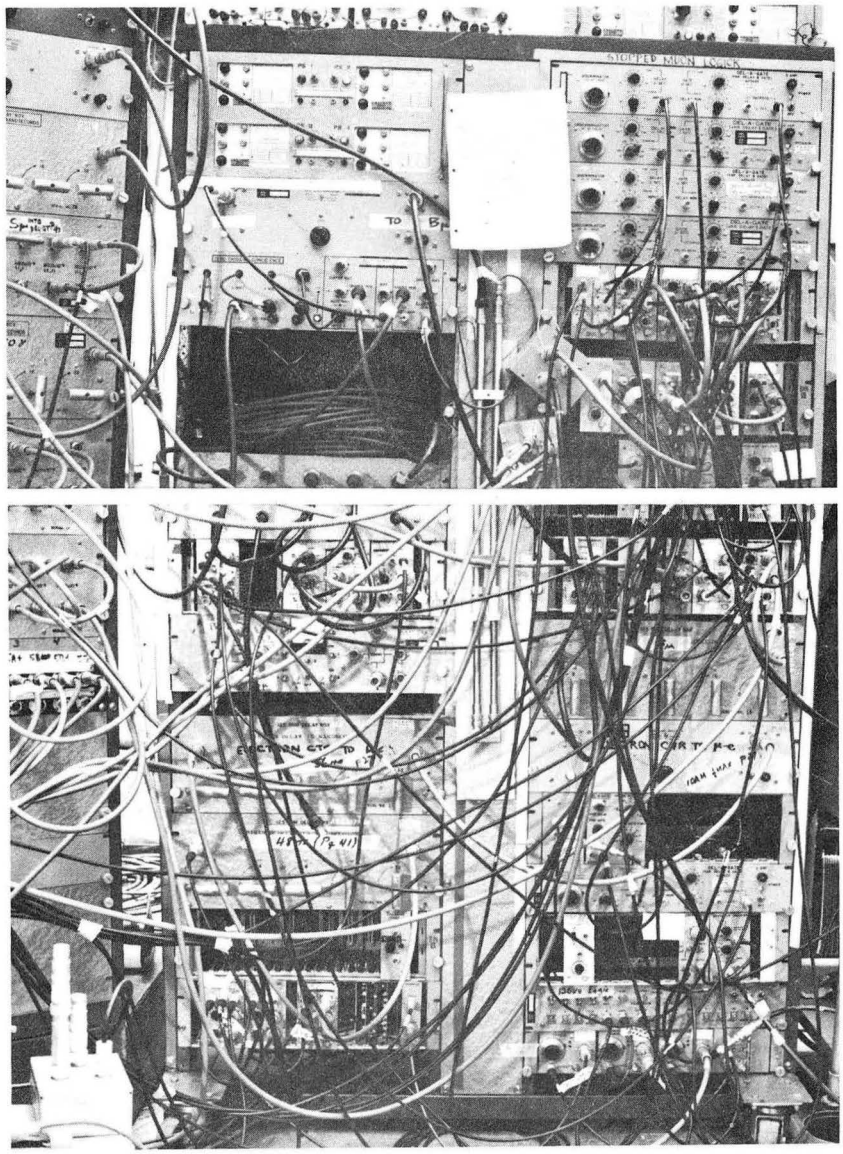

ZN-4281

Fig. 13. Rack containing the electronic logic circuits.

base of all the 7046 phototubes (counters 3, 4, and 5) is a standard ×4 divider, as described, for instance, in the UCRL Counting Handbook.[60] The high voltage for the phototubes was monitored with a digital voltmeter (Hewlett-Packard model 521 DR) and was kept constant to within ±1 volt throughout the experiment. Most of the cable was of the type RG-63/U with a 125-ohm impedance. Some of the cable used in the logic was 125-ohm BNC type, but low-loss 50-ohm Styrofoam coaxial cable was used between counters B1 and B2 and the circuit Bμ. Standard Lawrence Radiation Laboratory pulse inverting and impedance-matching transformers were used as required throughout the circuit. A distributed amplifier (Hewlett-Packard type 460A) was used as a general-purpose amplifier, and the delay boxes consisted of RG-63/U cable with easily interchangeable lengths. All scalers were Model V of Radiation Laboratory design[60] and were gated by a master control. The pulse-height analyzer was the Radiation Instrument Development Laboratory's model 34-12 (RIDL), which has 400 channels.

2. Identification of the Muon Component of the Beam

Counters B1 and B2 are plastic scintillators 1-inch thick observed via Lucite light pipes by 10-stage photomultiplier tubes (RCA 6342A). Since B1 had an average of 10^6 particles/sec passing through it (with instantaneous rates much higher), Zener diodes were used in the base of the tube for stabilizing the voltage supplied to the last few dynodes. In addition it was necessary to increase the current through these diodes and to put B1 on its own power supply in order to keep the high voltage constant at the high-beam rates. Both phototubes were surrounded by magnetic shielding to reduce effects of the cyclotron-fringing field.

The bases of B1 and B2 contain special zero-crossing circuits[61] that produce a pulse at a time independent of the original pulse height. The very small (millivolts) signals from these bases are brought to the coincidence circuit[62] Bμ in the counting area via low-loss 50-ohm Styrofoam cable. The fine adjustments in the timing between B1 and

B2 pulses are made with a continuously adjustable "trombone" delay. The input signals are monitored after the first stage of amplification in the coincidence unit independent of whether or not a coincidence is made. These monitor signals are used to start and stop a fast transistorized time-to-pulse-height converter[63] whose output goes to an RIDL pulse-height analyzer. This time sorter allows us to measure accurately the number of pions, muons, and electrons in the beam and is extremely useful in optimizing the ratio of muons to other particles in the beam. Figure 14(a) shows a typical beam spectrum. Although the resolution (FWHM) of the coincidence can be made better than 0.2 nsec, the peaks of Fig. 14(a) are 1.2 nsec wide because of the different path lengths that a particle can have on going from B1 to B2.

The dynode signals from B1 and B2 are amplified, delayed relative to each other, and fed into the coincidence unit, B_t.[64] In this circuit any pulses coming within 20 nsec of each other are accepted and thus all beam particles will produce a pulse. The output of B_t is passed through a discriminator, which generates both a scaling pulse and a pulse that primes the time converter. This priming coincidence is necessary since otherwise the high counting rate of B1 changes the bias levels in the time converter and causes time jitter.

By use of a signal from B_μ to fire B_t, the time sorter can be gated on only for muons that produce a B_μ output. The resulting spectrum allows a convenient way to set the delays of B1 and B2 into B_μ and reassures us that circuit B_μ is working and triggering only on muons. Figure 14(b) shows the beam spectrum with the time sorter gated in this manner. Comparison with Fig. 14(a) indicates that B_μ is accepting virtually all muons and very few pions or electrons. Please note that in addition to the time-of-flight selection of muons, range requirements allowed only muons to stop in the helium gas. Thus there is double assurance that the stopping-beam particle is a muon.

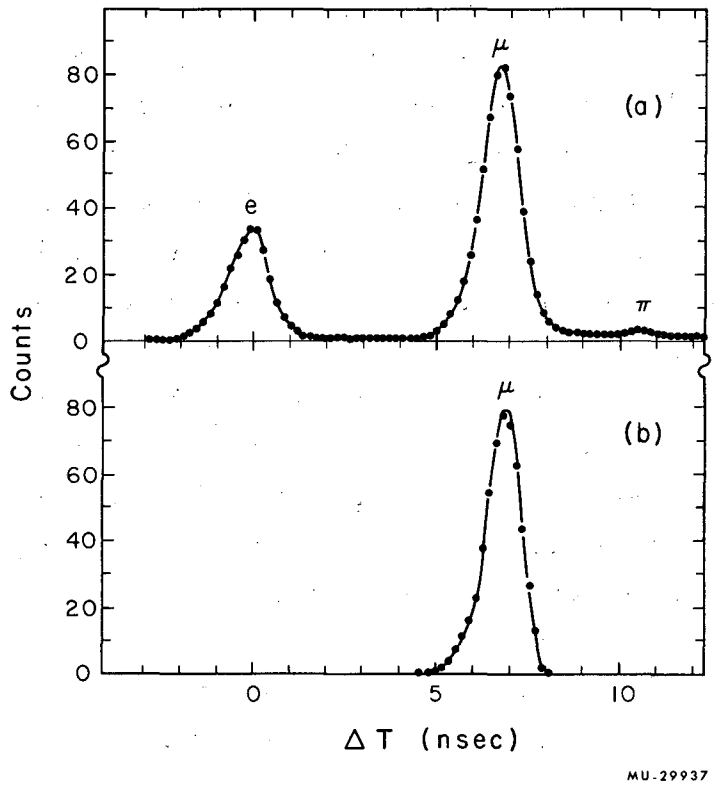

Fig. 14. (a). Composition of the beam, as measured by time-of-flight analysis with counters over a flight path of 18.5 feet: 60% muons, 38% electrons, and 2% pions.

(b). Same spectrum when the time sorter is gated only on the fast coincidence, Bμ.

3. Stopped-Muon Circuitry

The pulse from Bμ is amplified, scaled, and fed into the coincidence circuit Sμ (Ref. 65, Fig. 15). The dynode pulse from the He counter (4) is split, amplified, delayed, and fed from a tunnel-diode discriminator into Sμ. Thus a He-Bμ coincidence ensures that a muon reached the helium gas. To ensure that the muon did not go beyond the helium gas, the cup counter's anode signal (5) was used as a veto in Sμ. Checks throughout the experiment ensured that 5's vetoing efficiency remained the same. This was required in order to keep constant the number of muons that just penetrate 5 without leaving enough light in the scintillator to veto themselves. The basic scaler Sμ counts need a correction for these muons and for those stopping in the MgO and Al coating on the cup counter (see Sec. IV. A).

There are two other anticoincidence requirements for the circuit Sμ. One "inhibit" circuit, triggered by Bμ, turns the circuit Sμ off for 22 μsec after every beam muon enters the system. This keeps the rest of the electronics from being "confused" when there is a pileup of muons. This inhibit circuit vetoed about 2.5% of all the Sμ.

It takes the PHA an average of about 80 μsec to analyze a given pulse and during this time the PHA cannot accept a second pulse. Therefore, to prevent the possibility that a good event might not be analyzed because the analyzer is already busy, the PHA also inhibits Sμ during the time it is analyzing a pulse. To first order these two inhibits do not affect the TR/Sμ ratio since they inhibit equally muons that are going to be captured or those that will decay. If a second muon did come along and was captured by a He^3 nucleus while the first muon was still being analyzed, it would appear as if the TR event came from the first muon. This second-order effect changes TR by less than 0.05% and hence we neglect it.

Some good stopped muons will decay almost immediately. Their decay electron then has a good chance of causing a pulse in $\bar{5}$

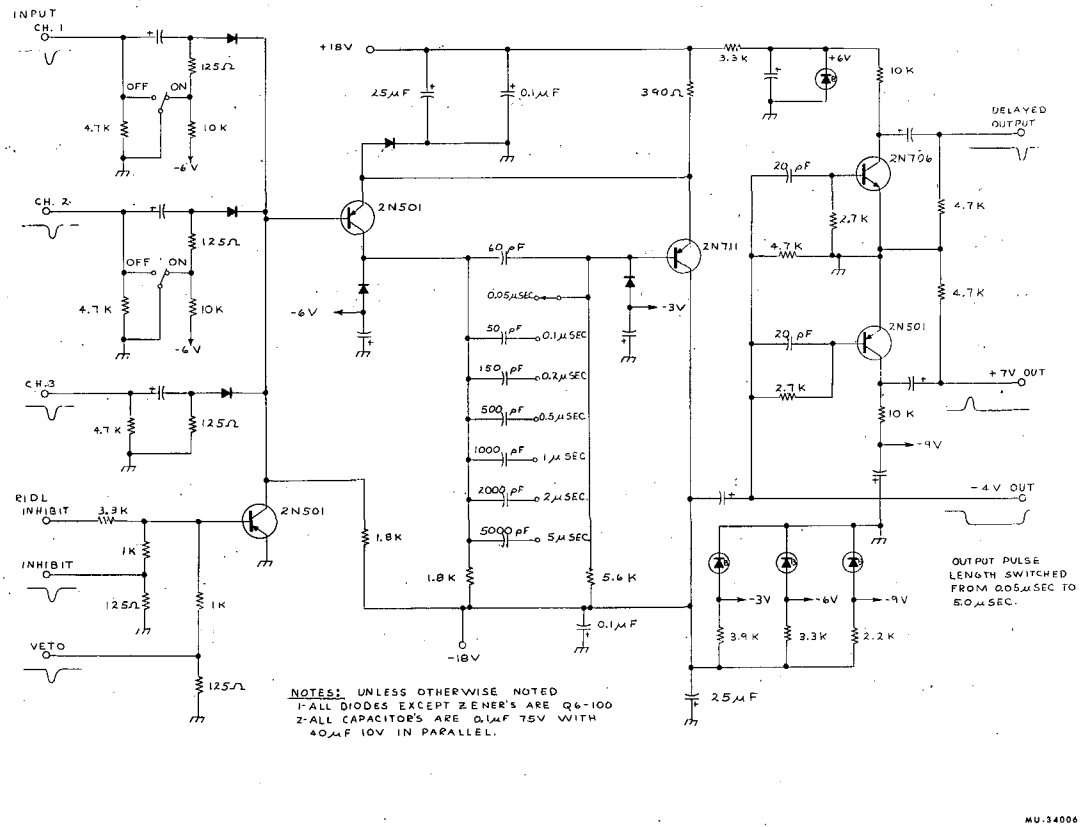

Fig. 15. Three-fold coincidence circuit with output triggers, as designed by G. Culligan and N. H. Lipman. Sμ, TR, and μ-e coincidences use this circuit.

to veto the coincidence Sμ. This would tend to increase the TR/Sμ ratio since this effect preferentially vetoes those muons that decay into electrons. The number of electrons that veto their own muon can be found from a measurement of the overlap of the anticoincidence $\bar{5}$ pulse with the coincidence He Bμ that signals the arrival of a muon. The overlap can be determined from the delay curve of 5 into Sμ [shown in Fig. 16(a)]. Pulses occurring in $\bar{5}$ later than 14 ± 2 nsec after timing for a normal prompt $\bar{5}$ pulse will not veto Sμ. Thus, knowing that the muon lifetime is 2.2 μsec and that $\bar{5}$'s electron efficiency is about 86%, one can easily calculate that 0.55 ± 0.11% of all stopped muons are vetoed by their own decay electrons.

Early in the experiment it was discovered that, in addition to the light coming from the helium gas, light was also coming from the front Lucite window. This light could generate a false Sμ signal since a muon stopping in the front window would have all the electronic appearances of a muon stopping in the gas. The amount of light from the window was small compared to the helium scintillation light, and we therefore used the tunnel-diode discriminator on the He-to-Sμ line to bias against this light output. Muons passing through the window still gave out light but those stopping in the window did not trigger a pulse big enough to fire the He-Sμ discriminator. By taking all the gas out of the target, one could easily check that there were no Sμ counts from the window. Under our operating conditions, there was still $1.1 \pm 0.1 \times 10^{-4}$ Bμ counting in Sμ with the target under a vacuum. This number is automatically subtracted from the scaler Sμ when the dead-layer correction (Sec. IV. A) is made, since the xenon analysis does not distinguish between muons stopping in the front window and those stopping in the plastic scintillator dead layer. At any rate, this window correction is very small and well within the uncertainty of the over-all dead-layer correction.

The output of the circuit Sμ is scaled twice, once directly out of Sμ and once after a discriminator set to fire on all Sμ pulses. Readings on the two Sμ scalers agreed throughout the run to within

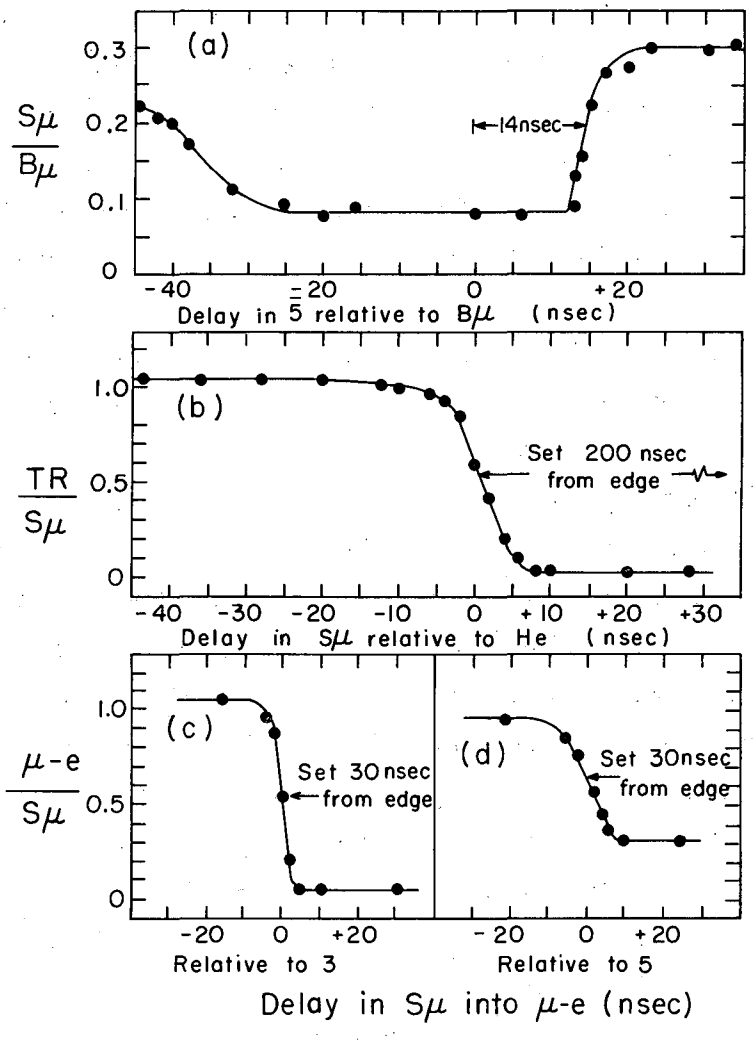

Fig. 16. Important delay curves.
(a). Delay of the veto 5 into the coincidence Sμ was set at 0 during the run. Decay electrons coming between 0 and 14±2 nsec veto their own Sμ.
(b). Relative delay of Sμ and prompt (beam) He pulses into the coincidence TR. An Sμ delay of 200 nsec from the edge of this curve was added under operating conditions so that only He pulses occurring 200 nsec after an Sμ made a coincidence in TR.
(c). Relative delay of 3 and Sμ into μ-e, and
(d). Relative delay of 5 and Sμ into μ-e. An Sμ delay of 30 nsec from the edge was added in each case so that only 3 or 5 pulses occurring 30 nsec after an Sμ made a coincidence in μ-e.

10 counts in a million. Another output of Sμ starts a time-to-pulse-height converter that is stopped either by a decay electron or by a TR event. In addition the circuit Sμ generates a pulse used to gate the coincidence circuit TR. This pulse was 6.2 μsec long and is shown in Fig. 17(b). The discriminator following Sμ generates a 10.6-μsec pulse that gates the μ-e circuit. This discriminator is scaled and forms one input to the μ-e logic system (see Sec. III. F. 8).

It was noted during the experiment that in order to have a constant 6.2-μsec gate, it was necessary that the amplitudes of the activating pulses be between ≈1 and 3 volts. Too large or too small an input pulse shortened the gating pulse to about 0.1 μsec. Since constancy of the gate length is essential to the experiment, the pulses going into Sμ were made uniform by a tunnel-diode discriminator.

4. Triton-Recoil Circuit and Time Gate

The 6.2-μsec pulse from Sμ forms a delayed coincidence (see below) in the circuit[65] TR with pulses coming from the dynode of the He counter. Pulses from the dynodes of counters $\bar{3}$ and $\bar{5}$ are amplified, delayed with respect to one another, and mixed by means of a passive network (a tee of 47-ohm resistors). The mixed output is amplified and split again passively. One output of the tee goes to the μ-ē circuit and the other through a delay box to the TR veto. We set the delay with Sμ out of TR and with beam electrons which all pass through $\bar{3}$, 4, and $\bar{5}$. Thus any $\bar{3}$ or $\bar{5}$ pulse occurring within about 20 nsec of a He pulse will veto the TR event. This feature prevents many of the decay electrons and all second-beam particles from registering on the pulse-height analyzer (PHA). A negligible 0.025% of the true TR events are vetoed by random $\bar{3}$ or $\bar{5}$ pulses.

There are three outputs of the circuit TR. The first goes to a scaler. The second stops a time sorter started by Sμ; thus we can measure the time distribution of TR events [see Fig. 20(b) and Sec. III. F. 7] and verify that they indeed have the characteristic decay spectrum. The third output is a 160-nsec pulse that gates the helium pulse going to the PHA [see Fig. 17(c)].

Fig. 17. Selected oscilloscope traces.

(a). Integrated pulses of counter B1 showing the gross structure of the beam. The spike at the end of each accelerating cycle, representing a high counting rate, causes the scalers to miss counts; we therefore electronically gate the scalers off during this part of the beam spill. The top trace shows the scaler gating pulse (≈ 2 msec/cm).

(b). TR gating pulse from the circuit Sμ (2 V/cm, 6 μsec/cm).

(c). TR output gate to the linear gate (2 V/cm, 0.1 μsec/cm).

(d). Pulses from the helium scintillator after the linear amplifier and before the linear gate (0.2 V/cm, 0.1 μsec/cm).

(e). Output from the linear gate. These pulses are then integrated and analyzed according to pulse height. The small bumps mark the beginning and the end of the gating pulse. These are integrated out to zero by the integrating amplifier (0.2 V/cm, 0.1 μsec/cm).

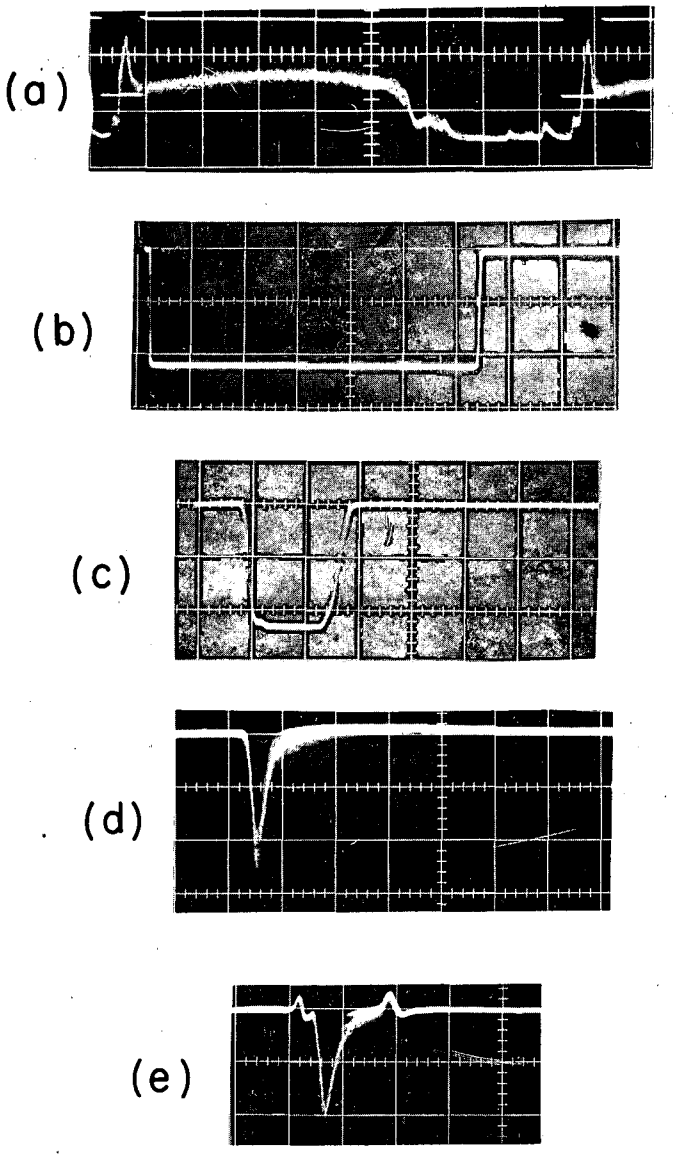

ZN-4291

Fig. 17

The 6.2-μsec pulse from Sμ is delayed from a prompt coincidence to prevent the stopped-muon pulse in the helium counter from registering in TR. It is important to know between what time, t_1 to t_2, after a stopped muon that a He pulse will register in TR. Since triton recoils follow an exponential law with mean life $\tau = 2.189$ μsec (the inverse of the muon-disappearance rate in He^3), one must correct the observed events for those that come before t_1 or after t_2. The fraction of muons disappearing between t_1 and t_2 is $F_t = \exp(-t_1/\tau) - \exp(-t_2/\tau)$, and therefore the total number of events occurring over all times is the observed events divided by this fraction.

We measure the time t_1 by "doing" a delay curve between the prompt He pulse and the Sμ pulse. This delay curve is shown in Fig. 16(b) and was obtained with $\bar{3}$ out of TR. Note that this delay curve traces out the back edge of the He pulse; however, as indicated by the relative timing of the pulses in Fig. 35, the desired time t_1 is the additional delay added from the point where TR counts at half efficiency. A cable (RG 63/U) was used to delay Sμ. By measuring the frequency of standing waves in the shorted delay cable, we obtained a delay length of 202 ± 3 nsec, in which the error is due to a shift in the delay curve from the beginning to the end of the run.

The time $t_2 - t_1$, obtained by measuring the Sμ pulse length as described in Appendix C, is equal to 6.2 ± 0.1 μsec. Thus $t_1 = 202 \pm 3$ nsec, $t_2 = 6.4 \pm 0.1$ μsec, and the time factor

$$F_t = \exp(-0.202/2.189) - \exp(-6.4/2.189) = 0.858 \pm 0.003. \qquad (62)$$

5. Pulse-Height Analysis

Delayed pulses from the He counter's anode are sorted according to energy (pulse height) in order to pick out pulses arising from the 1.9-MeV triton recoil. The pulse height from the He counter was very sensitive to small shifts in the photomultiplier's high voltage; hence this voltage was monitored carefully with a digital voltmeter so as to keep gain shifts to less than a channel. In order to prevent saturation of the pulses in the last stages of the photomultiplier tube,

the voltage of the He counter was kept relatively low. An amplifier compensated for this low voltage in order to make the pulse through the gating circuit an optimum volt or so [see Fig. 17(d)]. The He anode signal was delayed so that it fell within the gating pulse [Fig. 17(c)] provided by TR, which in turn was generated by He's dynode signal. Figure 17(e) shows the He pulses as they appear after the gating circuit. The integrating amplifier,[66] following the gating circuit, was necessary to generate the relatively wide pulses required by the PHA. It also integrated over the area of the pulses, thus making the output-pulse height closely related to the total amount of light generated in the helium gas. Finally the pulses were analyzed according to pulse height in the PHA. The resulting pulse-height spectra, along with the $S\mu$ scaler counts, are the basic data of the experiment.

If the μ-e logic were used (see Sec. III. F. 8), a 14-μsec delay line (consisting of RG 176/U cable with a 2200-ohm impedance) was inserted between the integrating amplifier and the PHA. This delay line brought the pulse to be analyzed into coincidence with the pulse from the μ-e logic system. Except for one run, the 14-μsec line and the prompt coincidence on the PHA were not used.

By adjustment of the gain on the amplifiers, the 1.9-MeV triton-recoil peak could be made to fall in any channel desired. During any given run, however, the gain stayed the same. This was checked by frequent calibrations with an α source. Periodically throughout the experiment, the linearity of the pulse-height-analysis system was checked by replacing the He counter with a pulse generator. A typical plot of the variation of the helipot dial on this pulse generator (controlling the pulse amplitude) with the channel number in the PHA is shown in Fig. 18(a). This shows that the amplifier, linear gate, integrating amplifier, and PHA form a linear system up to channel 110, where the integrating amplifier saturates. Figure 7 shows that even with the addition of the He counter the system is still linear.

Several times during the experiment the PHA was checked to be sure that it was storing all input pulses and that it did not lose

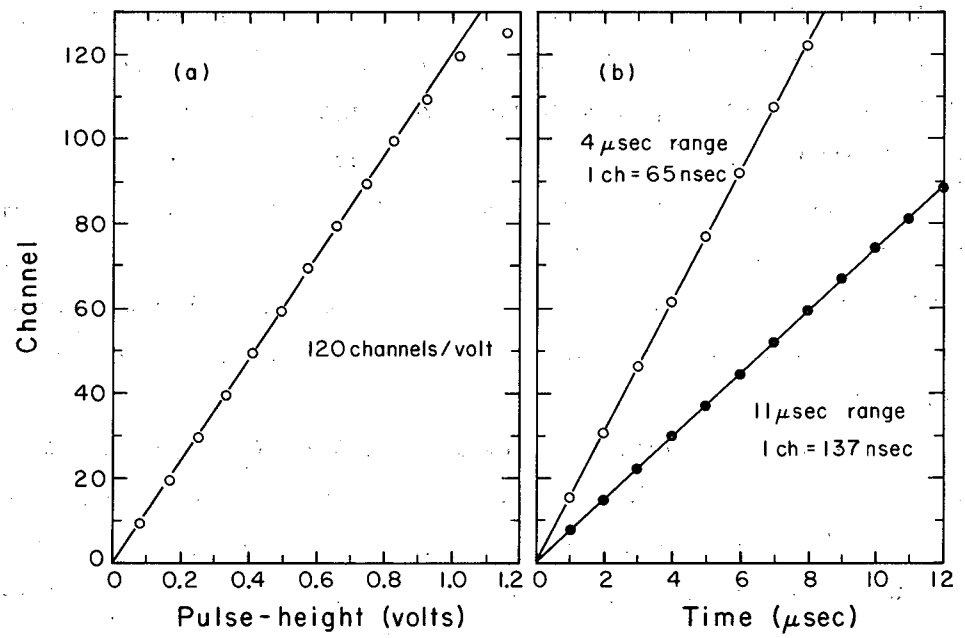

Fig. 18. Typical pulse-height analyzer calibrations.
(a). Channel number vs pulse height of a standard generator pulse showing the linearity of electronics from amplifier to PHA. Note that some nonlinearity does occur at about channel 110 and that above channel 120 the system saturates.
(b). Calibration of two ranges of the Wieber time sorter by the method described in the text.

counts from its memory. All tests showed that the PHA was operating properly; however there was no continuous monitor throughout the data-taking runs on the number of counts being stored. The tests with the pulse generator showed that large pulses, which normally would be off-scale on the PHA, were instead stored in the PHA between channels 120 and 134 because of electronic saturation. Thus no matter how large the He pulse, it still registered on the PHA. These saturated pulses can be used in obtaining the integrated number of counts above a given energy and were used in obtaining the capture rates for the breakup reactions.

6. The μ-e Circuit

Most of the stopping muons decay into electrons. Some of these electrons are detected by the μ-e coincidence circuit as follows. A pulse from Sμ, signifying a stopped muon, fires a discriminator that generates a 10.6-μsec pulse (see Appendix C). This pulse makes a coincidence in the μ-e circuit[65] with a signal coming from either counter 3 or counter 5. Since all beam particles trigger a pulse in counter 3 as the muon stops, the 10.6-μsec pulse from Sμ is delayed 35 nsec from a coincidence with such prompt pulses [see Fig. 16(c) and (d)]. Thus μ-e is sensitive from 35 ± 7 nsec to 10.6 μsec after a muon stops, and therefore will detect only 97.6 ± 0.4% of the electrons because of this time gate.

Like TR, the μ-e circuit also has three outputs. The first goes to a scaler, which counts μ-e events; the second goes to the μ-e logic system; and the third stops a time sorter. This time sorter starts to time whenever an Sμ coincidence occurs. Thus the time sorter measures the time intervals between arrival and decay of muons.

Experimentally the number of μ-e events obtained was 84.6% of the Sμ events if counter 5 only were used as input to μ-e. As explained in Sec. III. F. 8, 2.1% of these were determined to be random events, leaving 82.5 ± 0.3% for real observed decay electrons. This number can also be calculated as a check on several aspects of the

experiment. The probability of registering an incoming muon is the product of the probability of decay times the geometric efficiency. The geometric efficiency for detecting a decay electron in counter 5, as computed by the Monte Carlo program (see Appendix D), is $85.6 \pm 0.5\%$ of the $S\mu$ counts. The probability of decay in the finite time gate is 0.967. Taking into account that 0.8% of the $S\mu$'s are captured (mostly in the dead layer, as explained in Sec. IV. A), we finally get $82.8 \pm 0.6\%$ of $S\mu$ as observed decay electrons in counter 5. This checks well with the experimental number given above.

Because of its small solid angle and because many of the decay electrons stop in the front Lucite window, the copper elbow, or the pressure-vessel flange, counter 3 detects only $1.9 \pm 0.5\%$ of the decay electrons. Considering that counter 3 has a rate of randoms as high as 3.1% of $S\mu$, it does not appear that counter 3 is very useful as an electron detector, which was its original purpose. As it turned out, the main reason for using counter 3 was as a veto in the circuit TR. Here it vetoed about 2% of the beam particles that otherwise would appear as random background on the TR pulse-height spectrum.

7. Time Analysis of Events

The time sorter[67] is a device that converts the time interval between two pulses into a pulse height that is proportional to this time interval. The resulting pulse height is measured on a PHA. The main purpose of doing the time analysis is to be sure that both μ-e and TR events showed an exponential decay with the 2.2 μsec mean life characteristic of muon decay. Other experimenters have measured the free-muon mean life using much more accurate methods and have obtained $\tau_{\mu^+} = \tau_{\mu^-} = 2.200$ μsec.[6] Taking the measured capture rate into account, one then obtains 2.189 μsec for the muon mean life in He^3.

The time sorter also plays an important role in the xenon analysis (see Sec. IV. A.). Zero time on the distribution, important in the xenon analysis, is defined as the time at which a muon stops. The channel in which zero time occurs on the time distribution can

be varied by changing the relative delay of the start and stop pulses going to the time sorter. An extra 1.3 μsec was added to the stop-pulse delay to shift zero time from the start pulse. This is done to avoid any distortion of the time distribution for early times due to finite-rise-time effects in the PHA. The exact position of zero time on the distribution is measured by varying the delay of the Sμ pulse going to μ-e so that prompt beam pulses stop the time sorter.

Calibration of the time sorter, by means of the circuit shown in Fig. 19, proceeds as follows. Pulses 1 μsec and pulses 1 msec apart are generated synchronously in the Tektronix Time Mark Generator. The pulses 1 msec apart trigger the circuit Sμ, which then starts the time sorter. Meanwhile these same pulses go through a Del-A-Gate[60] and form a coincidence with the pulses occurring every 1 μsec. The coincidence-circuit output stops the time sorter. By changes in the Del-A-Gate delay, the time sorter is stopped at 1-μsec intervals from the Sμ starting pulse. The results are in the form of spikes (in certain channels of the PHA), which therefore are 1 μsec apart. Figure 18(b) shows typical calibration plots for the two ranges of the time sorter. Figure 20(a) and (b) shows typical time distributions of μ-e events and TR events, respectively. The mean life of μ-e events, obtained with a least-squares fit to the data points, is 2.19 ± 0.03 μsec; the error is due mostly to uncertainty in calibration of the time sorter. Of the normal TR events, almost 80% were actually low-energy pulses due to decay electrons that missed being vetoed. In order to measure the time distribution of TR pulses due only to nuclear-capture events, we set the TR discriminator to bias out events with energy below 1.2 MeV. The time distribution of Fig. 20(b) is with this high bias on the TR discriminator. In this case the lifetime is 2.23 ± 0.08 μsec; the error is due to statistical uncertainties. Both of the measured lifetimes agree well with the expected value and thus show that the effects we measured are related to a muon stopping in helium.

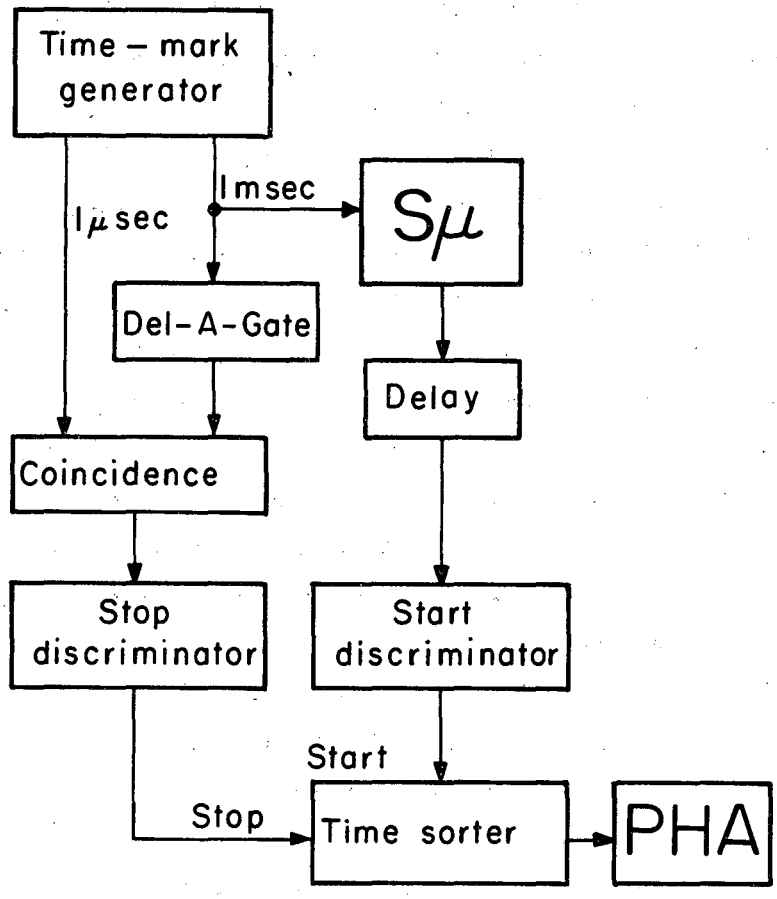

Fig. 19. Circuit used in calibrating the time sorter. The time-mark generator generates a string of pulses 1 μsec apart, and at the same time, in synchronism, another string 1 msec apart. With the Del-A-Gate, the delay of the 1 msec pulses can be continuously varied.

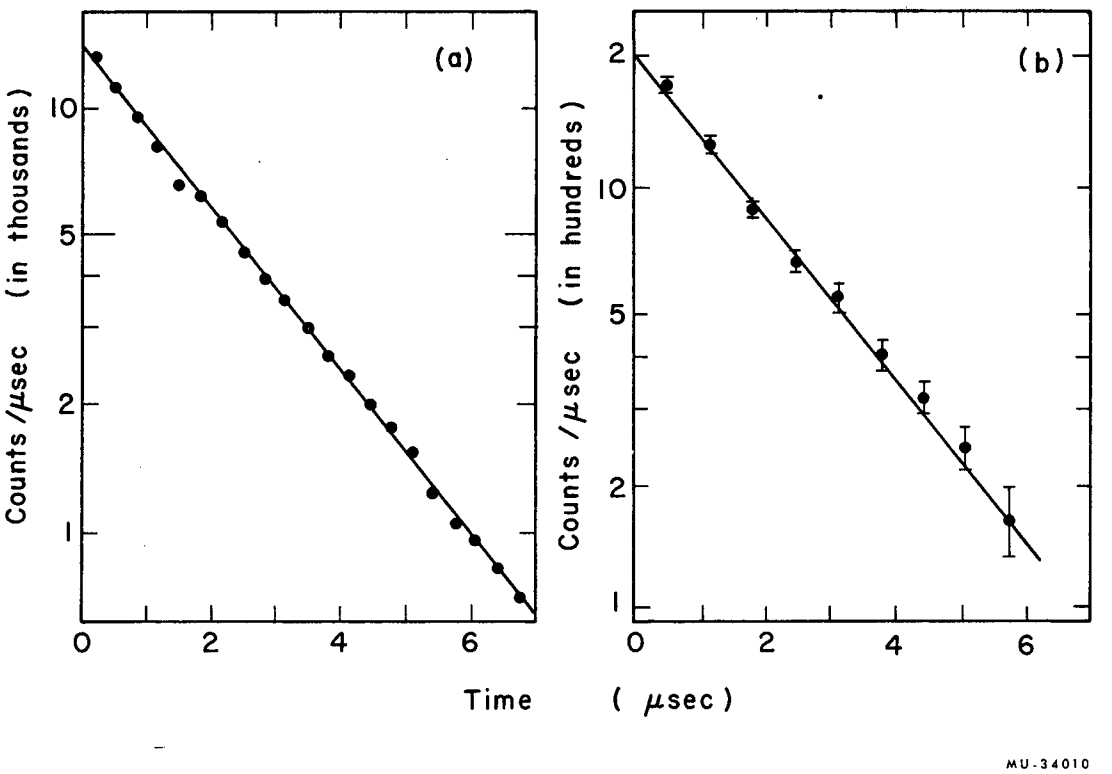

Fig. 20. Time distributions. (a). μ-e events; τ = 2.19±0.03 μsec. (b). TR events; τ = 2.23±0.08 μsec. In the measurement of TR events, the low-energy decay electrons were biased out; thus this time distribution mainly represents muon-capture events of the type shown in Eqs. (3), (4), and (5).

8. The μ-e Logic System

A given muon can "die" only once. Therefore, if a muon decays into an electron there can be no capture event and one should not look for such events on the pulse-height analyzer. Ideally one could not get a TR event and a μ-e event for the same Sμ. However, random events not connected with an Sμ (such as cosmic rays and neutron or gamma-ray background from the cyclotron) do occur in both TR and μ-e. The μ-e logic system is designed to eliminate a large fraction of the randoms occurring in the pulse-height spectrum by requiring that no TR event can register on the PHA if a μ-e event occurs in the first 10.6 μsec after a stopped muon. Since the μ-e coincidence "sees" ≈ 84% of the decay electrons, the μ-e logic will reduce the number of PHA randoms by this amount.

This logic system was used only on one short trial run for two reasons: (a) the randoms in the pulse-height spectrum were smaller than expected and could be measured in any event (see Sec. IV. D) and (b) the random events in μ-e itself led to the cancellation of good triton-recoil events and thus introduced an additional correction and therefore an additional error in the result. However, for the sake of the record, I describe how the μ-e logic system works.

Between stopped muons, a standard bistable multivibrator called the Set-Reset (S/R) flipflop remains in the reset position. Any μ-e event, which of course requires an Sμ, sets this flipflop. The delayed pulse from Sμ (occurring after the μ-e time gate) resets the flipflop and causes it to trigger a scaler and a 11-μsec pulse that feeds into a simple anticoincidence circuit as the veto. That is, if the S/R flipflop goes from a set to a reset position, no pulse comes from the coincidence. If however there was no μ-e event, the flipflop does not get set in the first place. In this case the delayed pulse from Sμ is delayed another 1 μsec (to ensure overlap with the 9-μsec veto pulse, if it is present) and then generates an 8-μsec pulse, which feeds through the coincidence to a scaler and the PHA. The 14-μsec delay from the integrating amplifier to the PHA is chosen so that all possible events occurring in the

6.2-μsec TR time gate also fall in the 8-μsec pulse from the μ-e logic. The 14-μsec delay is necessary since one must wait for at least the 11 μsec of the μ-e time gate to see whether or not a μ-e event occurs.

Thus the net effect of the μ-e logic system is to allow pulse-height analysis of only those delayed He events not accompanied by any event in either 3 or 5. Note that the $\bar{3}$ or $\bar{5}$ veto in TR also prevents events immediately associated with a pulse in 3 or 5, such as decay electrons, from registering on the PHA, but that the μ-e logic in addition kills all TR events occurring before or after the μ-e event.

The S/R scaler also allows an immediate computation of the number of randoms occurring in μ-e. The scaler μ-e can count twice for a given Sμ, for instance, once for a real decay electron and once for a random; however, the S/R scaler will count only once since the S/R flipflop gets reset only once for a given Sμ. Thus the number of double counts in μ-e is just (μ-e) - S/R and the number of randoms per Sμ in μ-e is just [(μ-e) - S/R]/(μ-e). In this manner and by calculating the number of expected second-beam particles in 10.6 μsec after the stopped muon, one can determine the various amounts that each counter contributes to randoms in μ-e. The following table shows as percentages of Sμ counts the number of randoms occurring in μ-e.

	Counter		
	3	5	3 + 5
Beam randoms	2.1	1.5	2.1
Nonbeam randoms	1.0	0.6	1.6
Total randoms	3.1	2.1	3.7

Note that beam particles that hit counter 5 also hit counter 3 and hence cause a random count only once. The nonbeam randoms are caused mostly by a background of neutrons and gamma rays from the cyclotron.

Because of these randoms in μ-e, some good TR events are vetoed by the μ-e logic criterion. To calculate the number of vetoed TR events, V, let T' be the observed TR events and T be the true number of events so that T = T' + V. Then it follows that

$$V = T \times (\text{probability per } S\mu \text{ of getting a random})$$
$$= (T' + V) \times (\mu\text{-e} - S/R)/\mu\text{-e} . \quad (63)$$

Solving this equation for V, one obtains

$$V = T' \times \left(\frac{\mu\text{-e}}{S/R} - 1\right) \quad (64)$$

and so

$$T = T' \times \left(\frac{\mu\text{-e}}{S/R}\right) . \quad (65)$$

For the run during which the μ-e logic was used, the scaler ratio

$$\frac{\mu\text{-e}}{S/R} = 1.040 \pm 0.001 \quad (66)$$

was obtained where the quoted error is statistical only. The actual error is larger than this since fluctuations in the beam level will change the number of μ-e randoms. Estimating that the beam fluctuation could lead to 1% error, we must then correct the observed number of TR events on the PHA by the factor 1.04 ± 0.01.

G. Data Collection

The first 2 weeks of the cyclotron run were spent in a beam study, in systematically delaying and plateauing the various counters, and in checking the operation of the electronics with He^4 in the target. After this initial setup, about a month was spent (≈ half time on the cyclotron) in collecting data. In this section I first describe the routine followed in the data gathering and then present the data itself.

1. Data-Collecting Procedure

Each day before beginning a group of runs, the radius and azimuth of the Be cyclotron target and the quadrupole currents were checked. Generally the bending-magnet current was varied to maximize the number of stopping muons. This was necessary since small changes in the target position could change the beam's momentum. The composition of the beam, as determined by the time-of-flight

analysis, was checked daily, as was the Bμ coincidence. (See Fig. 14 and Sec. III. F. 2). Except for maintenance of the LN reservoir, the helium target did not require attention and the gas pressure remained constant.

Data were usually accumulated in blocks of 500 000 Sμ, each of which represents about 3 hours of running time at full beam. After each block of data, the scaler counts were recorded and the PHA's memory transcribed. These blocks of data were later totalled for each type of run. Periodically, while accumulating data for each block, we also checked counter high voltages, the bending-magnet current, scaler gating, counting rates, and scaler ratios for consistency.

After every million Sμ's, a short run was made with the coincidence TR on singles He to measure the random background of the pulse-height spectrum (see Sec. IV. D). At this time an alpha-source calibration, and calibrations of the PHA and of the time sorter, were usually made.

Once at the beginning and once at the end of all the data gathering, all vital delay curves and pulse lengths were checked. During the data-gathering period many miscellaneous checks were made and subsidiary data were accumulated.

2. Pulse-Height Spectra

Pulse-height spectra with He^3 in the target were taken in five main runs, during which the experimental conditions were varied to check for systematic errors. The runs are summarized in Table II. Run A was made at the beginning of data gathering and Run B about 2 weeks later; otherwise these two runs were made under identical conditions at 28.9 atm of helium. These runs are kept separate only to show the consistency of the data. The only change made during the LP (low-pressure) run was the lower gas pressure at 15.4 atm. During the logic run the μ-e logic system (see Section III. F. 8) was used. In addition, run B3 was made without $\bar{5}$ in the TR coincidence and with a 2:1 attenuator before the linear amplifier. This made it

Table II. Summary of the data runs made during the experiment.

Run	Type	Purpose	Pressure (atm)	Number of events	Running time (hr)	Data blocks	χ^2 per deg of freedom	$P(\chi^2)$
A	$\mu^- He^3$		28.9	12 000	24.3	9	0.26	2%
B	$\mu^- He^3$	Muon capture	28.9	14 000	27.8	11	1.44	16%
LP	$\mu^- He^3$	He^3 into H^3	28.9	11 000	47.1	11	0.64	22%
Logic	$\mu^- He^3$	ground state	15.4	6 000	12.1	5	1.37	24%
B3	$\mu^- He^3$	Muon capture	28.9	7 000	10.4	5	0.98	40%
B4	$\mu^- He^4$	(He^3 / He^4) into all channels	28.9	2 000	10.8	4		
C	$\mu^- He^4$	Study of	28.9	-	11.2	5		
	$\mu^+ He^3$	backgrounds	28.9	-	17.5	7		
	$\mu^- Xe$	Study of "dead layer"	3.4 - 7.0	-	17.8	11		

possible to see more of the breakup reactions [Eqs. (4) and (5)] since the breakup proton and deuteron have relatively high energies and many normally veto themselves in counter 5.

Two main runs were made with He^4 in the target. The first, B4, was identical to B3 except for the gas used, and was an effort to observe capture events in He^4 [Eq. (9)]. Since the objective of the second He^4 run was to study the electron and breakup backgrounds, it was made under conditions similar to Runs A and B. In addition, a run with positive muons was made in order to check the shape of the electron background. Several additional runs, made with xenon in the target, allowed a measurement of the "dead layer" thickness (see Sec. IV. A).

Figure 21(a) through (h) shows the raw pulse-height spectra for each of the above sets of data. Also shown on these graphs are the computed random spectra (see Sec. IV. D). Each spectrum is the sum of a number of data blocks. For each block of data a rough capture rate was computed and assigned a purely statistical error. The goodness-of-fit parameter, χ^2, for the sum of these data blocks is also given in Table II. These χ^2 show that the data is consistent with a purely statistical variation from one run to the next.

3. Other Data

In addition to the basic pulse-height spectra of delayed events of muons stopping in helium, other information was collected to aid in the interpretation of the data. Generally whenever a pulse-height spectrum was being obtained, the time distributions of the TR events were also recorded on another PHA to be sure that the TR events had the correct lifetime. These spectra are similar to Fig. 20(b) but are not shown here since no additional information is obtained from them. A time distribution of μ-e events is given in Fig. 20(a) and discussed in Sec. III. F. 7. The xenon time distributions are discussed in Sec. IV. A.

By removal of the 200-nsec delay of the He pulse going into TR, the coincidence circuit TR was allowed to fire on prompt He

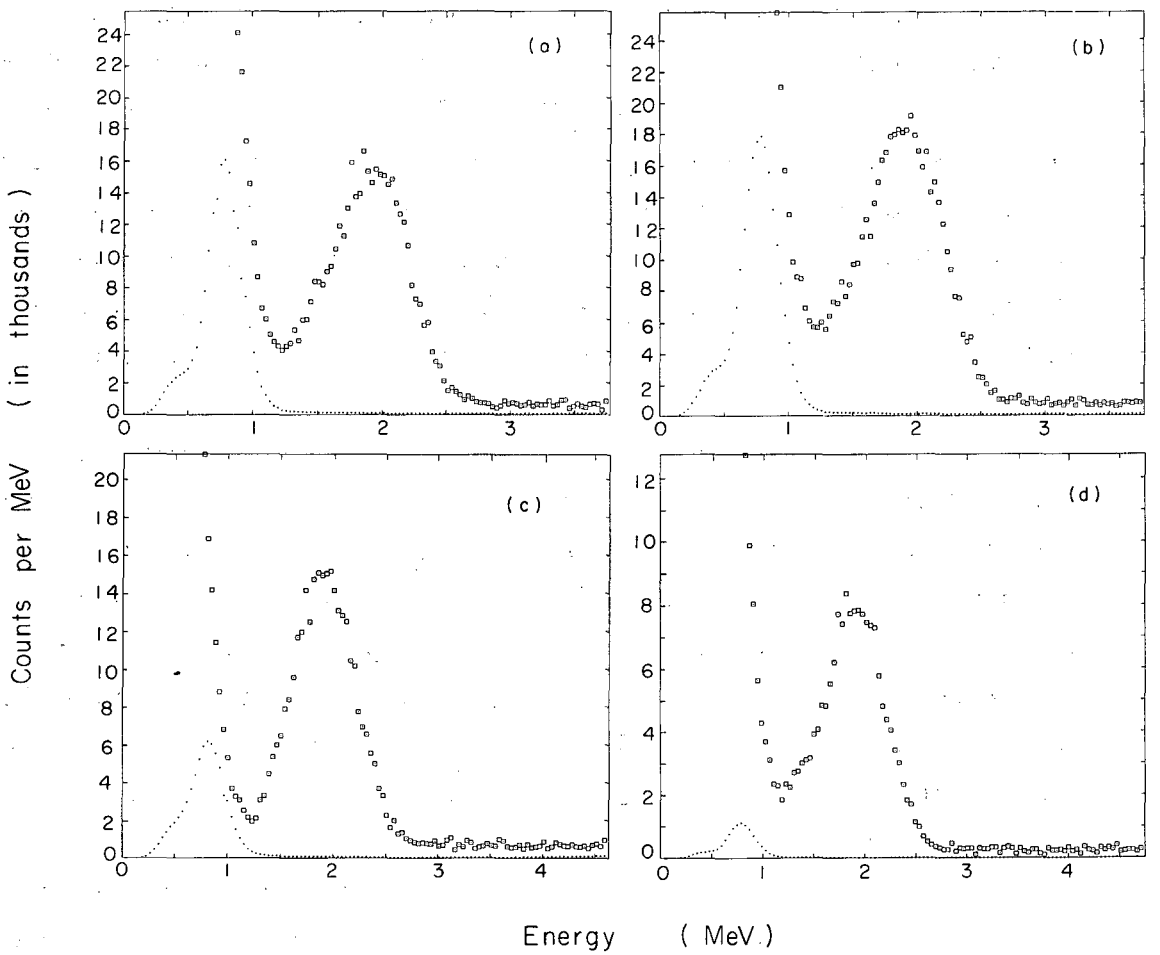

Fig. 21. Pulse-height spectra for each of the major sets of data. (a). Run A, (b). Run B, (c). LP run, (d). Logic run. The squares are the raw counts in each PHA channel and the dots are the random events calculated for each run.

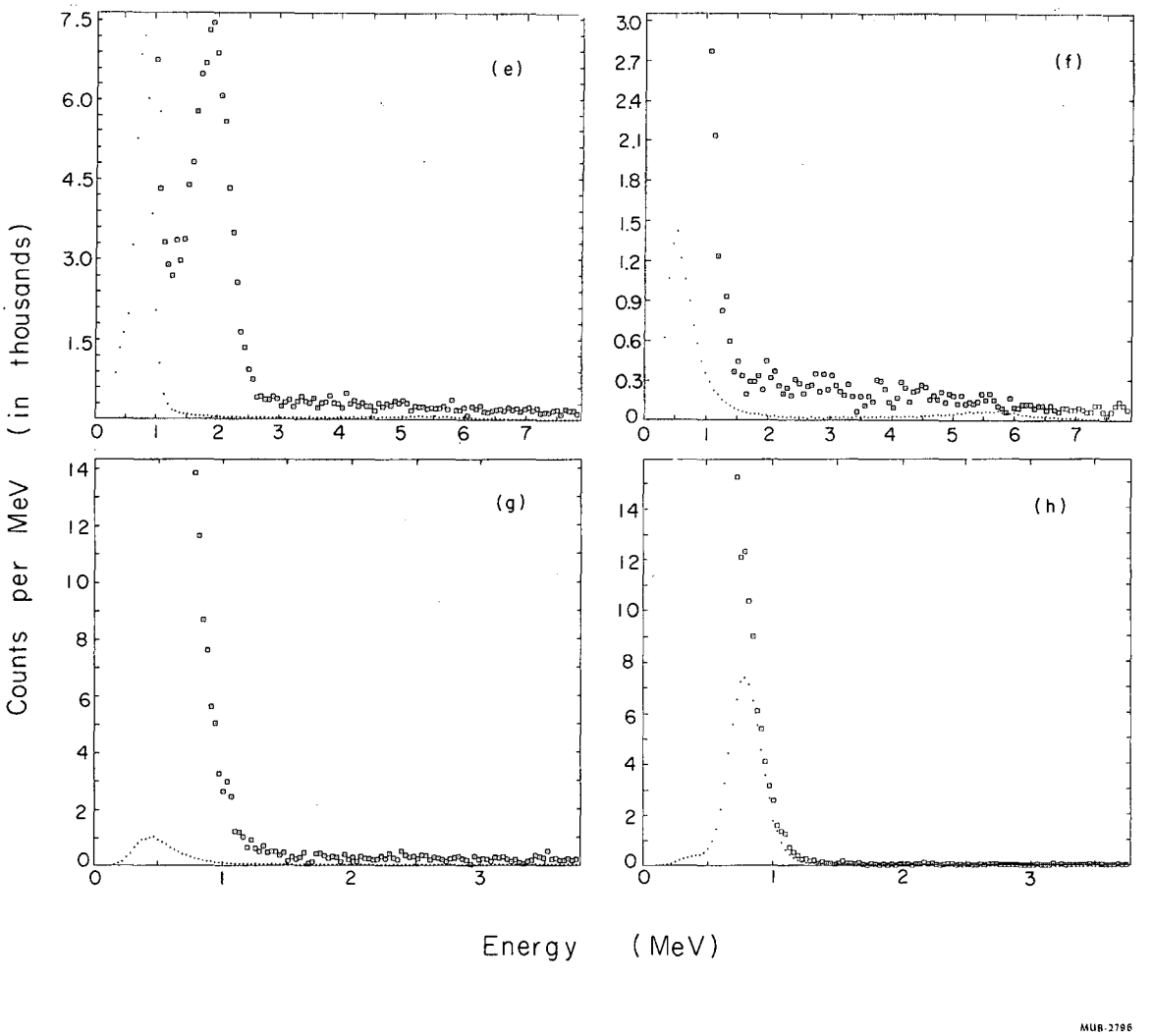

Fig. 21. (continued). (e). Run B3, (f). Run B4, (g). Run C, and (h). $\mu^{+}He^{3}$ run.

pulses and thus distribution of the energy lost by muons stopping in the gas could be obtained. This energy spectrum is shown in Fig. 22 and served as a useful check of the Monte Carlo program (see Appendix D).

A graph of the (S_μ/B_μ) versus gas pressure for both helium and xenon is given in Fig. 23. The positive-pressure intercept is related both to the "dead layer" and to the light given off by the window, as is explained in Appendix D.

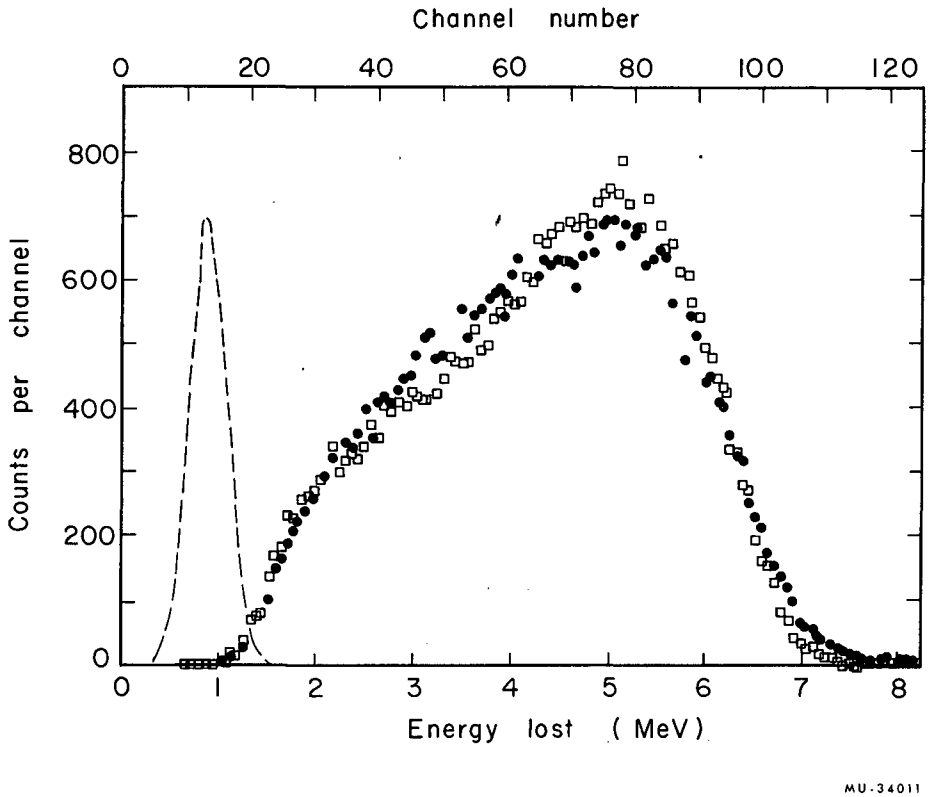

Fig. 22. Spectrum of the energy lost by muons stopping in helium. □ , experimental points; ●, points calculated by the Monte Carlo program, normalized to the same number of stopped muons. The dashed line represents the 0.85 MeV lost in the Lucite window with the He counter's resolution folded in. Notice that the small overlap between this Gaussian and the energy spectrum indicates that the Sμ discriminator was set correctly to bias out muons stopping in the window.

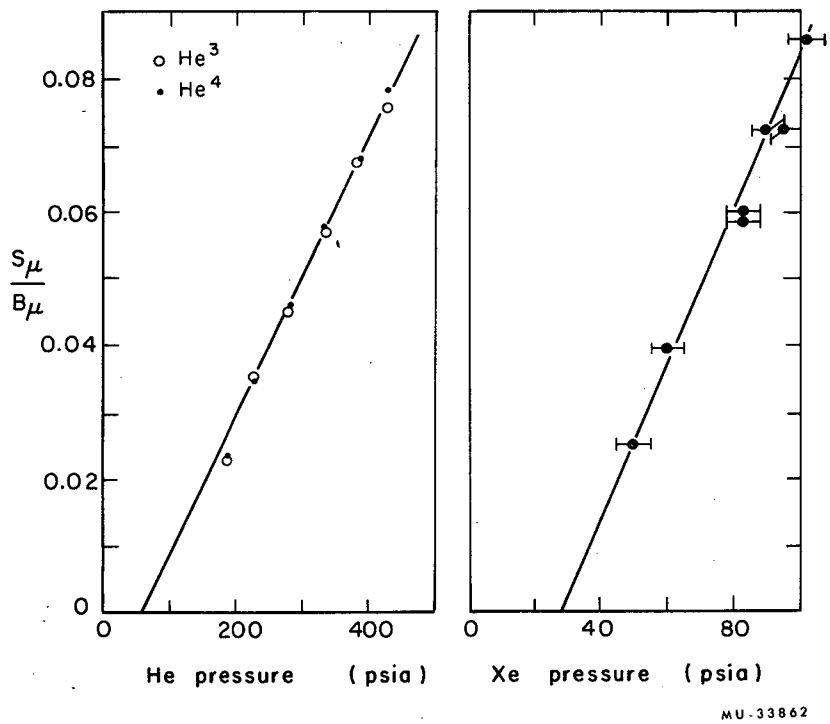

Fig. 23. Variation of $S\mu/B\mu$ with pressure for He^3, He^4, and Xe. The low value at 200 psia is due to the pressure variation of light output from the helium scintillator (see Fig. 5). The positive-pressure intercept arises partly from the MgO "dead layer" and partly from a high energy cut to discriminate against muons stopping in the Lucite window.

IV. DATA ANALYSIS

In this section I describe how the data were analyzed and calculate the capture rates in He^3 and He^4. I first describe the xenon analysis and then compute the number of muons stopping in the helium gas for each run. Next I discuss the pulse-height spectra and the backgrounds associated with those spectra. Then I give a short description of the Monte Carlo program used in analyzing the breakup events, followed by the calculation of the capture rate in He^4 and the breakup-capture rate in He^3. Consideration of events arising from muon capture in the walls show these to be a factor in the breakup capture rates. Finally I arrive at the $He^3 \rightarrow H^3$ capture rate by combining previous results with a correction for triton recoils that hit the wall of the gas container.

A. Xenon Analysis and the Dead-Layer Correction to S_μ

Not all of the muons that register in the coincidence circuit S_μ actually stop in the helium gas. Some muons stop in the "dead layer" that surrounds the gas, that is, in the cup-coating materials or in the cup counter itself. Most muons that stop in the cup counter veto themselves in S_μ; however some do not penetrate deeply enough into the cup counter to give sufficient light to be vetoed. These muons must be subtracted from the S_μ counts in order to get the true number of muons stopping in the helium. This correction was determined experimentally by replacing the helium with xenon gas and performing a time analysis of $\mu \rightarrow e$ decays (see Sec. III. F. 7). Figure 24 shows a typical time distribution of μ-e events with xenon in the target. Muons stopping in xenon have a very short mean life (90 nsec),[12] whereas muons stopping in the low-Z materials of the dead layer have mean lives of about 1 μsec. Determination of the number of muons stopping in the dead layer from this spectrum is rather involved, but the following describes how it was done.

The "dead layer" consists principally of four elements: magnesium, oxygen, aluminum, and carbon. The MgO powder was smoked onto the cup-counter walls over an opaque coat of Al. Even

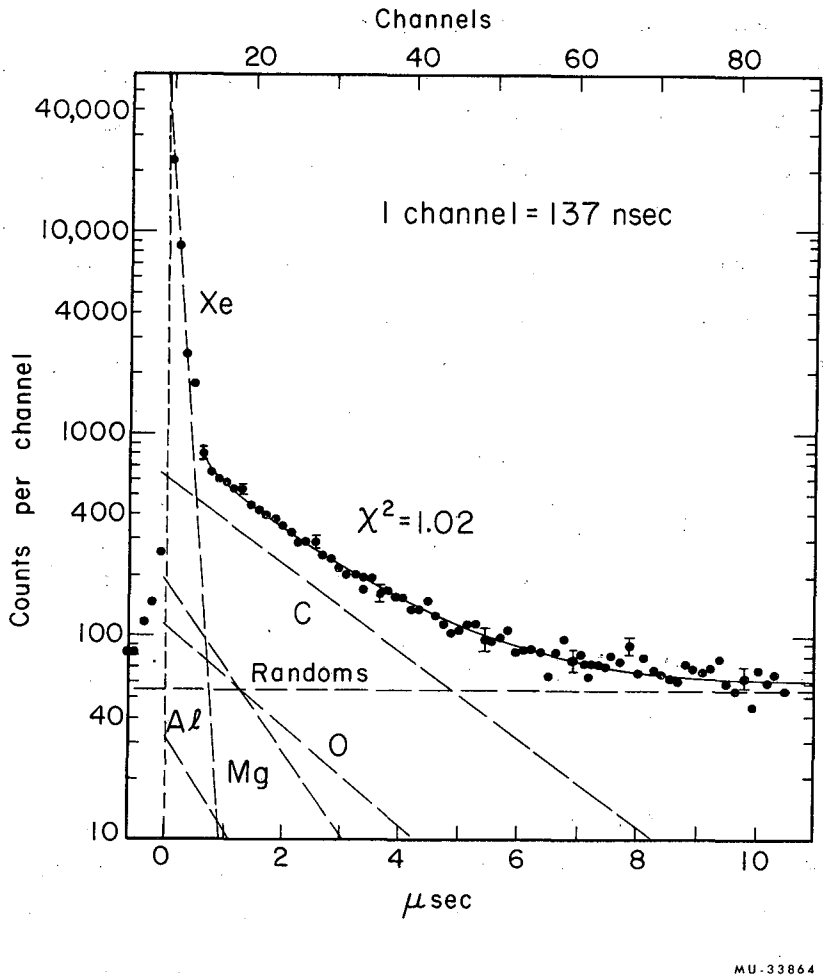

Fig. 24. Time distribution of μ-e events for 6.75×10^6 Bμ with 6.1 atm of xenon in the target. The dashed lines show the contributions of muons that stop in the various elements of the dead layer. The Mg, O, and Al exponentials were computed as described in the text, and the Xe, C, and randoms were determined by a least-squares fit of the spectrum. The solid line is the least-square fitted sum of the exponentials. Its computed χ^2 per degree of freedom is 1.02.

though the gas permeates the MgO powder, it was assumed that this did not affect the number of muons stopping in the gas versus the number stopping in the MgO. Since the hydrogen mesic atom is neutral, any muons that stop in the hydrogen of the plastic scintillator (CH) cup counter are very quickly transferred to carbon atoms through collisions. Thus muons stopping in the cup counter will have the same mean life as if they stopped in carbon. Line 3 of Table III gives the mean life of the muon in the various elements and line 5 gives the fraction of muons that stop in that element and that give a decay electron. The rest of the muons, of course, are captured, and it is assumed that these muons do not cause a signal in counter 5.

From the time distribution (Fig. 24) one can see that it would be very difficult to extract the number of muon stops in all four elements. Furthermore, we can measure the amount of MgO and Al present in the cup counter. Thus the procedure followed was to determine how many counts corresponding to stops in MgO and in Al one would expect to see in the time distribution, subtract these, and use the remaining counts to determine the number of muon stops in carbon.

The total weight of the MgO (measured after the experiment) was 0.45 ± 0.02 g; the area of the cup counter covered was 485 cm^2 (4 inches in diameter by 5 inches long); thus the average MgO thickness was 0.93 ± 0.04 mg/cm^2. When one assumes that the Fermi-Teller Z Law[68] (the atomic-capture rate in a compound is proportional to the Z of each element) holds true in MgO, then six-tenths of the muons that stop in MgO are captured by magnesium and four-tenths by oxygen. The aluminum coating was about 3000 Å or 0.09 ± 0.03 mg/cm^2 thick. Knowing the relative stopping powers of Mg, O, Al, and He, one can obtain an equivalent-helium-gas thickness of 0.51 mm at 28.9 atm pressure for all three elements. Then, knowing the distribution of stopping muons (see Sec. III-E.), one can find the percentage of muons stopping near the side walls in this equivalent thickness of gas. Since the beam spreads as it moves further from the collimator, one must average over various distances from the front of the cup.

Table III. Calculation of the dead-layer correction to Sμ.

1.	Element	Mg	O	Al	C
2.	Atomic number	12	8	13	6
3.	Muon mean life[12] (μsec)	1.04	1.81	0.88	2.025
4.	Muon mean life (channels)	7.6 ± 0.3	13.2 ± 0.6	6.4 ± 0.3	14.8 ± 0.6
5.	Fraction of muons giving off a decay electron	0.47	0.82	0.40	0.92
6.	Time-gate factor	0.971	0.980	0.966	0.980
7.	Solid angle × time gate × fraction of decay electrons (≈1% error)	0.434	0.763	0.367	0.856
8.	Number of dead-layer stops/Bμ	$5.7 \pm 0.6 \times 10^{-4}$	$3.8 \pm 0.4 \times 10^{-4}$	$0.85 \pm 0.3 \times 10^{-4}$	$12.5 \pm 2.5 \times 10^{-4}$
9.	Observed decay electrons/Bμ	$2.5 \pm 0.3 \times 10^{-4}$	$2.9 \pm 0.3 \times 10^{-4}$	$0.3 \pm 0.1 \times 10^{-4}$	$10.7 \pm 2.1 \times 10^{-4}$
10.	$N_o/B\mu$	$3.3 \pm 0.4 \times 10^{-5}$	$2.2 \pm 0.3 \times 10^{-5}$	$0.48 \pm 0.16 \times 10^{-5}$	$7.25 \pm 1.4 \times 10^{-5}$

In this way 1.09% of the S_μ (gas) is found to stop in the side walls [S_μ (gas) is the number of S_μ counts from muons stopping only in the gas, not in the dead layer]. To obtain the number stopping in the back wall of the cup counter, one can form a ratio of wall thickness to gas thickness (after correcting for the spreading of the beam) and thus obtain 0.33% of S_μ (gas) stopping in the back wall. Thus a total of $1.42 \pm 0.15\%$ of S_μ (gas) counts are muons that stop in the MgO and Al.

The number of muons stopping in the dead layer should be independent of the gas pressure and directly proportional to the number of incident-beam muons (B_μ). Since S_μ depends on the gas pressure and since we used several gas pressures, it is convenient to convert from dead-layer stops per S_μ to dead-layer stops per B_μ. From the scaler S_μ/B_μ ratio of 0.077 ± 0.002 (at the helium pressure of 28.9 atm) and the ex post facto knowledge of the fraction of S_μ counts in the dead layer, one obtains S_μ (gas)$/B_\mu = 0.074$. Thus one obtains $1.05 \pm 0.1 \times 10^{-3}$ dead-layer stop per B_μ. Line 8 of Table III shows how this is divided among the Mg, O, and Al, taking into account the Fermi-Teller Z law. Note that carbon numbers (lines 8, 9, 10) on this table are not calculated as the above but are determined from the time spectrum, as described below.

Knowing the dead-layer stops per B_μ, one must now determine how many decay electrons one will see on the time spectrum. Five percent of the decay electrons miss counters 3 and 5 because of the geometrical arrangement. The time gate on the μ-e circuit (see Sec. III. F. 6) is open only between 30 nsec and 10.6 μsec after a stopped muon, and hence the μ-e circuit will count only $\exp(-0.03/\tau) - \exp(-10.6/\tau)$ of the electrons. This fraction is shown on line 6 of Table III with the various muon lifetimes in each element taken into account. Finally one must account for the captured muons that do not give off a decay electron. Line 7 of Table III shows the product of these three factors and is the fraction of stopped muons that gives off an observable decay electron. Line 9 gives the number

of observed decay electrons per B_μ, and line 10 gives this number divided by the muon mean life τ (in channels, with 137 nsec equal to one channel), where N_o is the initial rate of muon decay. Multiplication by the B_μ counts for each particular run gives N_o for the time spectrum. Finally, having obtained both parameters, N_o and τ, in the exponential decay law $N = N_o \exp(-t/\tau)$, one can subtract the Mg, O, and Al contributions from the time distributions. These contributions can be seen in Fig. 24, which is the time distribution of μ-e events for 6.75×10^6 B_μ with 6.1 atm of xenon in the target.

In order to help detect systematic errors, runs were made at xenon pressures of 3.4, 4.1, 5.6, 6.1, 6.5, and 7.0 atm. From each of the time distributions, the MgO and Al contributions were subtracted and a least-squares fit made with the remaining spectrum; a constant random background and two exponentials (one with the xenon and the other with the carbon lifetime) were assumed. The three parameters of the least-squares fit were the randoms/channel and N_o for xenon and carbon. The average N_o/B_μ obtained was $7.25 \pm 1.4 \times 10^{-5}$ counts/channel. Multiplication of N_o/B_μ by τ gives the observed decay electrons/B_μ and division by 0.856 (see Table III, line 7) gives the carbon dead-layer stops/B_μ = $12.5 \pm 2.5 \times 10^{-4}$. The quoted error represents the maximum variation of the carbon counts at the various xenon pressures. There was a small tendency towards more carbon counts at higher xenon pressures; however the variations from one pressure to the next showed a scattering that would be about what one would expect from fitting the carbon exponential. Summing the Mg, O, Al, and C contributions, one gets $2.3 \pm 0.3 \times 10^{-3}$ dead-layer S_μ/B_μ; the quoted error is a bit conservative. This is the number used in correcting the scaler S_μ counts and corresponds to a dead-layer thickness of about 2.2 mg/cm^2 (equivalent of C) or about 1.1 mm of He^3 gas at 28.9 atm.

Two other checks were made with the xenon spectrum. The amount of MgO and Al subtracted from the time spectrum was decreased by 10%, and the best least-squares fit then gave about 11%

more carbon counts, which almost compensated for the smaller MgO and Al used. In a second check, the high voltage on counter 5 was decreased by 150 volts (out of 3100 volts) to see how much this would change the dead layer. This represents about a 2:1 variation in the pulse height of unsaturated pulses from counter 5. The analysis of a xenon spectrum under this condition showed that the dead layer increased 25%. These checks show first that the dead-layer correction is relatively insensitive to the MgO and Al subtraction; and second that the dead layer is insensitive to small changes in the high voltage or amplifier gain.

B. Number of Stopping Muons

Table IV lists the pertinent numbers used in calculating the number of muons stopping in the helium gas for each of the runs. The discussion in Sec. IV. A demonstrated that $[(2.3 \pm 0.3) \times 10^{-3} \times (B_\mu \text{ scaler counts})]$ muons are expected to stop in the dead layer surrounding the gas; these are subtracted from the S_μ scaler counts. To this is added that fraction (0.55% of S_μ) of the muons that are vetoed by their own decay electrons (see Sec. III. F. 3). Since other corrections are negligible, one thus obtains the final corrected number of muons stopping in the helium. Note that the error in S_μ is $\approx 0.5\%$ at the high gas pressures and $\approx 1\%$ at the low gas pressures. The "dead-layer" correction contributes the largest part of this error.

Other possible corrections to the S_μ rate include random S_μ events, short TR-gate pulses, two stopping muons within the same TR gate, and S_μ events for which the stopping particle is not a muon. By delaying the B_μ pulse one rf-pulse separation (an additional 54 nsec) with respect to the S_μ coincidence, we determined that there were no random S_μ events in 10^4 B_μ. Occasionally if the input pulse were too large, the S_μ circuit generated a scaler pulse without generating a 6.2-μsec TR-gating pulse. This was corrected by standardizing all the pulses going into S_μ, and to the best of our knowledge all TR gates were uniformly 6.2 μsec long. A second stopping muon occurring in

Table IV. Corrected numbers of stopping muons (in thousands).

Run	Bμ scaler counts	Sμ scaler counts	-Dead layer Sμ $(2.3 \pm 0.3 \times 10^{-3} \times B\mu)$	+Decay electron vetos $(5.5 \pm 1.1 \times 10^{-3} \times S\mu)$	Corrected number of stopped muons
A	56 073	4250 ± 2	129 ± 17	23 ± 5	4144 ± 18
B	65 920	5109 ± 2	152 ± 20	28 ± 6	4985 ± 21
A + B	121 993	9359 ± 3	281 ± 37	51 ± 10	9129 ± 39
LP	116 585	4004 ± 5	268 ± 35	22 ± 5	3758 ± 36
Logic	28 808	2250 ± 2	66 ± 9	12 ± 3	2196 ± 10
B3	25 455	2000 ± 1	59 ± 8	11 ± 2	1952 ± 9
B4	26 167	2000 ± 1	60 ± 8	11 ± 2	1951 ± 9
C	26 463	2000 ± 1	61 ± 8	11 ± 2	1950 ± 9

the 6.2-μsec TR gate could give a good TR event and not be counted in S_μ because of the inhibit from B_μ. Since the S_μ rate was ≈ 50/sec with a duty factor of ≈ 0.5, the probability of second muons occurring in the same gate is $\approx 0.06\%$, which is negligible compared to the error in S_μ.

Pions and electrons in the beam should not stop in the helium because of range considerations. As a test we set the B1-B2 delay such that the coincidence circuit B_μ triggered on electrons. One "electron" in 1600 triggered an S_μ count; however, the $(\mu\text{-e})/S_\mu$ ratio indicated that these "electrons" were mostly "good" muons with the wrong timing in B_μ. This could happen because the high counting rate in B1 causes random coincidences with good muons passing through counter B2. Similarly, when the B_μ coincidence was set to trigger on pions, there was one S_μ count in 300 B_μ counts; again the $(\mu\text{-e})/S_\mu$ ratio indicated that most of these were really muons. In addition to random B_μ events discussed above, these false-pion triggers could be due to pions that decay in flight and to real muon coincidences that overlap the pion peak. (Figure 14 shows that considerable overlap occurs between the pion and muon peaks.) Thus, there appear to be no additional corrections to the S_μ rate.

C. Pulse-Height-Spectra Shapes and Curve Fitting

The energy spectra of Fig. 21(a) through (e) all show the 1.9-MeV triton-recoil peak. We want to know the number of counts in this peak in order to calculate the $He^3 \rightarrow H^3$ capture rate. In addition to statistical variation of the number of recoil counts, there are three major backgrounds that complicate the computation of the capture rate. The sharply rising background at low energies is from μ to e decays in which the electrons miss the veto counters. The shape of this electron background was established from the runs on $\mu^+ + He^3$ and $\mu^- + He^4$. Random background was measured to an accuracy of $\approx 15\%$ and is discussed in Sec. IV.D. The remaining background is due mainly to muon capture resulting in many-body final states [Eqs. (4) and (5)]. This breakup background contributes

the largest uncertainty in the determination of the number of triton-recoil counts; however, a measure of it determines the total-capture rate in He^3. The runs with μ^- stopping in He^4 [Fig. 21(f) and (g)] of course do not show any recoil peak but have a spectrum similar to the He^3 case in other respects. The run with μ^+ on He^3 has only the decay-electron background as it should since positive muons are not captured.

Initially an attempt was made to separate the triton peak from the background by fitting the spectra to a shape consisting of two Gaussians plus a linear background. The shape function used was

$$f(x) = A + Bx + \frac{C}{\sqrt{2\pi}\,D} \exp\left[\frac{-(E-x)^2}{2D^2}\right] + \frac{F}{\sqrt{2\pi}\,G} \exp\left[\frac{-(H-x)^2}{2G^2}\right], \tag{67}$$

where A through G are adjustable parameters and x is the PHA-channel number. A least-squares-fitting program[69] varied the parameters of this function until the goodness-of-fit parameter

$$\chi^2 = \sum_{\text{all channels}} \frac{(y - f(x))^2}{(\delta y)^2} \tag{68}$$

reached a minimum. In this expression y is the number of counts in the channel x with error δy and f(x) is the function defined above for the same channel x. Once a minimum was reached, the program also calculated the error matrix[70]

$$G_{mn} \equiv \frac{1}{2} \frac{\partial^2 \chi^2}{\partial a_m \partial a_n} \tag{69}$$

(where a_m are each of the parameters), and finally gave the rms error for each parameter according to the expression $\delta a_m = \sqrt{(G^{-1})_{mm}}$ where G^{-1} is the inverse of the error matrix.

Table V summarizes the results of the curve fitting. The coefficient C is the number of counts under the triton Gaussian and is the main parameter of interest. Each value of C is the average

Table V. Curve fitting results.[a]

1. Run designation	A	B	LP	Logic	B3
2. Counts in triton-recoil peak (coefficient C)	11125	13200	10600	5855	5323
3. Coefficient C per million $S\mu$	2685	2648	2820	2666	2727
4. Error in C	± 1.9%	± 2.1%	± 1.5%	± 2.2%	± 1.9%
5. χ^2 per degree of freedom	2.20	1.98	1.03	1.33	1.74

a. Assumes a linear background subtraction extrapolated from above the triton-recoil peak.

of several fits with different low-energy cutoff channels. Since there are about 80 degrees of freedom in each case, any value of χ^2 above ≈ 1.3 represents a poor fit to the data. The low-pressure data form the only spectrum that fits f(x) very well. The logic data is on the border line; but the χ^2 for runs A and B represent especially bad fits. A close inspection of the spectra in Fig. 21 (a) and (b) reveals that the triton peak is asymmetrical for A and B, and thus could not be expected to fit a Gaussian shape very well. A Poisson shape fits the triton peak even less well. Consequently, except for the LP data and possibly the logic data, shape fitting does not lead to trustworthy results and was not used in the final data analysis. It is comforting to note, however, that the results of the LP and logic curve fitting agrees exceedingly well with the final triton-count determination (see line 2 of Table VIII).

D. Random Background

The random background of the pulse-height spectra of TR events was measured by allowing the TR coincidence to fire on every He pulse. Thus, we obtained the pulse-height spectrum of singles in the He counter and were able to compute the random spectrum to be subtracted from the raw data. During a given data run the circuit

TR can respond to single He events for $(6.2 \times 10^{-6} \times S\mu)$ second, since the $S\mu$ gate is 6.2 μsec long. From the He-singles data one obtains the rate of single events to be
(singles counts)/(running time × DF); DF is the duty factor of the cyclotron and must be included because the clock keeps running even when there is no beam. Duty factors typically ranged from 0.55 to 0.60 and were measured by observing the beam structure on an oscilloscope [See Fig. 17(a) and Sec. III. D]. The circumstance that the beam also has rf structure is unimportant since the $S\mu$ gate length is large compared to the rf period of 54 nsec. The random events to be subtracted from the data are thus given by

(singles rate) × (time TR is open) =

$$\frac{6.2 \times 10^{-6} \times S\mu \times (\text{singles counts})}{(\text{singles running time in seconds}) \times DF} .$$

The random-background pulse-height spectra are shown for each set of data in Fig. 21. All further data analysis was carried out with these random shapes subtracted from the raw data (also shown in Fig. 21). Most of the random events arise from thermal neutron reactions in He^3 according to

$$n + He^3 \rightarrow H^3 + p . \qquad (70)$$

This reaction releases 0.77 ± 0.02 MeV and accounts for the peak in the random spectrum with He^3 gas in the target. The runs with He^4 in the target show that the remaining random background is rather flat, except for a low-energy tail that may be associated with tritium decays but more likely is due to other neutron reactions. A small peak in the random background near 5 MeV occurs in runs B3 and B4. This peak is probably from Am^{241} that rubbed off the alpha source. Note that random charged particles should not constitute a background since in general they are vetoed in counters 3 or 5.

We estimate the uncertainty in the duty factor to be ≈ 15% and thus, since the other quantities have smaller errors, this is the error in the randoms calculation. Fluctuations in the beam intensity between the singles run and during the data run would also introduce an error in the randoms calculations. This effect is uncertain but we feel that the error is probably still included in the 15% uncertainty. The beam intensity was kept relatively constant during the runs, and singles runs were made fairly often between the main blocks of data to offset long-term-intensity variations. The randoms calculation was checked by delaying the S_μ to TR gate an additional 30 μsec after a prompt stopped muon. The long delay ensured that all activity associated with the muon had died away and thus all the TR events should be randoms. A run with 4×10^5 stopping muons then yielded 524 random events. The calculation involving the singles data gave 537 events and thus verified that the singles calculation is not far off. Any future and more accurate experiment should include a delayed gate that would measure the randoms simultaneously with the data collection.

Random background accounts for an area of ≈ 1.5% of the main portion of the triton-recoil peak. However, the low-energy tail of the peak extends into the region where the randoms become very large due to the neutron-induced reaction (70); hence, the randoms contribute to the confusion of measuring the counts in this region. Randoms contribute in about the same ratio to the low-pressure data; however, in the μ-e logic data, randoms are reduced by ≈ 85%, as discussed in Sec. III. F. 8. About 10% of the counts above the triton peak in the He^3 data are due to randoms. Similarly, ≈ 15% of the counts above the electron tail in the He^4 data are randoms, and these contribute to the uncertainty in the breakup reaction rate. The error introduced by randoms in the number of triton recoils is tabulated for each run on line 3b of Table VIII. Much of this uncertainty arises because the large neutron peak centered at 0.8 MeV lies just on the edge of the electron background and uncertainties in the randoms rate introduces additional uncertainty in the electron-background subtraction.

E. Decay-Electron Background

Considerable uncertainty in determining counts on the low-energy edge of the triton peak is introduced by the decay-electron background, which rises sharply until it is artificially cut off at ≈ 0.4 MeV by the He-TR discriminator. This background is due to electrons (from muon decay) that miss being vetoed in counters 3 or 5 and thus arises mostly from the 15% of the electrons that pass through the front hole in the cup counter. Normally one would expect a maximum of ≈ 0.5 MeV to be deposited by an electron in the gas; however, if the energy resolution of the He counter is taken into account, one can easily obtain the observed number of electron counts above ≈ 1 MeV. The decrease in electron background at low gas pressures indicates that most of the electron's energy is deposited in the gas.

The shape of the electron background that is to be subtracted from the pulse-height spectra is established from the runs $\mu^+ He^3$ and $\mu^- He^4$. The procedure followed was to subtract the capture events from the $\mu^- He^4$ data (run C) and normalize the resulting "electron tail" to the same number of S_μ as each of the other appropriate runs. The resulting spectrum agrees reasonably well with the $\mu^+ He^3$ data and with the gross shape of the electron background in runs A and B, and thus it was subtracted from runs A and B; this left only the triton peak and the breakup background. Similarly, run B4 was subtracted from run B3. In the case of the low pressure and logic runs there were no acompanying $\mu^- He^4$ or $\mu^+ He^3$ data and the electron background was obtained by curve fitting a Gaussian tail. Because the electrons lose less energy in the gas at low pressure, there was good separation between the TR peak and the electrons in the LP run. Thus, the error associated with uncertainties in the electron background in the LP run is very small. In contrast, the error due to the electron background in the logic run was rather large. An intermediate situation exists for the runs in which the He^4 data are used to subtract the electron counts. In these runs the electron background

shape is more certain than in the logic data; however, the overlap with the triton-recoil peak is ≈ 5 times greater than in the LP run. Furthermore, the He^4 subtraction is not exact because one must subtract two large numbers to get a small one, and thus statistical fluctuations and gain shifts play a large role. Estimates of the error introduced in the triton counts by the electron background are tabulated for each run on line 3c of Table VIII. Because the electron background is so large, any determination of the number of breakup events below ≈ 1.5 MeV is impossible.

F. Monte Carlo Program

In order to properly calculate the breakup background and to find the shape of the breakup-energy spectrum, it is necessary to account for a number of factors. Among these are the distribution of stopping muons, the energy resolution of the He counter, energy lost by the charged particle in the helium gas, the energy distribution of breakup events, and the probability that the charged breakup particle vetoed itself in counter 5. The most practical method of combining these factors to give a breakup shape is through a Monte Carlo program that simulates events. The program follows a particular muon, randomly choosing variable parameters according to specified distributions, and calculates quantities of interest. By summing over many muons, the program then produces the desired breakup spectrum. Simultaneously, the program calculates other quantities such as the decay-electron vetoing efficiency for counter 5, the number of triton recoils that lose part of their energy in the walls, the energy lost by a muon stopping in the helium, and the energy left by decay electrons in the gas. In Appendix D I discuss various aspects of the Monte Carlo program in detail.

Shown in Fig. 25 is a typical breakup-energy spectrum. The theoretical input-energy spectrum was in this case taken to be given by just the phase space distribution[71] of the deuteron in the reaction $\mu^- + He^3 \rightarrow d + n + \nu$. One can see the effect of the finite size of the gas scintillator, since in the output spectra there are no particles

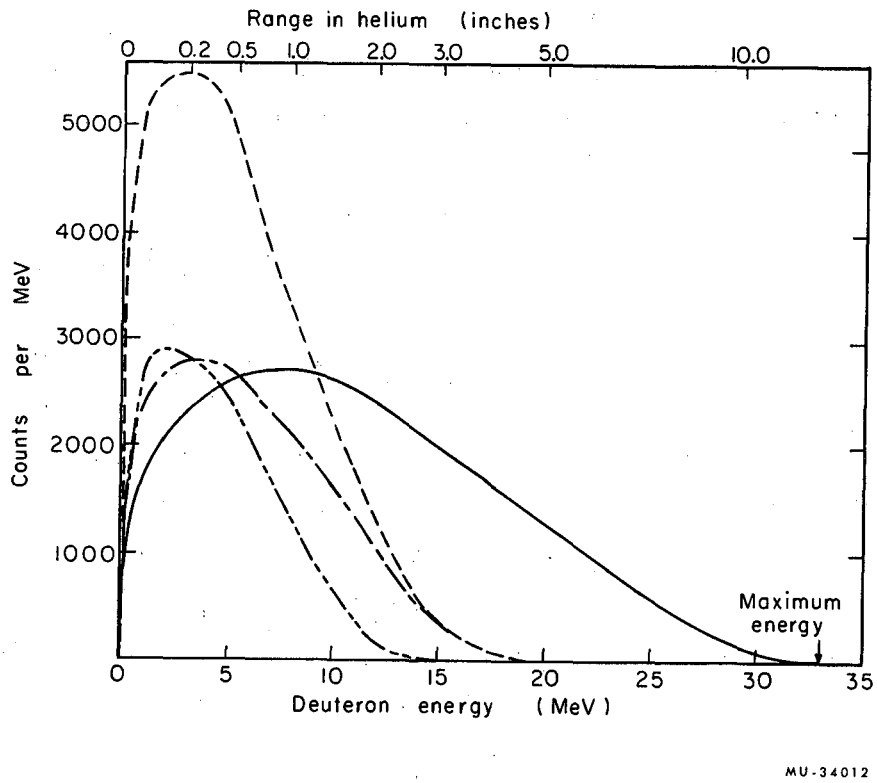

Fig. 25. Effects of the geometry of the gas scintillator on the shape of the deuteron-energy spectrum in the reaction $\mu^- + He^3 \rightarrow d + n + \nu$. A pure phase-space energy distribution was used as input to the Monte Carlo program. The program returned energy distributions for the various running conditions: veto on, veto off, high gas pressure, low pressure. The top scale on the graph indicates the range of the deuterons in the helium gas at high gas pressure (28.9 atm). ——, phase space; - - - veto off, HP; —·—, veto on, HP; — - -, veto on, LP.

with range greater than 5 inches. The higher energy particles leave only a part of their energy in the gas and then most pass into counter 5 with enough energy to veto themselves. During the runs (B3 and B4) where counter 5 was not used as a veto in TR, these higher energy particles would still show up on the spectrum but shifted to a lower energy. With counter 5 veto on, none of these particles will show up on the observed energy spectrum. Similarly at the lower gas pressure, the particles leave even less energy in the gas and more veto themselves.

G. Muon-Capture Events in the Wall

An estimate of the number of muons that stop in the wall and yet give a good TR event seems in order at this point. These wall events must arise from the muons stopping in the dead layer surrounding the helium gas, as discussed in Sec. IV. A. Table III lists each element of the dead layer, the fraction of the muons not captured, and the dead layer stops per B_{μ}. Combining these factors gives the following number of capture events per B_{μ}:

Element	Fraction captured	×	TR time-gate factor	×	Dead-layer stops/B_{μ}	=	Observable capture events/B_{μ}
Mg	0.53	×	0.822	×	5.7×10^{-4}	=	2.5×10^{-4}
O	0.18	×	0.867	×	3.8×10^{-4}	=	0.6
Al	0.60	×	0.796	×	0.85×10^{-4}	=	0.4
C	0.08	×	0.863	×	12.5×10^{-4}	=	0.8

Adding the contribution from each element one obtains $4.3\pm1.3\times10^{-4}$ wall captures per B_{μ} within the TR time gate. Table IV lists the number of B_{μ} for each run; thus the number of muons captured in the wall can be calculated rather well. Note that the low pressure run gives about twice the number of wall-capture events per S_{μ} as does the high-pressure data.

Not every muon that is captured in the dead layer gives a good TR event. One of the capture products must leave energy in the helium scintillator to be observed. The capture products consist

mainly of neutrons and gamma rays in complex nuclei. There may be ≈ 2% protons and alpha particles [72] but these are neglected in this section and discussed further in Sec. IV. J. If protons do arise from ≈ 2% of the capture events, they may contribute about the same number of TR events as the neutrons, since any proton going more than ≈ 1 cm in the gas will be detected. The gamma rays will not, in general, be detected, as their secondary electrons leave little energy in the helium. At any rate these electrons would be masked by the electron background. The major portion of TR events are expected to come from neutrons that collide elastically in the gas. The recoil helium could then be detected if it had sufficient energy.

More than one neutron may be emitted per muon capture. Neutron multiplicities in the light elements vary from 1.29 in Al to 0.76 in Ca. [73] Since, to my knowledge, neutron multiplicities have not been measured accurately in Mg, O, or C, a value of 1.0 ± 0.3 neutrons per muon capture is used in this calculation. The neutron-energy spectrum is assumed to be similar to that calculated in Refs. 74 or 75. The neutron-energy spectrum ranges from 0 to 20 MeV, with an average of ≈ 8 MeV, and does not vary drastically from one element to the next, so this approximation should be good to at least 50%. Using the total cross section vs neutron energy for neutron-He^3 and -He^4 scattering as given in Ref. 76, and folding in the stopping-muon distribution and the geometry (solid angle) of the helium scintillator, one can calculate how many neutrons interact in the helium. The results of such a calculation, which employs Monte Carlo methods similar to that outlined in Appendix D, give ≈ 1.3% of the capture products interacting in the helium at high pressure and ≈ 0.7% at low pressure. Note that the number of wall events detected per good S_μ is almost independent of the gas pressure. This is because fewer neutrons are detected at the lower gas pressure even though relatively more stop in the wall.

Although a neutron interacts in the gas, it does not leave all its energy in the gas. Assuming elastic collisions between the

the neutrons and the helium nuclei, and using differential cross sections given by Seagrave,[77] one can calculate how much energy is left in the gas by a neutron with a given energy. Combining all of the above factors, the neutron spectrum given by Bietti, for example, is transformed into the shape shown in Fig. 26. Since events less than 1.5 MeV are masked by the electron background, this leaves only one-fifth of the interacting neutrons in the observable-energy region. These could conceivably contribute to breakup events.

If the number of muons captured in the wall are multiplied by that fraction that give an observable energy loss in the helium, one obtains the numbers listed on line 3 of Table VI. Luckily these numbers are small compared to the observed events, but they are not quite negligible, especially in the He^4 case where they amount to $\approx 5\%$ of total events. It should be stressed that the calculation outlined above is accurate to only 50%. If the assumptions were not justified, or if additional factors must be taken into account, then the wall events may be more or less than the above calculation shows. This is discussed further in Sec. IV. J.

H. Calculation of the Muon-Capture Rate in He^4

Figure 27(a) and (b) shows the data with randoms subtracted for the runs with He^4 in the target (runs B4 and C). Only the spectra between 1.5 MeV, where the decay-electron background becomes large, and channel 115, where the pulse-height analysis system begins to saturate, was observed directly, and these points are shown on the graph. In addition to these points, however, the total number of events above channel 115 was measured (see Sec. III. F. 5). The number of events observed in each energy region is tabulated in the box on each graph, and the total observed events are listed on line 2 of Table VI. On line 3 is listed the number of wall events in the observable-energy region, as were calculated in the previous section. These are subtracted from line 2 to give the number of observed events in the helium. The remaining question is how many events lie in the region below ≈ 1.5 MeV masked by the electron background.

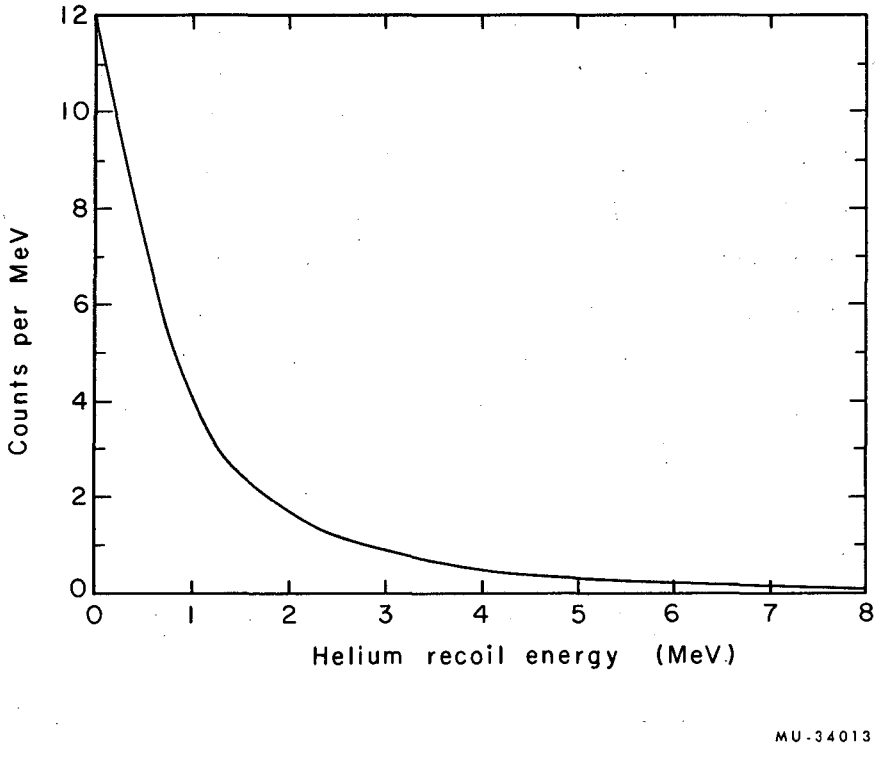

Fig. 26. Calculated distribution of helium-recoil energies from the elastic scattering of neutrons originating from 1000 muon-capture events in the "dead layer" surrounding the helium gas.

Table VI. He^4 and He^3 breakup events.

1.	Run designation	B4	C	B3	A+B	LP	Logic
2.	Observed events	1085±45	1080±45	1445±65	5490±130	2460±75	445±25
3.	Wall events in observable region	55±40	55±40	30±20	140±100	75±50	33±20
4.	Unobserved events	360±90	275±75	1070±540	4200±2100	2280±1200	1650±700
5.	Fraction of events not vetoed	1.0	0.95±0.03	1.0	0.824±0.061	0.726±0.085	0.824±0.061
6.	Corrected total number of events	1620±130	1590±120	2900±630	13500±3500	7500±1900	3070±1000
7.	Corrected number of stopped muons($\times 10^{-3}$)	1951±9	1950±9	1952±9	9129±39	3758±36	2196±10
8.	Breakup events per stopped muon($\times 10^{3}$)	0.830±0.066	0.816±0.065	1.48±0.33	1.48±0.37	1.99±0.50	1.40±0.46
9.	Breakup capture rate (sec^{-1})	378±30	372±30	675±150	675±170	910±230	635±210

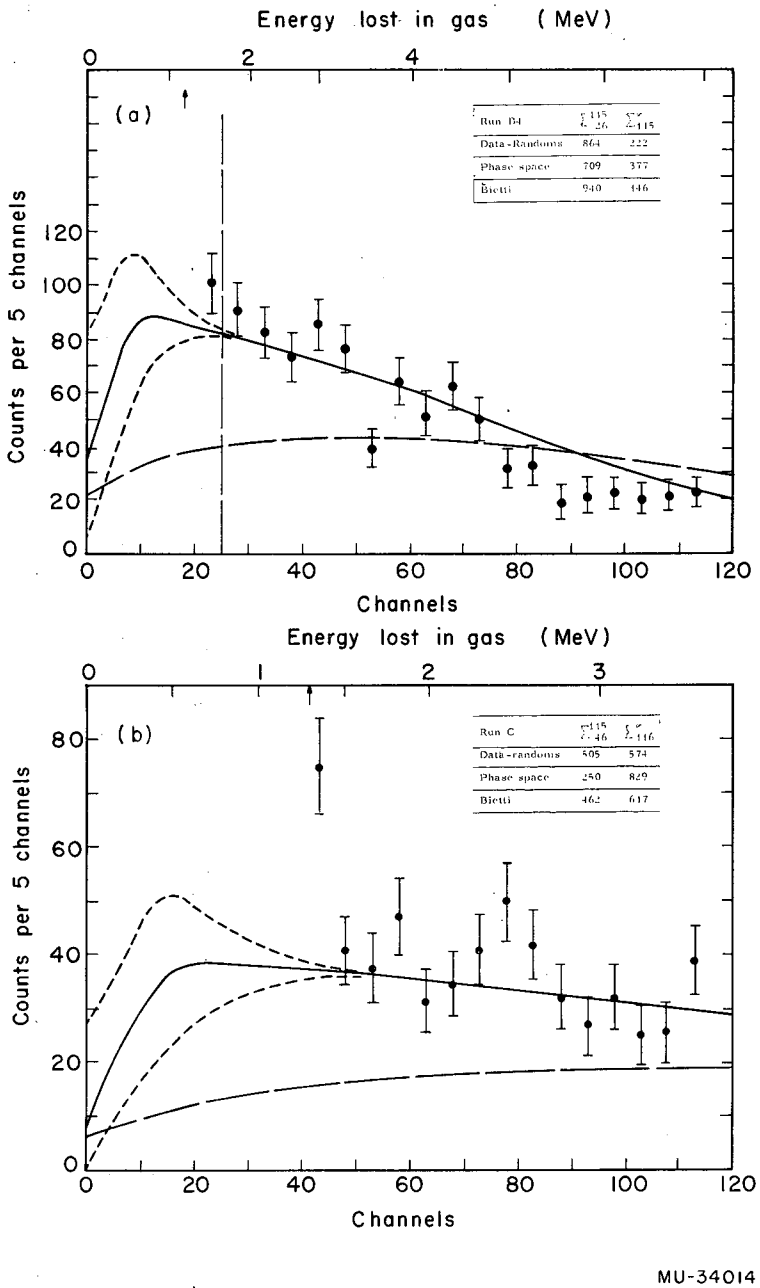

Fig. 27. Capture events in He^4. (a) Run B4, (b) Run C. The data points are with randoms subtracted and are summed over every five channels. - - -, normalized spectrum derived from a phase-space distribution; ——, spectrum derived from Bietti's distribution; ....., the rough effect of varying the counts below ≈ 1.5 MeV by 25%.

To determine these unobserved events, theoretical shapes with the counter geometry folded in by the Monte Carlo program were extrapolated to the region under the electron tail. Bietti and Di Porto[75] give an energy spectrum for the triton in the reaction (called Bietti's spectrum for convenience):

$$\mu^- + He^4 \rightarrow H^3 + n + \nu; \qquad (9)$$

this spectrum (their Fig. 2) is shown roughly in Fig. 28. In this case most of the tritons leave all their energy in the helium and thus folding in the counter geometry does not affect the spectra shape as much as in Fig. 25, for example. The observed spectrum thus almost follows the actual theoretical shape. If the theoretical shape (slightly altered by the counter geometry) is normalized to the observed number of capture events above the electron tail, one obtains the solid curves in Fig. 27(a) and (b), with the counts distributed as shown in the box on each graph. The agreement between the theoretical curve and the experimental data is not bad and shows that Bietti's theoretical spectrum is close to the actual spectrum. Because of poor statistics and knowledge of the spectrum over only a limited-energy region, not much more can be said about the actual spectrum shape. However, theoretical shapes that differ greatly from Bietti's spectrum can be ruled out. For example, if the phase-space distribution alone is used to get an energy spectrum, one obtains the dashed curves in Fig. 27(a) and (b). These curves disagree with the experimental spectra.

The number of "unobserved" counts under the electron background are listed on line 4 of Table VI, and are equal to the counts expected from the normalized Bietti shape. It is difficult to assign an error to these unobserved events; however, a ±25% variation in this number would seem to give reasonable error limits. A ±25% variation would have the effect on the theoretical-energy spectrum that is shown by the dotted lines in Fig. 27(a) and (b). Since the Bietti spectrum fits the data reasonably well, one would not expect a drastic change below 1.5 MeV, and thus the error is probably well

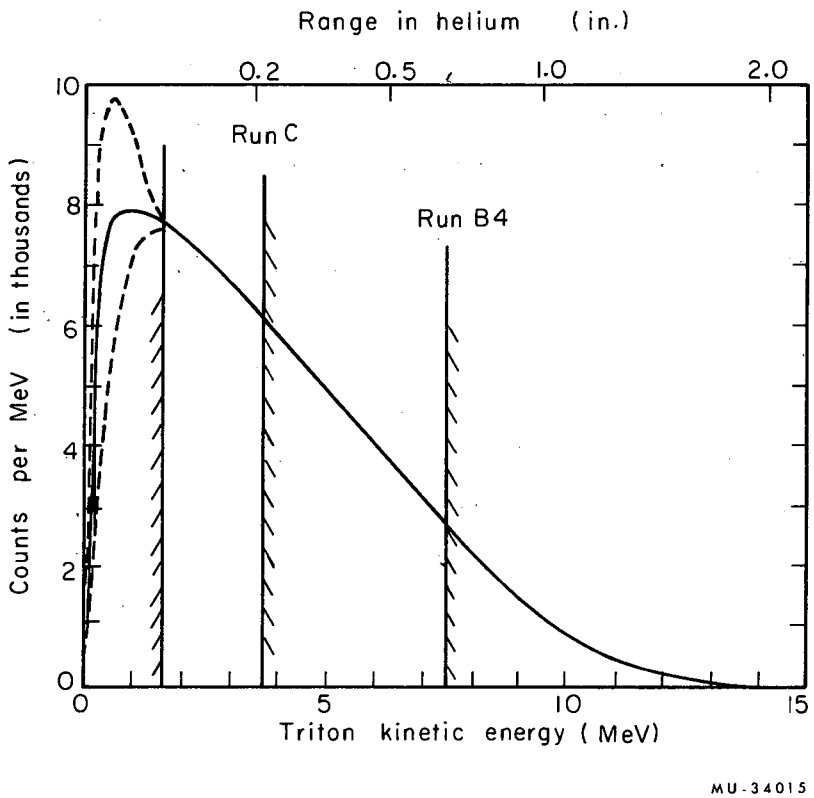

Fig. 28. Theoretical-triton-energy distribution for muon capture in He^4 (as given by Bietti and Di Porto) and containing 50 000 capture events. The top scale gives the range of a triton in helium at 28.9 atm. The shaded areas indicate the unobserved portions of the spectra and are different for runs C and B4. The dotted lines indicate the effect of varying by 25% the unobserved portion of the spectra below ≈ 1.5 MeV.

within this ±25% variation. It must be emphasized, however, that we really have no experimental information in this region of the spectrum.

Two additional factors complicate a determination of the capture rate in He^4. Besides Reaction (9), possible reactions include:

$$\begin{aligned} \mu^- + He^4 &\rightarrow H^3 + n + \nu + \gamma \\ &\rightarrow H^2 + 2n + \nu \\ &\rightarrow H^1 + 3n + \nu \end{aligned} \qquad (71)$$

There are also other possibilities. In this experiment, we can not distinguish tritons, deuterons, or protons, but can detect only the energy of charged particles irrespective of their mass. If any of these other reactions (71) occur in substantial amounts, they will modify the assumed theoretical spectrum, and thus the "unobserved" counts. For muon capture in He^4, however, Reaction (9) is expected to occur well over 90% of the time;[78] thus we neglect the other possible reactions. About all that can be said experimentally is that the data are consistent with Bietti's shape, which is for the triton reaction only. The second factor that changes any straightforward calculation of the capture rate is the presence of events in the pulse-height spectrum that are derived from muon-capture events in the walls of the gas container. Muons stopping in the dead layer surrounding the gas could furnish charged particles that would be detected in the helium gas. Further discussion of this is given in Sec. IV. J, but for now it too will be neglected.

With the above reservations, the muon-capture rate in He^4 can now be calculated. In run C the total number of events must be corrected for the 5% that veto themselves in counter 5. This fraction of events that is vetoed is determined by the Monte Carlo program and depends on the assumed theoretical-energy distribution. In addition to this factor, the total number of events is multiplied by 1.1655 ± 0.004 to correct for the finite TR time gate (see Sec. III. F. 4). The corrected total number of events is listed on line 6 of Table VI.

Dividing by the number of stopped muons and multiplying by the free muon decay rate then gives the muon-capture rate in He^4. These results are also listed in Table VI. The two runs are in excellent agreement and average to give a capture rate of:

$$\Lambda (He^4) = 375 \pm 30 \text{ sec}^{-1}. \tag{72}$$

It must be stressed that the error is almost entirely due to the uncertainties in the "unobserved" events and thus is only an estimate. However, I do feel that it is a conservative estimate, if the wall events have been computed correctly.

I. Calculation of the Breakup Capture Rate in He^3

The calculation of the capture rates for the breakup reaction

$$\mu^- + He^3 \rightarrow d + n + \nu \tag{4}$$

$$\mu^- + He^3 \rightarrow p + 2n + \nu \tag{5}$$

proceeds similarly to the He^4 calculation. However, there are two additional complications with the He^3 calculation: (a) even a greater portion of the low energy spectrum is masked since the triton peak covers the spectrum from $\approx$ 1 to 3 MeV, and (b) the branching ratio between the proton and deuteron reactions above is unknown experimentally. Yano has calculated the rates for each of the reactions and obtained a theoretical branching ratio of $\approx$ 3 deuterons to 1 proton.[15] Messiah[79] has calculated rates for similar pion-capture reactions

$$\pi^- + He^3 \rightarrow d + n + \gamma$$
$$\rightarrow p + 2n + \gamma \tag{73}$$

and obtains a branching ratio of $\approx$ 4 to 1. For the purpose of analysis in this experiment, I used a branching ratio of 3.5 to 1. Since the protons leave little energy in the gas, the energy region less than $\approx$ 1 MeV is most sensitive to them. Unfortunately, this is just the energy region masked by the electron background. Thus the data can not determine this branching ratio. An experiment without the electron background could conceivably give some information on the branching ratio.

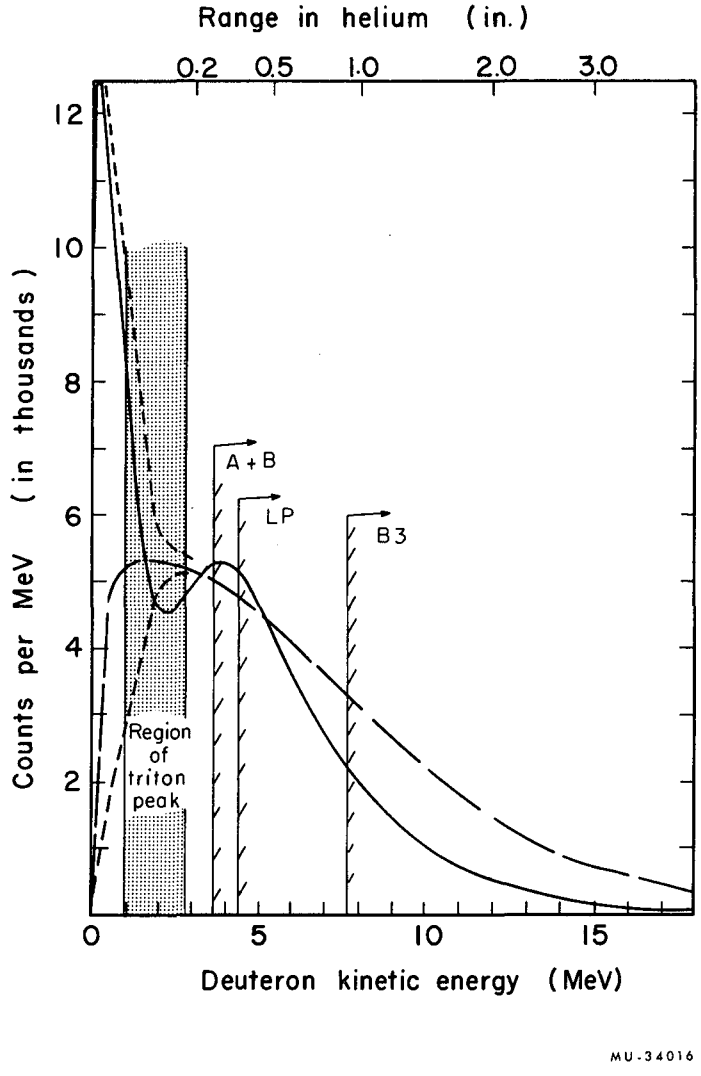

Fig. 29. Theoretical deuteron-energy distributions for the reaction $\mu^- + He^3 \rightarrow d + n + \nu$. The solid curve is derived from Yano's spectrum and the dashed from Bietti's. The top scale gives the ranges of a deuteron in helium at 28.9 atm. The shaded area indicates the region masked by the 1.9-MeV triton recoil peak, and the cuts indicate the upper limit of the observed counts for runs B3, A+B, and LP. The dashed lines indicate the estimated upper and lower limits of the deuteron spectrum in the region below $\approx$ 3 MeV.

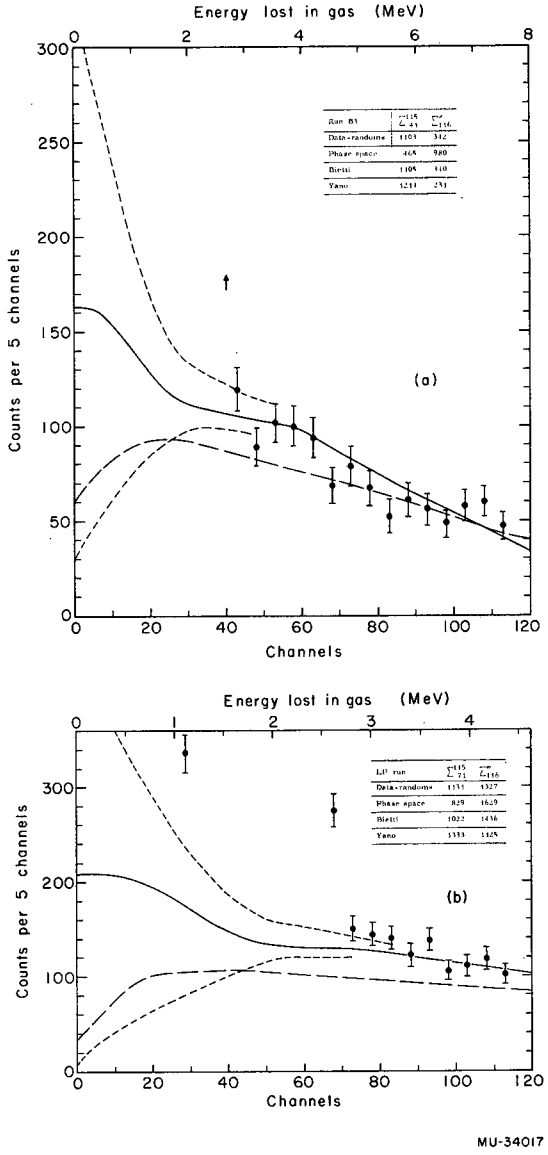

Fig. 30. Breakup capture events in He^3. (a) B3, (b) LP. The data points are with randoms subtracted and are summed over every five channels. The dashed lines are the normalized spectrum derived from a phase-space distribution; the solid line is the spectrum derived from an average of Yano's and Bietti's distribution; the dotted lines indicate roughly the effect of varying the counts below ≈ 3 MeV by 50%.

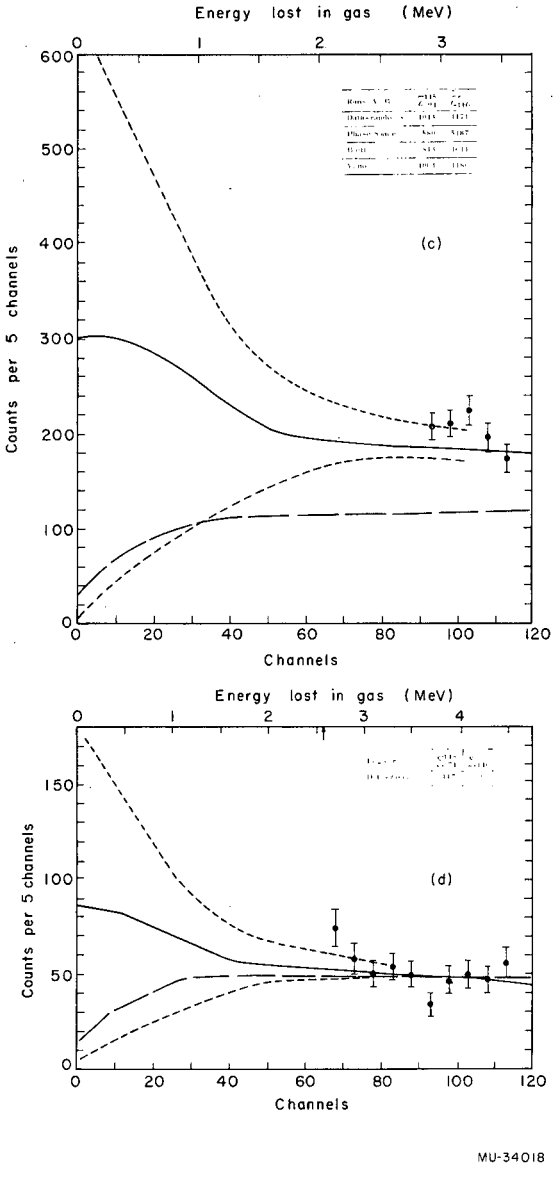

Fig. 30. (c) A+B, (d) logic. Explanation same as for (a) and (b).

Yano has also computed the energy distribution of the deuteron in Reaction (4) in the c.m. system of the three nucleons.[80] Using his numbers, I have calculated the deuteron spectrum expected in the laboratory system. This is shown in Fig. 29 and for convenience is called the Yano spectrum. The minimum in the spectrum at ≈ 2 MeV arises from a fortuitous combination of factors in transforming from the c.m. to the lab system and would be interesting to observe experimentally. Unfortunately neither statistics nor the energy resolution allows this in our case. If allowance is made for the deuteron-triton mass difference, Bietti's spectrum for muon capture in He^4 can be applied to the He^3 case. This shape is also shown in Fig. 29. Note that the shapes differ considerably below ≈ 1 MeV, but are similar in the observable region above the triton peak. As far as the experimental data are concerned, one shape is as good as the other and an average of the two was taken to compute the "unobserved" events below ≈ 3 MeV.

There are no theoretical calculations of the proton spectrum in Reaction (5), but it is expected to be similar to the deuteron spectrum after the differing masses are taken into account. Thus each of the above-mentioned spectra was fed into the Monte Carlo program (with the 3.5 to 1 deuteron-to-proton branching ratio) and the various veto on, veto off, HP, and LP spectra obtained, with results similar to Fig. 25. Each spectrum was then normalized to the observed number of counts above ≈ 3 MeV for each appropriate run. In the logic run alone, only the counts between channels 70 and 115 were used to normalize the spectra, since the number of counts above channel 115 were not measured in this case; consequently the counts above channel 115 were determined from the theoretical shapes. The data with the normalized average of Yano's and Bietti's spectra are shown in Fig. 30 (a) through (d). As in the He^4 graphs, the box encloses the sum of the observed counts in each region of the spectrum, and the dashed line shows a normalized spectrum, plotted with the assumption that the proton and deuteron each follow a simple phase-space distribution. Because of poor statistics and the finite region of observation,

the data can not ascertain whether the Yano spectrum or the Bietti spectrum is a better fit; however, the grossly different phase-space distribution can again be ruled out. Neither the Bietti nor Yano spectrum fits perfectly in all respects so that probably different shapes are to be expected for the true spectrum. Other distributions and other branching ratios were also considered without any theoretical basis, but the data is not sensitive to small changes in the spectra shape. Thus a more precise determination of the spectra shape must await a better experiment and one with better statistics.

As in the He^4 case, the theoretical-spectra shapes were used to determine the number of counts below ≈ 3 MeV. However these counts are even more uncertain than in the He^4 case, since an even larger energy region is masked by other events. These "unobserved" counts, an average of Yano's and Bietti's spectrum, are listed on line 4 of Table VI. The dotted lines in Figs. 29 and 30 (a) through (d) show the effect of varying the unobserved counts by 50%. The Yano and Bietti spectra were used as guides in determining the upper (Yano) and lower (Bietti) limits of the spectra, and it is believed that the true spectrum lies somewhere between these limits. Again it is emphasized that there are no experimental data for this part of the spectra so that these error limits can only be considered as best estimates. Considering, however, the shapes shown in Fig. 29 and the reasonable fit above ≈ 3 MeV, these error limits can be considered conservative.

By adding the observed and unobserved events for each run in Table VI, correcting for the number of breakup events that veto themselves, correcting for the finite TR time gate, and dividing by the number of stopped muons, one obtains the total number of events per S_μ. From the proportionality,

$$\frac{\Lambda_B}{\Lambda_T} = \frac{\text{events}}{S_\mu} \tag{74}$$

where $\Lambda_T = \Lambda_C + \Lambda_B + \Lambda_D$ is the total-muon-disappearance rate, Λ_B is the breakup capture rate, Λ_C is the $He^3 \rightarrow H^3$ capture rate ($\approx 1500\ sec^{-1}$) and Λ_D is free-muon-decay rate = $4.5454 \times 10^5\ sec^{-1}$, one obtains $\Lambda_B = 4.56 \times 10^5$(events/$S_\mu$-events). The breakup capture rates for each run are shown on line 9 of Table VI. The weighted average of the four runs is

$$\Lambda_B = 700 \pm 180\ sec^{-1}, \tag{75}$$

where again the error is mostly from the uncertainty in the "unobserved" events. Note, however, that the low-pressure run gives a high Λ_B well outside the statistical errors (but not outside the error quoted, which is due to the systematic uncertainty of the unobserved events). This discrepancy is disturbing, for it would indicate a systematic error in all the breakup results. It is discussed further in Sec. IV. J.

J. Low-Pressure Discrepancy

It can be argued that the serious discrepancy of the LP-breakup-capture rate arises from wrong assumptions concerning the "unobserved" events. To test this argument I first show that the observed events above 3 MeV also show this discrepancy. If I calculate the uncorrected observed breakup counts per stopped muon, I obtain $5.97 \pm 0.24 \times 10^{-4}$ for the LP data and $5.83 \pm 0.24 \times 10^{-4}$ for run A + B (the HP data). Although the two ratios are within the possible error, the LP is nonetheless larger than the HP. It should be considerably less than the HP counts, for not only should more counts be vetoed at LP, but also any given breakup product will in general leave less energy in the gas at the lower pressure. Thus irrespective of the unobserved events, the LP and the HP data do not agree.

Since the dead layer effectively stops about twice as many muons at LP than at HP, one would naturally guess first that the extra events in the LP data come from muon captures in the wall surrounding the helium gas. However, because the detection of neutral particles also is proportional to the pressure, the number of wall events from neutral particles is relatively independent of the pressure. Furthermore, as discussed in Sec. IV. G, the wall events from neutral particles are a relatively small fraction of the total observed counts and could not account for the LP discrepancy. On the other hand, if charged particles--protons and alphas--constitute a large fraction of the wall-capture products, the wall events are proportional to the relative dead-layer thickness or inversely proportional to the pressure. Assuming that the capture rates listed in Table VI can be divided between the true helium breakup capture rate Λ_B and a wall-capture rate $\Lambda_W = k/P$ (P is the gas pressure), one can calculate Λ_B. If $\Lambda_H = 675\ \text{sec}^{-1}$ is the observed capture rate at high pressure and $\Lambda_L = 910\ \text{sec}^{-1}$ at low pressure, then one can write

$$\begin{aligned} \Lambda_H &= \Lambda_B + k/P_H \\ \Lambda_L &= \Lambda_L + k/P_L \,. \end{aligned} \tag{76}$$

So that

$$\Lambda_W(HP) = \frac{k}{P_H} = \frac{\Lambda_H - \Lambda_L}{P_H/P_L - 1} = 275 \text{ sec}^{-1} \quad (77)$$

and

$$\Lambda_B = \Lambda_H - \Lambda_W(HP) = 675 - 275 = 400 \text{ sec}^{-1}. \quad (78)$$

Furthermore, the He^4 runs (done at HP) must also be corrected for the wall events so that

$$\Lambda(He^4, \text{ corr.}) = \Lambda(He^4, \text{ obs.}) - \Lambda_W(HP) = 100 \text{ sec}^{-1}. \quad (79)$$

If the above calculation is to be believed, this means that 40% of the HP He^3 breakup events arise from muon-capture events in the walls. This also implies that charged particles come from wall captures 19% of the time. To my knowledge the fraction of charged particles coming from muon capture in Mg, O, C, and Al has not been measured, but it is not inconceivable that $\approx$ 19% of the products are charged. However, in an emulsion study only 2.5% of the products were charged;[72] thus offhand one would tend to disbelieve such a large fraction.

Another likely explanation for the discrepancy is that the calculation of the unobserved events and fraction of vetoed breakup events is grossly incorrect. It is possible that some weird combination of deuteron and proton spectra could bring the LP capture rate in line with the HP capture rates. For example, if the phase-space deuteron- and proton-energy distributions are used, the fraction of vetoed events doubles and the HP-LP discrepancy in the capture rates becomes even greater. Perhaps this explanation, in combination with a statistical fluctuation, is the reason for the discrepancy.

A third explanation that would completely eliminate any discrepancy would be if the $\bar{5}$ veto going to TR were really off during the LP run. There was every intention of having the veto on during

the LP run, but through some blunder a cable could have been disconnected and the veto could have been off. This veto has little effect other than the ≈ 25% reduction of breakup events, so there is no a posteriori way to determine if the veto were really on or off. If the veto were off, however, then there is no correction for vetoed events in the computation of Sec. IV. I, and the breakup capture rate becomes 660 sec^{-1}, which is in excellent agreement with other data listed in Table VI.

Neglecting blunders, one must conclude that the breakup capture rates have not been measured with as great an accuracy as given in Secs. IV. H and I. The LP discrepancy is probably due to a combination of charged capture products and incorrectly assumed energy distributions. With the present information it is not possible to calculate further either of these factors. Thus one must conclude that the capture rates given in Secs. IV. H and I are upper limits. The lower limits are difficult to assign but are probably within the rough calculation done above. Thus, if the LP breakup data is not used, and the breakup capture rate is averaged over the remaining three runs in Table VI, one obtains

$$\Lambda_B = 665^{+170}_{-430}\ sec^{-1}. \tag{80}$$

For the He^4 runs we have

$$\Lambda(He^4) = 375^{+30}_{-300}\ sec^{-1}. \tag{81}$$

K. Triton-Recoil Edge Correction

Luckily the LP discrepancy does not appreciably affect the $He^3 \rightarrow H^3$ capture rate. However, one other correction--the triton recoil-edge correction--must be discussed before the $He^3 \rightarrow H^3$ capture rate can be calculated.

Some muons will stop near the edge of the helium gas near the cup counter; if they are captured, their triton recoil could lose most of its energy in the wall materials and not give enough light in the

helium to be detected by pulse-height analysis. One must correct the observed number of triton recoils for this effect. The correction depends on how many muons stop close to the walls, i.e., the distribution of stopping muons, the range of tritons in the gas, and the amount of energy left in the gas. If the triton recoil barely touches the wall, it will still be detected since it will leave enough energy in the helium to appear under the triton peak on the pulse-height spectra. On the other hand, if the triton leaves only ≈ 0.5 MeV in the gas, it certainly will not be counted in the pulse-height spectra. The energy at which a triton has a 50% chance of being counted depends on the energy resolution of the He counter. Table VII lists the energies at which one would expect the triton to have a 10%, 50%, and a 90% chance of being observed in the pulse-height spectra. For each of these triton energies, the distance the triton must travel in the helium to deposit that energy is also given. These ranges are calculated by integrating the stopping power of helium as a function of energy[81] over the energy of interest. Integrating the stopping power from 0 to 1.9 MeV gives a triton range of 1.75 ± 0.1 mm in helium at 28.9 atm. This checks well with the triton ranges observed in a helium-diffusion chamber[16] of 2.37 ± 0.02 mg/cm^2 or 1.78 ± 0.02 mm at 28.9 atm.

Table VII. Triton-recoil-edge correction.

1. Energy left in gas (MeV)	0.77	1.19	1.65	1.90
2. Probability of seeing triton recoil(%)	<10	≈50	>90	100
3. Recoil range in helium at 28.9 atm (mm)	0.92	1.29	1.57	1.75±.10
4. Percentage of recoils lost (28.9 atm)	0.66	0.93	1.13	
(15.4 atm)	1.22	1.73	2.07	

Assuming an isotropic angular distribution, and taking the distribution of stopping muons into account, the Monte Carlo program (Appendix D) then calculated how many tritons would be lost in the wall. The results, given as a percentage of all triton recoils, are in Table VII for both pressures at which data were taken. Taking the central values as the correction with errors given by the 10/90% limit, the observed triton recoils must then be corrected by 0.9±0.3% at the higher pressure and by 1.7±0.5% at the lower pressure. The correction at the lower pressure is larger since the tritons travel further at the lower pressure and more have a chance of hitting the wall.

One complicating factor affects this correction. Some of the helium gas permeates the MgO powder that coats the walls of the cup counter, so that a muon capture occurring in this gas has an even smaller chance of being detected. This effect was not taken into account in the above corrections. How much helium permeates the MgO is difficult to determine, but the rough calculation given below shows that this effect is probably negligible. The thickness of the MgO layer was ≈ 0.1 mm. The number of muons stopping in a 0.1-mm layer of helium at the edge of the gas can be calculated with the knowledge of the stopping-muon distribution; it is ≈ 0.3% of all the stopped muons. Thus, at most, 0.3% of the muons are affected, and some of these could still give an observable-triton recoil. This fraction is small and within the uncertainty of the over-all edge correction and therefore this effect is neglected.

L. Calculation of the $He^3 \rightarrow H^3$ Capture Rate

The major goal of this experiment was the measurement of the muon-capture rate, Λ_C, in the reaction

$$\mu^- + He^3 \rightarrow H^3 + \nu . \qquad (3)$$

Its calculation is now discussed. First, all the backgrounds were subtracted from the basic pulse-height spectra of Fig. 21(a) through (e). The random and electron subtractions are discussed in

Secs. IV. D and E, respectively. The breakup background was subtracted by use of the solid curves in Figs. 30(a) through (d), with errors shown by the dotted lines. This procedure was discussed in Section IV. I. Finally the remaining counts were added to give the observed triton-recoil events shown on line 2 of Table VIII. The errors contributed by each source are listed on line 3 of Table VIII. Uncertainties in determining the outer wings of the triton peak are included in these errors (mostly under electron background) or are negligible.

These observed triton-recoil events must then be corrected for the number lost in the walls (discussed in Sec. IV. K) and for the finite TR time gate (Sec. III. F. 4). In addition, the logic-run data must be corrected for good TR events that are vetoed by the μ-e logic system (see Sec. III. F. 8). The total correction factor applied in each case is listed on line 4 of Table VIII; the corrected number of triton recoil counts is shown in line 5. Again the capture rate is computed from the proportionality

$$\frac{\Lambda_C}{\Lambda_T} = \frac{T}{S\mu} \tag{82}$$

where the total-muon-disappearance rate is $\Lambda_T = \Lambda_B + \Lambda_C + \Lambda_D$, $\Lambda_D = 4.545 \times 10^5$ sec^{-1} is the free-muon-disappearance rate, and the breakup capture rate is $\Lambda_B \approx 700 \pm 180$ sec^{-1}. Solving for Λ_C, one obtains

$$\Lambda_C = (\Lambda_B + \Lambda_D)\left[\frac{T}{S\mu - T}\right] = \left[\frac{T}{S\mu - T}\right] \times (4553 \pm 4) \times 10^3 \text{ sec}^{-1}. \tag{83}$$

The capture rates obtained for each run are listed on line 8 of Table VIII. Errors from each source are treated independently for each run. Weighting each result by the inverse square of its errors gives an average capture rate for the five runs of

$$\Lambda_C = 1505 \pm 46 \text{ sec}^{-1}. \tag{84}$$

Table VIII. Triton-recoil events.

1.	Run designation	A	B	LP	Logic	B3
2.	Counts in triton-recoil peak	11760±400	14030±480	10600±310	5860±270	5290±200
3.	Uncertainties contributing to error					
	a. Statistical	±110	±120	±100	±77	±73
	b. Random background	±125	±180	±100	± 5	±50
	c. Electron background	±200	±260	± 60	±200	±100
	d. Breakup background	±300	±340	±270	±170	±150
4.	Correction factor	1.1760±.0054	1.1760±.0054	1.1853±.0071	1.223±.013	1.1760±.0054
5.	Corrected triton-recoil counts	13830±470	16500±570	12570±380	7160±340	6220±240
6.	Corrected number of stopped muons (in thousands)	4144±18	4985±21	3758±36	2196±10	1952±9
7.	Triton recoils per stopped muon (in thousandths)	3.338	3.310	3.345	3.262	3.187
8.	Capture rate (sec^{-1})	1525±53	1512±53	1528±49	1490±72	1456±56

The error in this averaged result arises mostly from the uncertainty in the breakup backgrounds and is obtained by dividing the error for each run into a systematic and a random part. The random part, consisting of lines 3a, b, and c in Table VIII, is then treated independently for each run. There is excellent statistical agreement among the five runs, because the χ^2 (with only the random part of the error used) is 3.33. This χ^2 has a 50% chance of occurrence.

V. RESULTS AND CONCLUSIONS

This muon-capture experiment yields the capture rates in He^3 and He^4. The final results are listed in Table IX. The breakup capture rate in He^3

$$\Lambda_B(He^3) = 665^{+170}_{-430}\ sec^{-1} \tag{80}$$

is combined with the $He^3 \rightarrow H^3$ partial rate

$$\Lambda_C(He^3 \rightarrow H^3) = 1505 \pm 46\ sec^{-1} \tag{84}$$

to give a total-muon-capture rate in He^3 of

$$\Lambda(He^3,\ total) = 2170^{+170}_{-430}\ sec^{-1}. \tag{85}$$

The total-capture rate in He^4 is measured to be

$$\Lambda(He^4) = 375^{+30}_{-300}\ sec^{-1}. \tag{81}$$

Note the large isotope effect. The large lower limits for the He^3 breakup rate and the He^4 total rate signify the possibility that some of the events may have been from muon captures in the wall surrounding the gas. The error in the $He^3 \rightarrow H^3$ rate is almost entirely due to the uncertainties in the breakup capture events. All of the errors could be reduced in a new experiment that used the same methods as this experiment. Several suggested improvements are listed in Appendix E. In principle, this type of experiment is an excellent measure of muon capture rates in helium and is capable of giving very accurate results.

Also shown in Table IX are all other known experimental measurements and theoretical predictions for the muon-capture rates in He^3 and He^4. The He^4 capture rate agrees with the two recent measurements of Block[21] and Bizzarri[20] if the wall events are small. Theoretical predictions of the He^4 capture rate range within our experimental limits, with recent predictions tending toward a lower rate. Similarly the total He^3 capture rate is in excellent agreement with a previous measurement by Falomkin et al.,[16] who used a helium-diffusion chamber. The old theoretical prediction by Primakoff[42]

Table IX. Summary of muon-capture rates (in sec^{-1}) in He^3 and He^4.

Authors	$He^3 \rightarrow H^3$	Total He^3	Total He^4	Comments
Experimental				
This experiment	1505±46	2170^{+170}_{-430}	375^{+30}_{-300}	He scintillation
Falomkin et al.[16]	1410±140	2140±180		He diffusion chamber
Edelstein et al.[18]	1450±75			He + Xe scintillation
Bizzarri et al.[20]			450±90	Liquid He bubble chamber
Block et al.[21]			368±47	Liquid He bubble chamber
Anderson et al.[82]			1300	? ?
Theoretical				
Primakoff[42]		2500±250	470±70	Closure approx
Fujii, Yamaguchi[23]	1540±80			"Trion" wave function
Yano[15]	1460	670±30[a]		$g_P = 7\, g_A$
Goulard, Primakoff[84]		2360±240	324±60	Closure and relativity $g_P = 8\, g_A$
Fujii, Primakoff[36]	1460±150			
Werntz[43]	1560±80			
Wolfenstein[44]	1400→1500			
Fujii[45]	1660			Hard-core wave function
Duck[46]	1250			Shell-model wave function
Caine, Jones[78]			345±110	Explicit sum over states
Bietti[83]			310	
Bietti, DiPorto[75]			120→220	

a. Breakup rate only.

agrees reasonably well with the measured total capture rate; Yano's recent and more detailed calculation of the breakup capture rates[15] is in excellent agreement with the observed value. In the future, the detailed shape of the breakup energy spectra may be of considerable interest, much as the β-energy spectra were important in β decay.

Although our measurement of the $He^3 \rightarrow H^3$ capture rate is the highest of the three experiments performed so far, it does not disagree with the other results. Except for the calculations of Duck and Fujii[45, 46] (see also Ref. 15) the theoretical predictions are in agreement with our result. Because of ambiguities in the He^3 rms radius, obtained from electron-scattering experiments, the theoretical predictions of the $He^3 \rightarrow H^3$ capture rate are uncertain to within 10% and this accounts for most of the scattering in the results of the theoretical calculations.

If the experimental value of the $He^3 \rightarrow H^3$ capture rate is substituted into $\Lambda_C = 1/4\,\Lambda_s + 3/4\Lambda_t$ (Λ_s and Λ_t are given by Eqs. 34 and 35, with S=T=0), one obtains a relation between the two most uncertain parameters in muon capture--P and A. Figure 31 is a plot showing this relation. Any values of P and A within the shaded area would be consistent with this experiment. The vertical lines indicate possible choices of $A(q^2)$. Since the axial-vector and the weak-magnetism terms in the Hamiltonian reduce to the same form in the nonrelativistic limit, band I with $A(q^2)/A(0) = M(q^2)/M(0)$ is to be preferred over band II. Actually the value of $A(q^2)$ is very uncertain and could range from +0.9 to +1.15. This uncertainty in A reflects the uncertain state of the nuclear physics of the trion. The preferred theoretical value of $g_P = P(q^2)m_\mu/m_p$ for the nucleon is presently the $6.6\,A_\beta$ obtained originally by Goldberger and Treiman.[25] This is the horizontal line in Fig. 31. Note that g_P (trion) $\approx -3\, g_P$(nucleon). The intersection of $g_P = 6.6A_\beta$ with band I is in good agreement with the experimental capture rate. However, Eq. 35 is quadratic in P and has a minimum in the region of interest. Thus, with the inclusion of the uncertainties in $A(q^2)$ any value of g_P between 0 and $+25\,A_\beta$

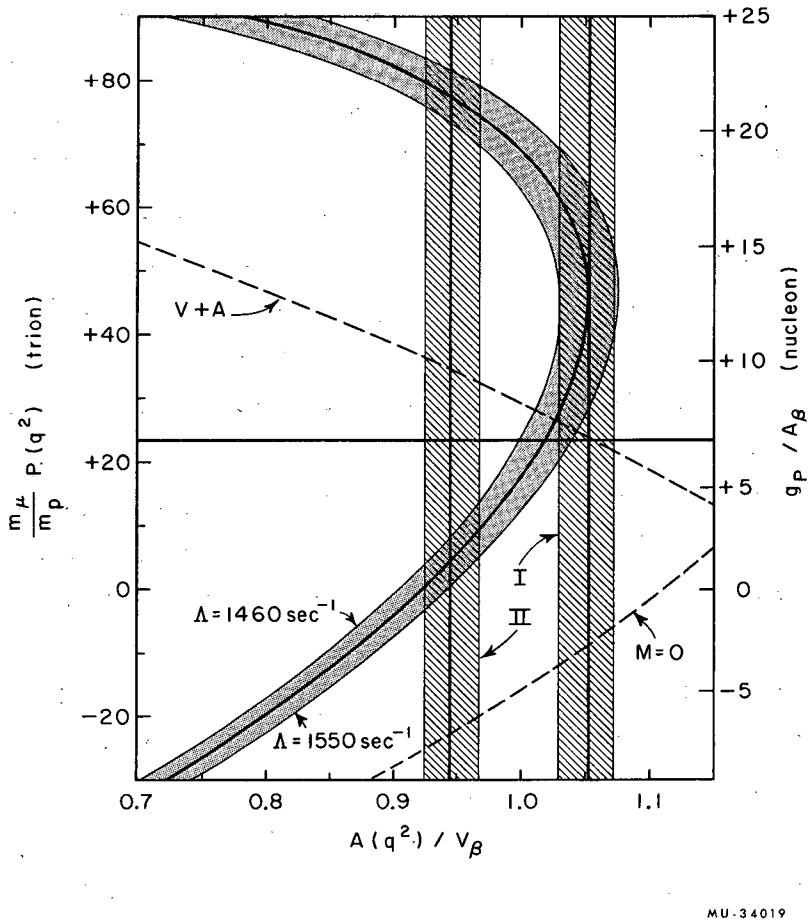

Fig. 31. The $He^3 \rightarrow H^3$ capture rate with the axial-vector coupling constant and the induced pseudoscalar coupling constant as independent variables. The shaded area indicates the region consistent with the present experiment. The theoretical preferences are indicated by the vertical and horizontal lines. Band I is with $A(q^2)/A(0) = M(q^2)/M(0)$ and band II with $A(q^2)/A(0) = V(q^2)/V(0)$. The width of each vertical band reflects the uncertainty in A(0). The dashed lines are for a V+A weak-interaction theory and for a theory with the weak-magnetism term equal to zero.

is allowed. Several recent experiments have indicated a value of g_P closer to 15 A_β.[37, 38] This would indicate that band I is correct. A graph similar to Fig. 31 is given by Rothberg et al. for muon capture in hydrogen.[13] A value of $g_P = 15\ A_\beta$ would bring their result in good agreement with theory.

This experiment does not rule out the possibility of a (V + A) interaction in muon capture. If A is a negative quantity in Eqs. 34 and 35, then for a capture rate of 1505 sec^{-1} one obtains the dashed curve in Fig. 31. Note that it too is consistent with $g_P = +6.6\ A_\beta$ and band I. This must be a chance combination of numbers. Muon capture in hydrogen has established a V-A theory.[11]

One must conclude that at the present time, because of the uncertainties in P and A, the quantitative predictions of the UFI in muon capture have only about 10% accuracy. However, the excellent agreement between the theoretical and experimental values of the capture rates in helium lends considerable support to the hypotheses of a universal Fermi interaction and a conserved vector current.

ACKNOWLEDGMENTS

This experiment was performed in collaboration with Leonard Auerbach, Roger Hill, David Jenkins, Joseph Lach, and Norman Lipman. I am deeply indebted for their long hours of creative work.

The success of the experiment is due to Norman Lipman, who conceived the target design and the electronics logic. He invariably saw the problems and difficulties in the experiment and was quick to suggest their correct solution. I greatly appreciate his advice and encouragement.

The support of Professors Emilio Segrè and Owen Chamberlain and numerous helpful discussions both with them and with other members of the group, in particular Norman Booth, Herb Steiner, Clyde Wiegand, Willy Chinowsky, and Gilbert Shapiro, are gratefully acknowledged. I especially wish to thank Professor Segrè who served as my thesis advisor.

To mention all the people whose effort went into this experiment would take many pages. Special thanks go to the crew of the 184-inch synchrocylotron for supplying an excellent beam, to the accelerator technicians for their help in setting up the apparatus, to the Hydrogen Target Engineering Group under Ed Mc Laughlin for designing the special He^3 target, to the Hydrogen Target Test Group under Rene Bolaert for testing the target, to the Building 25 Acc. Techs for their skilled craftsmanship, to the counting equipment group for their willing assistance, to Art Bierke and Tom Nunamaker for their help with their fast coincidence circuit, to Walter Barkas for supplying the emulsions and to Lillian Zapata for scanning them, to Joe Good for his help with the computer programs, to Bill Tivol for his help in the early stages of the experiment, to Doris Heyneman and Pat Brown for assisting in numerous tasks, and finally to my wife, Joan, for her patience and encouragement.

Special credit must go to Dick Schafer, Bill Pope, and Ray Fuzesy whose perseverance beyond the call of duty made the leak-proof He^3 target possible.

This work was done under the auspices of the U. S. Atomic Energy Commission.

APPENDICES

A. Mass of the Muon Neutrino

In principle this experiment allows a mass determination of the neutrino in the reaction

$$\mu^- + He^3 \rightarrow H^3 + \nu \ . \qquad (3)$$

In practice, because of the large energy that the neutrino carries away (103.2 MeV), the accuracy of such a mass determination is quite limited. However, the mass of the muon neutrino now has an experimental upper limit as large as 3.5 MeV[85] and it seems worthwhile to examine the question to see what limits this experiment puts on the neutrino's mass.

I first derive an expression for the neutrino's mass in terms of the observed triton-recoil energy. If the initial energy in Eq. (3) is $E_i = m_\mu + m_{He} - B$, then the final energy is $E_f = E_\nu + E_t = E_\nu + m_t + T$ and $E_\nu = Q-T$; in these equations B is the atomic binding energy of the muon in its s-state orbit, T is the kinetic energy of the triton, and Q is $m_\mu + m_{He} - m_t - B$.

Since the momentum of neutrino is equal to that of the triton recoil, we have $P_\nu^2 = P_t^2 = E_t^2 - m_t^2 = T^2 + 2m_tT$. Finally, the mass of the neutrino is given by

$$m_\nu^2 = E_\nu^2 - P_\nu^2 = (Q - T)^2 - T^2 - 2m_tT = Q^2 - 2T(Q + m_t) \ . \qquad (86)$$

The mass difference between the He^3 nucleus and the triton is known very accurately and is $m_{He} - m_t = 529.1 \pm 0.4$ keV ;[30] the triton mass is 2808.76 ± 0.03 MeV. From the g-2 experiment,[86] the muon's mass was determined to be 105 653.5±2.0 keV. Since B is easily

calculated to be 11.252 keV, $Q = 105\ 113 \pm 2$ keV . The measured value of the triton-recoil's energy contributes the largest uncertainty in this calculation and this is mainly because of the uncertainty of the energy calibration (see Sec. III.C.4). The 5.45-MeV alpha calibration is most suspect since the alpha is doubly charged and comes from a finite (and light-absorbing) source. Using the low-pressure data, the neutron absorption and the alpha source for energy calibrations, we obtain $T = 1.85 \pm 0.08$ MeV where the error is conservative and arises from the uncertainty in the alpha calibration. (If the alpha calibration were not suspect, the error would reduce to ±0.03 MeV). The neutrino's mass is then less than 25 MeV with 90% confidence. Even if one were to assume that T could be measured with no error, the mass errors would allow only a determination that $m_\nu < 0.7$ MeV . Essentially these high upper limits arise because one must subtract two large numbers in Eq. (86) to get zero. Thus it does not appear that this experiment would ever be useful in a neutrino-mass determination.

By setting $m_\nu = 0$ in Eq. (86) one can solve for the expected triton-recoil energy:

$$T = \frac{Q^2}{2(Q+m_t)} = 1.8959 \pm 0.0001 \text{ MeV} \qquad (87)$$

B. Target Details and Procedures

Since we used about $20 000.00 worth (145 liters at STP) of He^3, and since the supply of He^3 was limited, an elaborate system was developed to ensure that the gas was not lost or contaminated. The plumbing system is shown schematically in Fig. 32 and a photograph of the plumbing control panel is shown in Fig. 33. The main vacuum tank (MVT) surrounded the target and contained three phototubes and their bases. Consequently, the MVT pressure had to be kept low to prevent discharge from the phototube bases. With 3000 volts on a phototube, sparking occurred at pressures above about 35 μ . During the experiment the MVT pressure was kept below 1 μ . . This low pressure was also necessary to keep any water vapor from condensing on the light guides and thus spoiling their optical-reflection properties. After the experiment the target pressure gauge was calibrated against a standard gauge and found to be about 30 psi in error. All pressures in this report have been corrected for this; however, the gauge is still only accurate to about ± 5 psi.

The problem of making a leaktight seal between Lucite and stainless steel at liquid nitrogen temperatures and pressures up to 600 psi had not been solved to our knowledge. After many tests, the design that worked is shown roughly in Fig. 4.[87] The seal is basically a shaped Kel-F O-ring bearing against specially shaped surfaces. All the contacting surfaces were painstakingly polished as the most minute scratch made possible a large leak. Unfortunately, the windows ruptured easily under the strains of temperature and pressure, so that

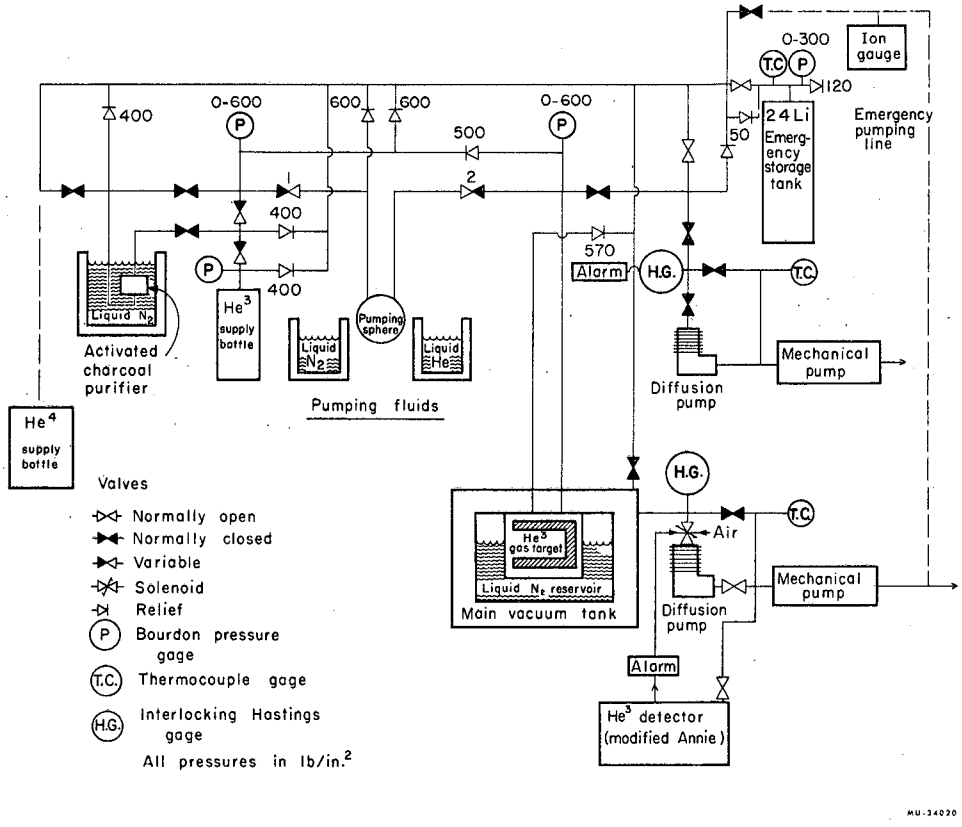

Fig. 32. Schematic of the closed-circuit plumbing system showing the cryogenic pump, carbon purifier, and safety details. All pressure-relief valves open into the emergency storage tank.

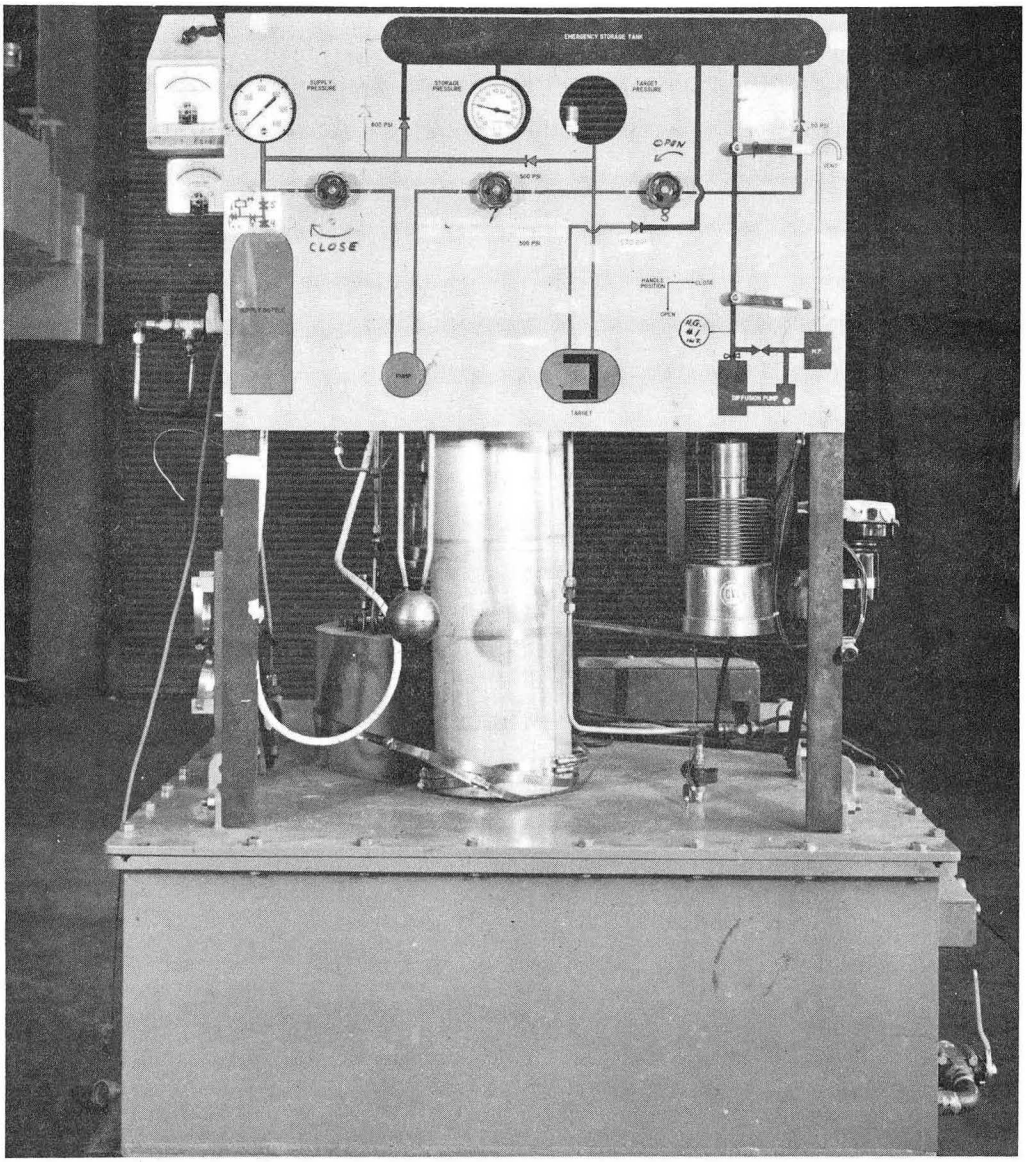

ZN-4240

Fig. 33. Side view of target showing the plumbing-control panel and MVT. The pumping sphere, emergency storage tank, and panel diffusion pump can also be seen.

precautions had to be taken to recover the gas if a window broke. This was done by attaching a helium leak detector to the MVT surrounding the target. If any helium were detected, a solenoid valve leading to the vacuum pumps rapidly closed, thus trapping most of the gas in the MVT for later return to the supply bottle. Luckily neither window broke during the experiment and more than 95% of the He^3 was recovered in the original supply bottle; about half of the rest was recovered in the emergency storage tank. Most of the remaining gas was lost because the last bit of gas could not be pumped from the pumping sphere itself. The final leak rate through the window seal was about 2 cc/month at 450 psi and the loss through plumbing joints was perhaps a hundred times this. Thus, the amount of gas lost through leaks was negligible.

The procedure used in preparing the target and transferring the He^3 from the supply bottle is as follows:

1. The system was evacuated and tested for leaks by means of a helium-leak detector and an ion gauge that could be attached temporarily at the emergency pumping line. This ion gauge was useful in measuring low pressures and small pressure differences, provided that it was well outgassed.

2. About 2 atmospheres of He^4 was then put in the target and cooling of the target begun. To avoid straining and fracturing the thick Lucite windows, the cooling took place slowly over a 10-hour period. Thermocouples located at seven spots on the target monitored the rate of cooling so that large temperature differentials could be avoided. Once the target was cold, an automatic-fill system kept the

liquid nitrogen reservoir full. Final temperatures on the outside surfaces of the target ranged from -120°C to -190°C, depending on how far the thermocouple was from the liquid nitrogen reservoir. The phototubes, cooled by conduction, operated at about 0°C .

3. With purified He^4 , the target was then tested at pressures up to 600 psi.

4. With a heating tape and a Variac to control the current, the activated charcoal purifier was baked at a temperature of 700°F (measured by a thermocouple). Exceeding this temperature had disastrous consequences as the hard solder that holds the purifier together melts at about 1200°F.

5. The entire plumbing system was evacuated to a pressure of about 1 μ, after an additional check for leaks.

6. The vacuum pumps were then isolated from the system and the He^3 allowed to pass <u>slowly</u> and adiabatically through the liquid-nitrogen-cooled purifier into the pumping sphere and target.

7. When equilibrium was reached, valve 2 (see Fig. 32) was closed, and the pumping sphere cooled, first with liquid nitrogen, and then with liquid helium contained in an open dewar surrounding the sphere. This brought most of the gas remaining in the supply bottle into the pumping sphere, because the He^3 liquified in the pumping sphere due to the higher pressure inside.

8. Valve 1 was then closed, valve 2 opened, and the sphere allowed to warm to room temperature, thus transferring most of the gas to the target.

9. To empty the target, the gas was pumped in the other direction in a similar manner.

10. The target was warmed by blowing first hot dry nitrogen and then hot dry air through the liquid nitrogen reservoir. During the runs with xenon in the target, the warmup was halted and a steady temperature of about -70°C was maintained. Care had to be taken not to go below this since xenon gas condenses at -107°C at atmospheric pressure.

C. The TR Time-Gate Measurement

In this experiment it was necessary to know the lengths of several pulses with some degree of accuracy. In particular, the circuit Sμ generated a pulse that determined the time during which the coincidence TR could register a triton-recoil. A schematic of the circuit developed to measure the length of a time gate is shown in Fig. 34. The discriminators, amplifiers, Sμ , and TR are the same circuits used in the experiment so that the pulse shapes to be measured are the same as those generated during data-collection. A variable-frequency nanosecond pulse generator[60] supplied a train of He-simulating pulses going into TR ; every tenth pulse triggered Sμ . The time gate to be measured was then generated by Sμ and fed into TR in coincidence with the simulated He pulses. As seen in Fig. 34, pulse (1) represents a He pulse coming at the beginning of the Sμ gate and (2) represents a He pulse coming at the end of the Sμ gate. By measuring the frequency of the He pulses with a frequency meter (Hewlett Packard 524A, accurate to 1 ppm), the period between (1) and (2), and hence the Sμ gate length, can be found.

The method of making this measurement follows. The He-Sμ relative delay is adjusted so that pulse (1) counts with half efficiency in TR . Since (1) is also the trigger for Sμ , this delay will be kept constant, independent of the frequency of the pulse generator. Next the frequency is varied so that pulse (2) also counts in TR with half efficiency. The period of the He pulses is then equal to the time during which He pulses can count in TR . Note that this method

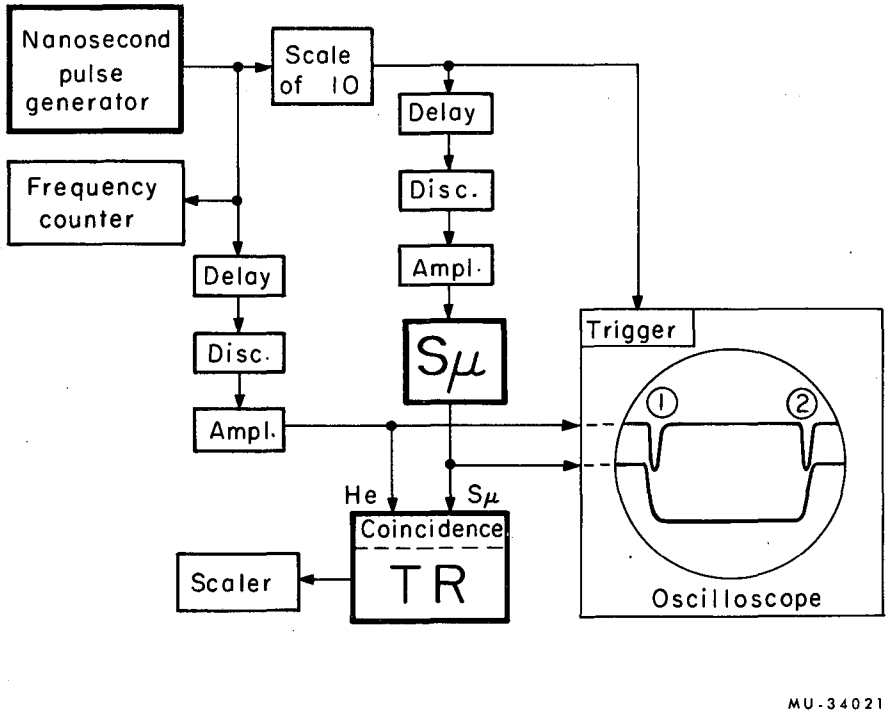

Fig. 34. Schematic diagram of the circuit used in measuring the TR time gate. The oscilloscope face shows the relative timing between the He pulses (1) and (2) and the Sμ pulse.

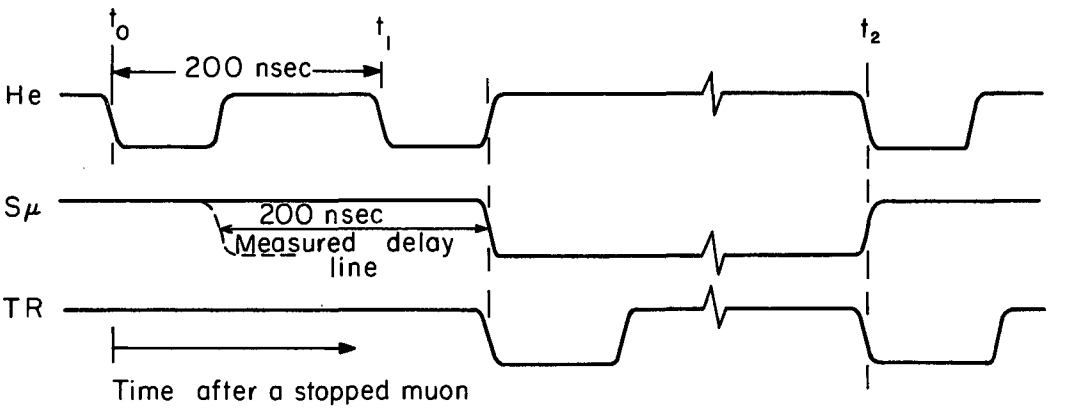

MU-34022

Fig. 35. Sketch of the relative timing of the He and Sμ pulses going into the coincidence TR. Note that this is not to scale; e. g. the He pulse is really only 20 nsec wide whereas the Sμ pulse is 6.2 μsec long. The He pulse occurring at t_o represents the prompt pulse that occurs for every stopping muon. The He pulse at t_1/t_2 represents the earliest/latest possible time at which a delayed pulse could occur in He and still give an output from TR. The dotted Sμ line shows the relative timing when the delay curve shown in Fig. 16(b) was taken. The solid Sμ pulse was delayed 200 nsec from the back edge of the prompt He pulse and since all He pulses had the same shape, t_1-t_2 also equals 200 nsec. Note that the TR output pulse usually takes its timing from the He pulse, but for those He pulses that occur before the start of Sμ, the TR output timing occurs at the start of Sμ. This would lead to an excessive number of pulses occurring in the first channel of the time sorter.

automatically compensates for the finite width of the He pulses and thus the period is the "true" gate length. According to this measurement the Sμ gate length was 6.27 ± 0.03 μsec; the upper/lower limit of error is taken to be the point where (1) and (2) count with 10%/90% efficiency in TR .

Unfortunately this measurement was not made until a month after the experiment and hence because of voltage changes it may also have a systematic error. During the course of the experiment itself, this Sμ pulse length was measured on an oscilloscope that was calibrated with a time-mark generator accurate to 10 ppm. The averaged result of these measurements indicates an Sμ pulse length of 6.13 ± 0.15 μsec in which the error is mostly from oscilloscope readings. This, however, is not the true gate length since even a small overlap of He-Sμ pulses causes TR to fire. To this must be added the He pulsewidth of 20 ± 10 nsec to account for those He pulses that come at the very beginning and the very end of the Sμ gate (see Fig. 35). The final number that was used as the TR gate length is 6.2 ± 0.1 μsec, which represents a compromise between the two methods. In a similar manner the Sμ gate to the μ-e circuit was measured to be 10.6 ± 0.2 μsec long.

D. Details of the Monte Carlo Program

A Monte Carlo program was developed to simulate the various decay modes of a stopping muon. This appendix describes some of the details of this program. Figure 36 is a flow diagram outlining the program, and should be used as a reference in the following discussion of the program's operation.

1. Input

The initial random numbers and two tables are read into the computer. The first table is the muon-stopping distribution, $Q(r, r_o)$, determined by the multiple-scattering calculation and discussed in Sec. III.E.1. The second is the assumed momenta spectra of the charged particle in the breakup reactions (4), (5), and (9) (see Sec. IV.F). All other information is written into the program itself; this includes the target parameters and two subroutines that contain a muon and a proton range-energy table.[88]

The heart of any Monte Carlo calculation is the random-number generator. In this calculation the subroutine GAS[89] generated the "random" numbers by means of a recursion relation of the power-residue type.[90]

$$R_{n+1} = C\, R_n \text{ (module } 2^{35})$$

where R_n is the (nth) random number generated and C is an appropriately chosen constant. Of course such a formula cannot give true random numbers - that is, successive values of R_n that are uncorrelated. However, by judicious choice of the constant C, these correlations may be reduced to the point where the numbers produced closely approximate

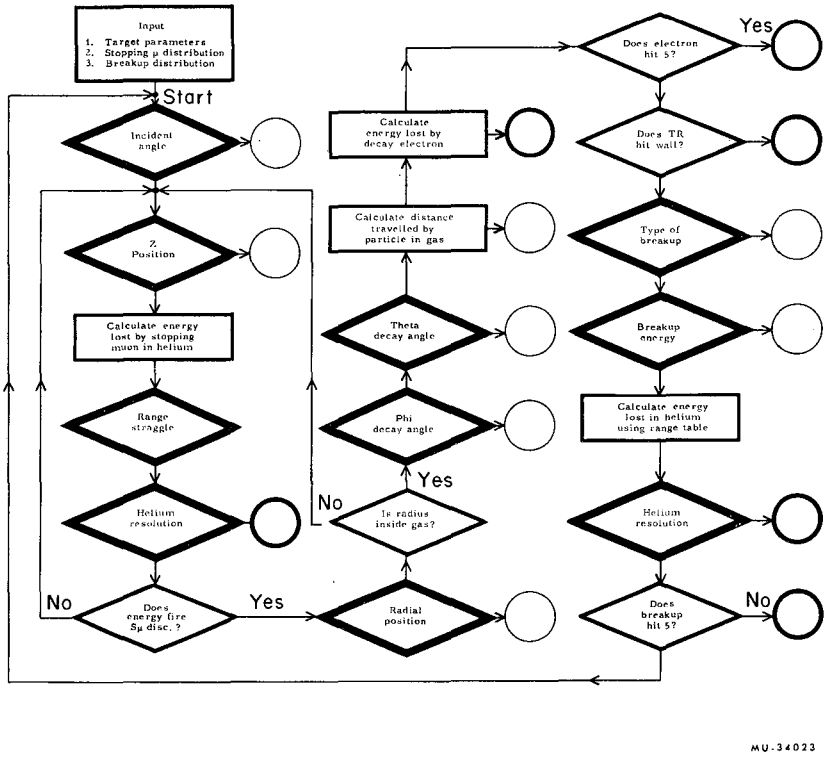

Fig. 36. Rough schematic of the computer-program logic. The heavy diamonds represent an independent random choice of the variable noted inside, and the light diamonds represent a logical choice that the computer makes. The circles represent the output distribution or numbers that are formed -- the light circles output that is used to check the computation, and the dark circles the desired results.

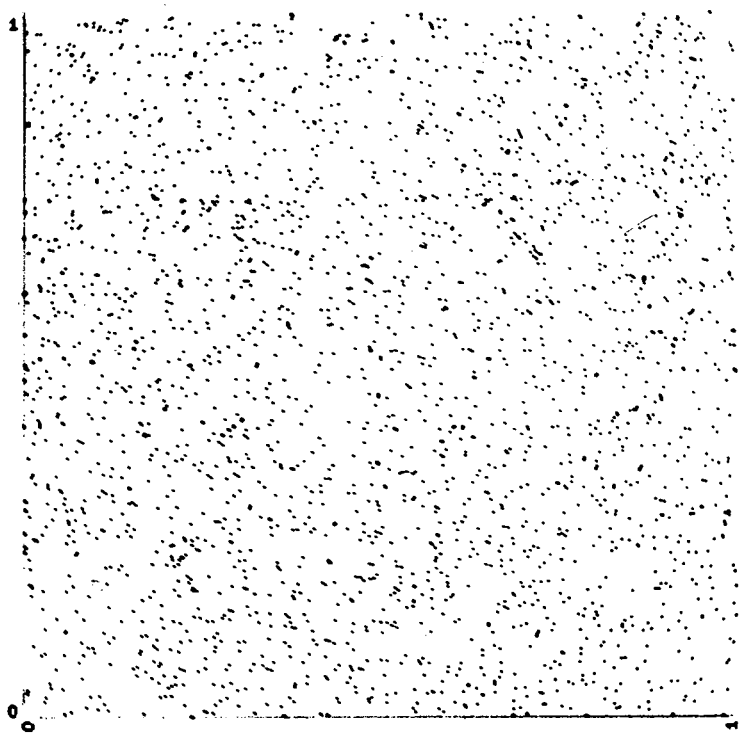

MU-33964

Fig. 37. A test for correlations of successive pairs of "random" numbers generated by the subroutine GAS. The coordinates of each point are determined by successive random numbers generated on the interval between zero and one.

a random distribution.

Figure 37 displays the coordinates of 2500 successive pairs of random numbers chosen on the interval between 0 and 1 and demonstrates no apparent correlations or departures from random distribution.

The entire calculation was done simultaneously for the two He^3 pressures at which data was taken, 28.9 and 15.6 atm. The calculations differed only in that at the lower pressure, the charged particles travelled through less gas and therefore left less energy to be seen by counter 4. Likewise the calculation of the breakup spectrum for muons stopping in He^4 proceeded simultaneously with the He^3 calculation. In the following subsection, however, I limit myself to a discussion of the high pressure He^3 case, since the other calculations are done similarly.

2. Choice of the Coordinates of the Stopping Muon.

The iterative process begins with the choice of the position of the stopping muon. Concomitant with this, the energy lost by the muon by stopping in the gas is calculated. First an incident angle for the stopping muon is randomly chosen according to a Gaussian distribution with $\theta_{rms} = 22^\circ$ (see Sec.III.E.1). This is necessary since variation in the incident angle will affect the energy loss in the gas. Next the coordinate of the stopped muon is chosen randomly, with each plane being weighted equally, as the momentum spread of the beam was much greater than the target width (see Fig. 9). However, two requirements are imposed before this z position is determined as final: (a) the muon must penetrate deeply enough into the helium gas to fire the $S\mu$

discriminator, and (b) after the radial position is determined, r must be $\leq$ 2 inches (so that the muon stops inside the gas). Consequently, at this point, with knowledge of the incident angle and the z position of the stopped muon, the energy lost by the muon in the helium is determined by means of the range-energy table. To this energy is added 0.87 MeV for the effective energy lost in the Lucite window (see Sec. III.D). This 0.87 MeV is determined empirically, as explained below. Next the possible small variation of energy due to range straggling is folded into the Sμ energy followed by the energy-resolution function of the He counter. Both of these random choices follow a Gaussian distribution whose width depends on the energy of the particle. If the resulting energy is greater than 1.5 MeV, then the particle is said to fire the Sμ discriminator, and its radial position is randomly determined according to the probability table $Q(r, r_o)$, previously read into the computer (r_o is a linear function of z). Interpolations between entries of the table are made for both r and r_o. If r is greater than 2 inches (the radius of the gas target), that stopping position is rejected and a new z and r chosen until the particle does fall inside the gas.

At this point in the calculation the computer has the r and z position of the stopped muon, the energy lost by the muon stopping in the gas, and the incident angle of the stopping muon. Tables of each of these quantities display the sum of all these parameters at the end of the calculation. The z and the energy loss tables are derived distributions, but the r and the angle distributions are predetermined.

The formation of these predetermined distributions are a useful check that verifies that the program actually does choose the random numbers according to the desired distribution. This kind of check is made in many places throughout the program. In this instance (as in all checks), the predetermined distributions, formed randomly by the computer, did indeed have the desired shapes.

3. Firing the Sμ Discriminator

The depth to which a muon must penetrate the gas before it generates enough light to fire the Sμ discriminator is difficult to determine, but it is important since this depth affects the distribution of stopping muons and therefore the entire Monte Carlo calculation. This section describes how it was determined and checked, and discusses Figs. 22 and 23. Related to the energy required to fire the Sμ discriminator is the light generated by the muon as it passes through the front Lucite window, for this light is added to that generated in the gas itself. When the Lucite window is discussed it is considered in terms of equivalent gas thickness or equivalent-gas-scintillation light.

Both the Sμ firing energy and the gas equivalent energy deposited in the Lucite window are determined from the experimental curve of energy lost in the helium by a stopping muon (Fig. 22). In order to fit the calculated distribution to the upper edge of this curve (near 6 MeV), 0.87 MeV must be added to the calculated energy lost in the helium. Presumably then this 0.87 MeV represents the light coming from the window. A first check is provided by the dotted

curve in Fig. 20, which is the energy variation expected of a 0.87-MeV energy loss because of the resolution of the He counter. Since we set the Sμ discriminator just above the point where there were no window counts, the small overlap between the Gaussian resolution shape and the energy spectrum indicates that 0.87-MeV for the window energy is about correct. That is to say, an energy less than 0.2 MeV or greater than 1.4 MeV would be completely unacceptable. The 1.5-MeV Sμ-discriminator firing energy was determined by fitting the lower edge of the experimental spectrum to the Monte Carlo calculated spectrum. The over-all fit to the remaining curve is not bad and is an additional check of the stopping-muon distribution and of the Monte Carlo program itself.

The positive-pressure intercept of the Sμ/Bμ curves of Fig. 23(a) lends support to the energies given above and is interesting to calculate in itself; however its interpretation is a bit tricky. The MgO dead layer (See Sec. IV.A), the gas inert region (where muons don't stop because they don't have enough energy to fire the Sμ discriminator), and the Lucite window all contribute to this pressure intercept as can best be seen by reference to Fig. 38. In this diagram all the material that the stopping muon passes through is represented in terms of equivalent range of gas (which can be converted to gas pressures). By considering the point where Sμ/Bμ = 0(60 psia in Fig. 23), one can determine what materials contributed to the pressure intercept. Normally one would expect that the MgO dead layer would subtract from this intercept but because the MgO dead layer does not contribute any

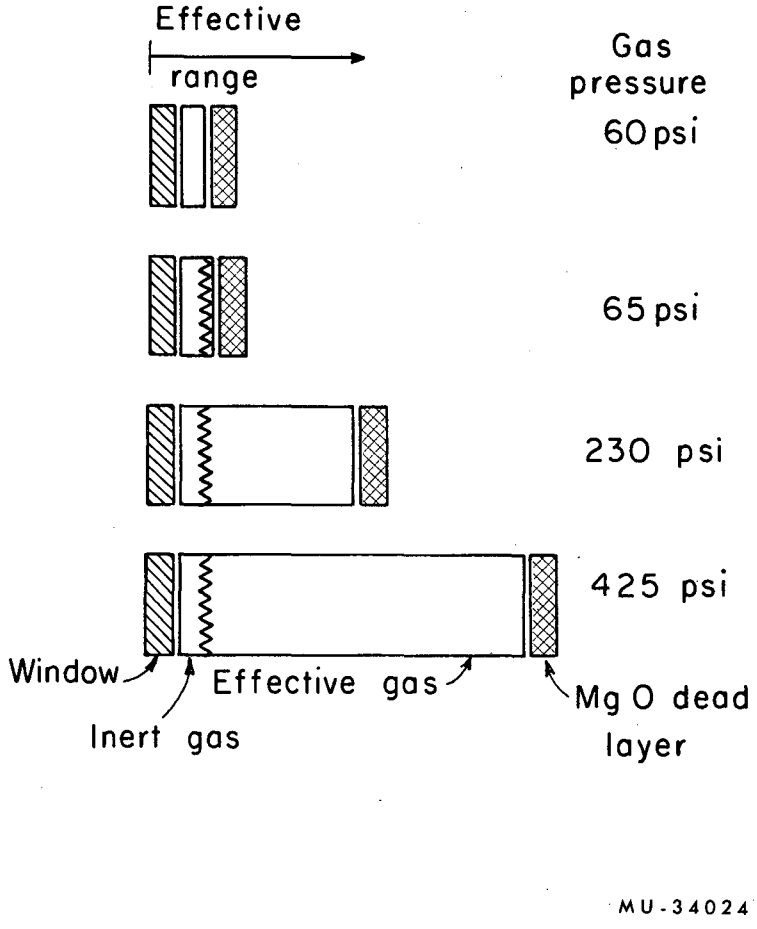

Fig. 38. Schematic representation of the effective range of material that a stopping muon passes through vs the gas pressure. At 60 psi the ratio $S\mu/B\mu = 0$ and thus the remaining range represents the pressure intercept of Fig. 23. Note that in terms of range or deposited energy the gas inert region is independent of the pressure. The wiggly line separates the inert gas from the effective gas.

light to counter 4, the dead layer adds to the intercept as can be seen in Fig. 38. The analysis of Sec. IV.A shows 2.3×10^{-3} $S\mu/B\mu$ stopping in the MgO dead layer. From the slope of Fig. 23, one obtains an equivalent helium thickness of 11 psi. The range of a muon losing 1.5 MeV in the window and gas inert region is 25.5 mg/cm^2, or effectively 45 psi worth of gas. Addition of these contributions shows a predicted pressure intercept of 56 psia, which compares well with the experimental intercept of 60 psia in Fig. 23.

Knowing that the range of an 0.87-MeV muon in the helium is 0.2 inch (at 28.9 atm), one obtains an inert gas thickness of 0.3 inch. This checks well with the cutoff in the z distribution generated by the Monte Carlo program. The meshing of these various experimental and computed values lends weight to the validity of Monte Carlo calculation.

4. The Decay Angle

Having obtained the position of the stopped muon, the computer then randomly chooses the direction of the decay particle. This direction was assumed to be completely isotropic, corresponding to depolarized muons. Although this may not be true, a better guess would be difficult to make. The ϕ coordinate was chosen randomly with a flat distribution on the interval from 0 to 2π ; $\cos\theta$ was chosen according to a flat distribution on the interval from -1 to 1. The net effect is an isotropic angular distribution. In order to increase the statistics of the computation, the same stopped muon was assumed to do everything possible; the same randomly chosen direction was used for the decay electron, the triton recoil, and charged breakup particle directions.

5. Distance Travelled in the Gas

Knowing the position of the stopped muon and the direction of the decaying particle, one can now compute the coordinates of the point where the decay particle leaves the gas, and the distance travelled in the gas. This is a straightforward analytic calculation and was checked by calculating several random cases by hand. Knowing the distance travelled in the gas, we calculated the energy lost by decay electrons in the gas according to Feather's Rule. The resulting energy spectrum did not match the experimental electron background, and predicted a considerably lower energy electron shape. Presumably the higher energy electrons observed experimentally come from a relatively few electrons, which cause delta rays in the helium. Alternatively they may result from light generated in the front Lucite window as the electrons pass through. It did not seem worthwhile to calculate this electron background exactly.

Knowing the coordinates of the point where the electron left the gas, one can calculate the geometric electron-detection efficiency by noting whether the electron would pass through counter 5. Nearly 100% of the electrons in the Michel spectrum have enough energy to veto themselves if they hit counter 5. Thus the geometric efficiency should be the experimental efficiency. With the assumption of an isotropic-decay distribution, the calculations showed that 85.6 ± 0.5% $S\mu$ hit counter 5. This checks well with the observed efficiency, if the various corrections are made as discussed in Sec. III.F.6.

Knowing the range of the triton recoil, one can calculate if the

triton left enough energy in the gas to be detected in the 1.9-MeV peak. Since the range of the triton recoil is only 1.7 mm at 28.9-atm helium pressure, only those muons are affected that stop near the wall and decay so that the triton hits the wall. Thus given the distribution of stopping muons, this is a purely geometric calculation. At high pressure 0.93% and at low pressure 1.73% of the triton recoils lose enough energy in the wall so that they have only a 50% chance of being counted in the pulse-height spectrum. These results are discussed further in Sec. IV.K.

6. Breakup Background Spectrum

Finally the breakup background-energy-spectrum shape, the major result of the Monte Carlo program, can be calculated. First, with an assumed branching ratio between Reactions (4) and (5),

$$\mu^- + He^3 \rightarrow d + n + \nu \qquad (4)$$

$$\mu^- + He^3 \rightarrow p + n + n + \nu \qquad (5)$$

the computer randomly chooses whether the particular muon undergoing calculation is captured into the deuteron or the proton channel. Second, using an assumed "theoretical" energy distribution for the deuteron or proton, the computer randomly chooses an energy at which either the deuteron or proton emerges from the reaction. The assumptions made in choosing these two parameters, the particle's type and its energy, are discussed further in Sec. IV.I.

The remaining computation is geometrical. By use of range-energy relation for either the deuteron or proton in the helium, and the distance that a particle travels in the gas, one calculates the energy

lost in the gas. After folding in the energy resolution of the He counter, one has the energy observed by the PHA. After adding the energies of many stopped muons, one then has the spectrum of the break-up particles. Since data were taken with $\bar{5}$ both in and out of TR, the computer program actually formed two spectra, one with 5 on and one with 5 off. If the breakup particle had enough energy to veto itself in $\bar{5}$, then its energy was not added to the $\bar{5}$-on spectra. Thus the higher energy breakup particles did not contribute to the $\bar{5}$-on spectra.

7. Output

After the calculation of the various energies and distributions for 50 000 stopped muons, representing 20 minutes of IBM 7094 computer time, all the information collected was printed out in tabular form. This included the actual distribution of stopping muons used by the computer, the angular distributions, the energy spectrum of stopping muons, a spectrum of distances travelled in the gas, a spectrum of energy lost in the gas by decay electrons, the various spectra of energy lost in the gas by the breakup processes, the number of electrons and breakup particles detected by counter 5, and the number of triton recoils leaving more than 1 MeV in the wall of the cup counter.

E. Future Improvements to the Experiment

As it does not appear that the theory of muon capture will predict capture rates in helium with an accuracy < 10%, it does not seem worthwhile now to improve the accuracy of this experiment. However, if an improvement is desired in the future, a partial-capture rate accurate to 1/2% could probably be achieved with the present apparatus. Consequently it seems worthwhile to suggest improvements that would be required for a 1/2% experiment. Most of the improvements are easily accomplished; however, the most important, the improved energy resolution of the helium scintillation, is also the most difficult to accomplish. A list follows:

1. Improved energy resolution of the helium scintillation would reduce all errors associated with the backgrounds under the triton peak; these errors limit the present experiment. A factor of 2 improvement in the resolution is vital to a 1/2% experiment. A phototube with higher quantum efficiency would help. Increasing the gas purity is the only certain technique that would increase the scintillation-light output. Probably extensive tests would have to be performed to diagnose just what impurity quenches the light output. Segrè and Wiegand report increased light output if an electric field is applied to the gas.[91] This is probably due to avalanching of the electrons as in a proportional counter, and operation of the scintillator in this mode may be the answer. Adding xenon to the helium, as the Carnegie group did,[18] improves the light

output by about a factor 3; however, most of the muons will then be captured by the xenon and this complicates a determination of the number of muons that are captured by helium atoms. Pure helium gas is probably the best solution to this problem.

2. Reduction of the dead-layer thickness is essential to a better experiment. The xenon experiment described in Sec. IV.A is a good method of determining the dead layer; however, its accuracy is limited. The dead-layer correction introduces the second largest error in this experiment and reducing the thickness of the dead layer would reduce this correction.
3. Improving the muon-beam intensity would allow use of a smaller collimator just before the target. This would cause fewer muons to stop near the walls and therefore reduce the dead layer, edge corrections, and possible wall events.
4. Reducing multiple scattering would also decrease the number of muons stopping near the walls. Half as much multiple scattering can be obtained by eliminating the absorber just before the target, by halving the thickness of counter B2 , and by removing counter 3. Counter 3 does not significantly increase the decay-election detection and its use as a veto in TR can be replaced by counter B2 . Moving the gas target closer to the collimator and counter B2 would further reduce the multiple scattering.
5. Complete 4π decay-electron vetoing would eliminate the

electron-background problem and allow a determination of the breakup spectrum shape at the lower energies. A possible method of achieving the 4π electron-detection would be to put some scintillator such as NaI (which gives out wide pulses), between the Lucite window and the gas. A pulse shape discriminator could then determine whether a given pulse seen in the He counter arose from the gas or from the NaI . A stopping muon would still require a signal from the gas and a decay electron signal would be a delayed NaI pulse.

6. A strictly zero $S\mu$ coincidence rate with vacuum in the target would completely eliminate any ambiguities associated with a few muons stopping in the front window or in a NaI scintillator if it were employed. One can afford a thicker gas inert region than that used in this experiment.
7. Evidence from a later experiment showed that borated paraffin shielding considerably reduced the neutron background around the target. Thus, the addition of paraffin and other shielding would reduce the random background.
8. A special time bin located long after a stopped muon is needed to measure the random rate accurately. The Del-A-Gate unit[60] can be used to generate this gate perhaps 30 to 36 μseconds after an $S\mu$ and any pulses occuring in this time bin can be routed to the second 200 channels of the PHA. This would eliminate the present 20% uncertainty in the random background and would especially improve the accuracy of the breakup

reaction rates.

9. A measurement of the wall events is needed or they must be shown to be neglible.

10. By the use of a more accurate time-to-pulse-height conversion system, such as a digitron,[92] more accurate time spectra could be obtained. Especially if used in combination with 4π decay-electron detection, an accurate digitron would permit another determination of both the μ^+ and the μ^- lifetimes. Comparison between the μ^+ and μ^- lifetimes[93] is a valuable check of the TCP theorem and must be done in the light elements.

11. Periodic measurement, during the course of the experiment, of the length of the Sμ-to-TR gating pulse by the method described in Appendix C would improve the error associated with the time factor. Lengthening the Sμ pulse would reduce the time-factor correction without increasing the randoms rate beyond a tolerable level.

12. Two moniters should be added to the electronics. The first is another coincidence circuit that would ensure that all of the Sμ-to-TR gating pulses are at least 6 μsec long and that none are anomalously short. The second is a scaler that would count all the pulses to be analyzed by the PHA. This would provide a means of ensuring that the PHA does not lose memory and that it stores all the pulses that go into it.

13. Making any second-beam particle veto the whole Sμ event would protect the system from TR events in which a second

muon gives a true triton-recoil.

14. Since opening the vacuum box is a lengthy process, the bases of the phototubes should be located outside the MVT, if possible. During the initial part of the experiment, several phototube bases failed and it was difficult to repair them while inside the MVT. Alternatively more reliable bases are required.

Although I suggest many improvements, the experiment as it was run did work well and provided a somewhat better result than we originally hoped for.

F. List of Tables

REFERENCES

1. M. Conversi, E. Pancini, and O. Piccioni, Phys. Rev. 71, 209 (1947); See also T. Sigurgeirsson and K. A. Yamakawa, Phys. Rev. 71, 319 (1947), and G. E. Valley, Phys. Rev. 72, 772 (1947).
2. J. Tiomno and J. A. Wheeler, Rev. Modern Phys. 21, 153 (1949).
   O. Klein, Nature 161, 897 (1948).
   G. Puppi, Nuovo Cimento 5, 587 (1948); 6, 194 (1949).
   T. D. Lee, J. Rosenbluth, and C. N. Yang, Phys. Rev. 75, 905 (1949).
   C. N. Yang and J. Tiomno, Phys. Rev. 79, 495 (1950).
3. R. K. Bardin, C. A. Barnes, W. A. Fowler, and P. A. Seeger, Phys. Rev. 127, 583 (1962).
4. H. A. Weidenmüller, Phys. Rev. 127, 537 (1962).
5. E. J. Konopinski, Ann. Rev. of Nucl. Sci. 9, 99 (1959);
   W. S. C. Williams, An Introduction to Elementary Particles, (Academic Press, New York, 1961).
   C. S. Wu, Rev. Mod. Phys. 36, 618 (1964).
6. G. Feinberg and L. M. Lederman, Ann. Rev. of Nucl. Sci. 13, 466 (1963).
7. E. Fermi and E. Teller, Phys. Rev. 72, 399 (1947).
8. R. Huff, Ann. Phys. (N. Y.) 16, 288 (1960).
9. L. Wolfenstein, The Muon Absorption Interaction, Proceedings of the 1960 Annual International Conference on High-Energy Physics, Rochester, N. Y. (Interscience Publishers, Inc., New York, 1960), p. 529.
10. R. D. Sard and M. F. Crouch, Nuclear Interactions of Stopped μ-Mesons in Progress in Cosmic Ray Physics, edited by J. G. Wilson (North-Holland Publishing Company, Amsterdam, 1954) Vol. 2.
11. V. L. Telegdi, Phys. Rev. Letters 8, 327 (1962).
12. J. C. Sens, Phys. Rev. 113, 679 (1959);
    M. Eckhause, T. A. Filippas, R. B. Sutton, and R. E. Walsh, Phys. Rev. 132, 422 (1963).

13. J. E. Rothberg, E. W. Anderson, E. J. Bleser, L. M. Lederman, S. L. Meyer, J. L. Rosen, and I-T. Wang, Phys. Rev. 132, 2664 (1963).
R. H. Hildebrand, Phys. Rev. Letters 8, 34 (1962).
E. Bleser, L. Lederman, J. Rosen, J. Rothberg, and E. Zavattini, Phys. Rev. Letters 8, 288 (1962).
E. Bertolini, A. Citron, G. Gianlanella, S. Focardi, A. Mukhin, C. Rubbia, and S. Saporetti, Determination of the μ^- Total Capture Rate in Liquid Hydrogen, Proceedings of the International Conference on High-Energy Physics, (Geneva, Switzerland, 1962) p. 421.
14. S. Weinberg, Phys. Rev. Letters 4, 575 (1960).
Ya. B. Zel'dovich and S. S. Gershtein, Usp. Fiz. Nauk, 71, 581 (1960) [translation: Soviet Physics - Usp. 3, 593 (1961)].
15. A. F. Yano, Phys. Rev. Letters 12, 110 (1964).
16. I. V. Falomkin, A. I. Filippov, M. M. Kulyukin, B. Pontecorvo, Yu. A. Scherbakov, R. M. Sulyaev, V. M. Tsupko-Sitnikov, and O. A. Zaimidoroga: Phys. Letters 1, 318 (1962); 3, 229 (1963); 6, 100 (1963).
17. R. L. Wagner, Jr., Ph. D. Thesis, Muon Capture in Helium-3, University of Utah (unpublished).
18. R. M. Edelstein, D. Clay, J. W. Keuffel, and R. L. Wagner, Jr., Measurement of the Rate for $\mu^- + He^3 \rightarrow H^3 + \nu$, Proceedings of the Conference on Fundamental Aspects of Weak Interactions, (Brookhaven National Laboratory, Upton, N. Y.), Sept. 1963 (to be published).
19. L. B. Auerbach, R. J. Esterling, R. E. Hill, D. A. Jenkins, J. T. Lach, and N. H. Lipman, Phys. Rev. Letters 11, 23 (1963).
20. R. Bizzarri, E. diCapua, U. Dore, G. C. Gialanella, P. Guidoni, and I. Laakso, Phys. Letters 3, 151 (1962); 3, 312 (1962).
21. M. Block, Proceedings of the Conference on Fundamental Aspects of Weak Interactions at Brookhaven, Sept. 1963 (to be published). (Also reported in Ref. 84.)

22. R. P. Feynman and M. Gell-Mann, Phys. Rev. 109, 193 (1958).
23. A. Fujii and Y. Yamaguchi, Progr. Theoret. Phys. 31, 107 (1964).
24. S. S. Gershtein and I. B. Zel'dovich, Soviet Phys. JETP 2, 576 (1956).
25. M. L. Goldberger and S. B. Treiman, Phys. Rev. 111, 354 (1958).
26. S. Weinberg, Phys. Rev. 112, 1375 (1958).
27. Wolfgang Drechsler and Berthold Stech, The Induced Pseudoscalar Interaction and the μ-Capture in He^3, (Institute für theoretische Physik der Universität Heidelberg), preprint, September, 1963.
28. Y. K. Lee, L. W. Mo, and C. S. Wu, Phys. Rev. Letters 10, 253 (1963).
A. F. Dunaitsev, V. I. Petrukhim, Yu. D. Prokoshkin, and V. I. Rykalin, Phys. Letters 1, 138 (1962).
P. Depommier, J. Heintze, A. Muhkin, C. Rubbia, V. Soergel and K. Winter, Phys. Letters 2, 23 (1962), and ibid., 5, 61 (1963).
R. Bacastow, T. Elioff, R. Larsen, C. Wiegand and T. Ypsilantis, Phys. Rev. Letters 9, 400 (1962).
29. S. D. Drell and F. Zachariasen, Electromagnetic Structure of Nucleons (Oxford University Press, London, 1961), Chap. I.
30. F. Everling, L. A. König, J. H. E. Mattauch, and A. H. Wapstra, Nucl. Phys. 18, 529 (1960).
31. D. Strominger, J. M. Hollander, and G. T. Seaborg, Rev. Mod. Phys. 30, 602 (1958).
32. H. Collard, R. Hofstadter, A. Johansson, R. Parks, M. Ryneveld, A. Walker, M. R. Yearian, R. B. Day, and R. T. Wagner, Phys. Rev. Letters 11, 132 (1963);
H. Collard and R. Hofstadter, Phys. Rev. 131, 416 (1963).
33. R. Hofstadter, Rev. Mod. Phys. 28, 214 (1956).
34. R. Hofstadter and R. Herman, Phys. Rev. Letters 6, 293 (1961).

35. Calculated by Kistner and Rustad, see M. Goldhaber, Weak Interactions: Leptonic Modes, International Conference on High Energy Physics, (CERN, CERN Scientific Information Service, Geneva, Switzerland, 1958), p. 238.

36. A. Fujii and H. Primakoff, Nuovo Cimento 12, 327 (1959).

37. M. Conversi, R. Diebold, and L. di Lella, Radiative Muon Capture in Ca^{40} and the Induced Pseudoscalar Coupling Constant (paper presented at the International Conference on Weak Interactions, Brookhaven, Upton, N. Y.) Sept. 1963.
M. L. Yovnovich and V. S. Evseev, Phys. Letters 6, 333 (1963).

38. R. C. Cohen, S. Devons, and A. D. Kanaris, Phys. Rev. Letters 11, 134 (1963).
A. Astbury, L. Auerbach, D. Cutts, R. Esterling, D. Jenkins, N. H. Lipman, and R. E. Shafer, Muon Capture in Oxygen (UCRL-11299), submitted to Nuovo Cimento.

39. J. B. Adams, Phys. Rev. 126, 1567 (1962).

40. E. U. Condon and G. H. Shortley, The Theory of Atomic Spectra (Cambridge, University Press, 1935) p. 422.

41. R. Winston, Phys. Rev. 129, 2766 (1963); R. Winston and V. L. Telegdi, Phys. Rev. Letters 7, 104 (1962);
A. P. Bukhvostov, I. M. Shmushkevich, Soviet Phys. JETP 14, 1347 (1962).

42. H. Primakoff, Revs. Mod. Phys. 31, 802 (1959). See also Ref. 83.

43. C. Werntz, Nucl. Phys. 16, 59 (1960).

44. L. Wolfenstein, Weak Interactions: Strangeness-Conserving, in Proceedings of the International Conference on High-Energy Physics, Geneva, 1962 (CERN Scientific Information Service, Geneva, Switzerland, 1962), p. 821. The theoretical Λ_C is given here as 1400 ± 140 sec^{-1}. In a private communication to N. Lipman, Wolfenstein gives a rate of 1500 sec^{-1} based on the recently measured He^3 and H^3 form factors.[32]

45. A. Fujii, Phys. Rev. 118, 870 (1960).

46. I. Duck, Nucl. Phys. 35, 27 (1962).

47. R. B. Murray, Scintillation Counters, in Nuclear Instruments and their Uses, Vol. 1 (A. H. Snell, ed.) Wiley, New York, 1962.
R. E. Shamu, Nucl. Instr. Methods 14, 297 (1961).
The article by Murray summarizes a large fraction of the work done on noble-gas scintillation and contains a useful bibliography. The final configuration used in our gas scintillator was similar to that described in Shamu's article.
S. A. Baldin, V. V. Gavrilovskii, and F. E. Chukreev, Soviet Journal of Atomic Energy 3, 331 (1957).

48. J. A. Northrup and J. C. Gursky, Nucl. Instr. 3, 207 (1958).

49. F. E. Moss and F. L. Hereford, [Phys. Rev. Letters 11, 63 (1963)] report on an effect in superfluid He II, and W. P. Jesse and J. Sadauskis, [Phys. Rev. 100, 1755 (1955)] report on ionization of helium by alpha particles. Our effects and the two given here may be related in a general way.

50. C. Rubbia and M. Toller, Nuovo Cimento 10, 410 (1958).

51. S. C. Brown in Handbook of Physics, E. U. Condon and H. Odishaw, Ed. (McGraw-Hill, New York, 1958), p. 4-166.

52. M. A. Biondi and S. C. Brown, Phys. Rev. 76, 1697 (1949).

53. A. Astbury, K. M. Crowe, J. G. Deutsch, T. Maung, and R. E. Taylor, Study of the Optimum Target Position for the Secondary Meson Beams from the 184-inch Cyclotron, UCRL-10120, March 1962.

54. T. J. Devlin, OPTIK, UCRL-9727, September 1961.

55. O. Chamberlain, Ann. Rev. Nucl. Sci. 10, 179 (1960).

56. Developed by Morris Pripstein, LRL.

57. H. Bethe and J. Ashkin, Passage of Radiations through Matter, in Experimental Nuclear Physics, Vol. 1, E. Segrè, ed. (John Wiley & Sons, New York, 1953), pp. 266, 285.

58. R. M. Sternheimer, Rev. Sci. Instr. 25, 1070 (1954).

59. Written by David Jenkins and Joseph Good, LRL.

60. Lawrence Radiation Laboratory Counting Handbook, UCRL-3307, January 1959.
61. A. E. Bjerke, Q. A. Kerns, T. A. Nunamaker, Nucl. Instr. Methods 15, 249 (1962). LRL Drawing No. 5X2203.
62. A. E. Bjerke, Q. A. Kerns, T. A. Nunamaker, IRE Trans. Nucl. Sci. N5-9, No. 3, p. 314 (1962). LRL Drawing No. 5X2374.
63. G. Culligan and N. H. Lipman, Rev. Sci. Instr. 31, 1209 (1960).
64. William A. Wenzel, Millimicrosecond Coincidence Circuit for High Speed Counting, UCRL-8000, October 1957.
65. This circuit was designed by G. Culligan and N. H. Lipman (CERN) and is shown in Fig. 15.
66. Designed by Mel Brown of the Lawrence Radiation Laboratory.
67. D. L. Wieber, A Fast Wide-Range Time-to-Height Conversion System, UCRL-10425, September 1962.
68. Jagdish S. Baijal, Atomic Capture of μ^- Mesons in Chemical Compounds and the "Fermi-Teller Z Law" (Ph. D. Thesis), UCRL-10429, August 1962.
69. GRID SEARCH developed by William B. Johnson and Joseph T. Lach, LRL.
70. H. L. Anderson and W. C. Davidon, Nuovo Cimento 5, 1238 (1957).
71. M. M. Block, Phys. Rev. 101, 796 (1956).
72. H. Morinaga and W. F. Fry, Nuovo Cimento 10, 308 (1953).
73. Burns MacDonald (Lawrence Radiation Laboratory), private communication, 1964.
74. E. I. Dolinsky and L. D. Blokhintsev, Nucl. Phys. 10, 527 (1959).
75. A. Bietti and P. DiPorto, Nuovo Cimento 28, 270 (1963).
76. D. J. Hughes and R. B. Schwartz, Neutron Cross Sections (Brookhaven National Laboratory, Upton, N. Y.) BNL-325 (2nd Ed.), 1958.
77. J. D. Seagrave, Phys. Rev. 92, 1222 (1953).
78. C. A. Caine and P. S. H. Jones, Nucl. Phys. 44, 177 (1963).

79. A. M. L. Messiah, Phys. Rev. 87, 639 (1952).
80. A. F. Yano (Long Beach State College), private communication, 1964.
81. S. K. Allison and S. D. Warshaw, Rev. Mod. Phys. 25, 779 (1953).
82. H. L. Anderson, E. P. Hincks, C. S. Johnson, C. Rey, and A. M. Segar, The Capture Rate for Muons in Helium, International Conference on Elementary Particles, Aix-en-Provence, 1961, Vol. 1, p. 141. (Abstract).
83. A. Bietti, Nuovo Cimento 20, 1043 (1961).
84. B. Goulard, G. Goulard, and H. Primakoff, Phys. Rev. 133, B186 (1964).
85. J. Bernstein, M. Ruderman, and G. Feinberg, Phys. Rev. 132, 1227 (1963).
86. G. Charpak, F. I. M. Farley, R. L. Farwin, T. Muller, J. C. Sens, and A. Zichichi, Phys. Letters 1, 16, (1962).
87. The seal design will be described in an article by E. Mc Laughlin, W. Pope, and R. Schafer (Lawrence Radiation Laboratory), private communication, 1963.
88. J. H. Atkinson and B. H. Willis, High Energy Particle Data, UCRL-2426 (rev.), June 1957.
89. Developed by Joseph Lach, UCRL.
90. Random Number Generation and Testing (International Business Machines Corporation, Data Processing Division, 112 East Post Road, White Plains, New York) 1959.
91. E. Segrè and C. Wiegand, Lawrence Radiation Laboratory Semiannual Report, UCRL-2152.
92. R. A. Swanson, Rev. Sci. Instr. 31, 149 (1960).
93. S. L. Meyer, E. W. Anderson, E. Bleser, L. M. Lederman, J. L. Rosen, J. Rothberg, and I-T. Wang, Phys. Rev. 132, 2693 (1963).